Aus der Anatomischen Anstalt der Universität München
Institut der Ludwig-Maximilians-Universität München

Vorstand/Direktor: Prof. Dr. Christoph Schmitz

Titel der Arbeit:

DDIT3-vermittelte Oligodendrozyten Apoptose und läsionsabhängige Gangstörungen in der Frühphase zweier MS Tiermodelle.

Dissertation
zum Erwerb des Doktorgrades der Medizin
an der Medizinischen Fakultät der
Ludwig-Maximilians-Universität zu München

vorgelegt von

Felix Fischbach

aus München

2021

Mit Genehmigung der Medizinischen Fakultät
der Universität München

Berichterstatter:	Univ. Prof. Dr. Dr. Markus Kipp
Mitberichterstatter:	Prof. Dr. med. Frank. Weber
	Priv. Doz. Dr. med. Astrid Blaschek
	Priv. Doz. Dr. med. Lisa Ann Gerdes
Mitbetreuung durch den promovierten Mitarbeiter:	
Dekan:	Prof. Dr. med. dent. Reinhard Hickel
Tag der mündlichen Prüfung:	28.01.2021

Inhaltsverzeichnis

Eidesstattliche Versicherung

Ich erkläre hiermit an Eides statt, dass ich die vorliegende Dissertation mit dem Titel „DDIT3-vermittelte Oligodendrozyten Apoptose und läsionsabhängige Gangstörungen in der Frühphase zweier MS Tiermodelle.“ selbständig verfasst, mich außer der angegebenen keiner weiteren Hilfsmittel bedient und alle Erkenntnisse, die aus dem Schrifttum ganz oder annähernd übernommen sind, als solche kenntlich gemacht und nach ihrer Herkunft unter Bezeichnung der Fundstelle einzeln nachgewiesen habe. Ich erkläre des Weiteren, dass die hier vorgelegte Dissertation nicht in gleicher oder in ähnlicher Form bei einer anderen Stelle zur Erlangung eines akademischen Grades eingereicht wurde.

München, den 15.03.2020

Felix Fischbach

Abkürzungsverzeichnis

ATF3	Activating Transcription Factor 3
ATF6	Activating Transcription Factor 6
CIS	klinisch isoliertes Syndrom
CNS	central nervous system
DDIT3	DNA damage-inducible transcript 3
EAE	experimentelle Autoimmune-Enzephalomyelitis
EDSS	expanded disability status scale
ER	endoplasmatisches Retikulum
eIF2α	eukaryotic Initiation Factor 2 alpha
IgG	Immunglobulin G
Ire1	Inositol-requiring Enzyme 1
mRNA	messenger-Ribonukleinsäure
MRT	Magnetresonanz-Tomographie
MS	Multiple Sklerose
OPCs	Oligodendrozyten Progenitor Zellen
PERK	Protein Kinase RNA-like Endoplasmic Reticulum Kinase
T25FW	timed 25-foot walk
UPR	unfolded protein response
ZNS	Zentralnervensystem

Einleitung

Multiple Sklerose (MS) ist eine neurologische Erkrankung, die mit dem Untergang von Oligodendrozyten, Demyelinisierung, Gliose, axonalem Schaden und der Aktivierung von peripheren Immunzellen einhergeht. Die demyelinisierten Läsionen unterscheiden die MS von anderen neurologischen Erkrankungen und sind somit auch von zentraler Bedeutung in den MS Tiermodellen.

Die ersten Symptome zeigen sich meist zwischen dem 25. und 35. Lebensjahr. Die Erkrankung betrifft doppelt so häufig Frauen wie Männer. Mit einer weltweiten Prävalenz von ca. 2 Millionen Patienten, davon 150.000 Patienten in Deutschland, ist die MS eine der häufigsten neurologischen Erkrankung und eine häufige Ursache bleibender Behinderungen bei jungen Erwachsenen. Etwa 30% der MS Patienten werden vorzeitig berentet. In der Gesamtheit belaufen sich die jährlichen Krankheitskosten bundesweit auf 4 Milliarden Euro (Gold, 2012). Sowohl genetische Faktoren als auch Umwelteinflüsse wirken sich auf das Erkrankungsrisiko aus (Bender, 2015).

Klinisch äußert sich die Erkrankung durch fokal-neurologische Defizite des Zentralnervensystems (ZNS). Dabei kann es zu Sehstörungen, motorischen Ausfällen, Gang- und Gleichgewichtsstörungen, sensiblen Defiziten sowie vegetativen und psychischen Störungen kommen (Bender, 2015). Die Krankheitsprogression eines Patienten wird anhand des (engl.) ‚*expanded disability status scale*' (EDSS) beurteilt. Dabei nimmt die Gehstrecke, sofern sie auf unter 500m ohne Hilfsmittel reduziert ist, eine zentrale Rolle ein (Kurtzke, 1983). Bei geringen Mobilitätsdefiziten (Score-Bereich 0-4.5/10) fallen Störungen aus insgesamt 8 funktionellen Systemen wie Blasenfunktion, visuelles System oder Kleinhirnfunktion stärker ins Gewicht. Daneben wird der (engl.) ‚*timed 25-foot walk*' (T25FW) zur weiteren Evaluation der Mobilität verwendet (Motl, 2017). Der 9-Loch-Steck-Test überprüft die Funktion der oberen Extremität und die Koordination feiner Bewegungen (Feys, 2017). Mehrere Arbeiten konnten zeigen, dass Patienten von einem frühen Therapiestart profitieren. So führt eine frühe Behandlung zu weniger Schüben und einem geringeren EDSS-Wert (PRISMS Study Group, 2001). Eine frühe Diagnosestellung setzt sensitive diagnostische Parameter voraus, um einen frühen Therapiestart gewährleisten zu können.

Die MS kann klinisch in 3 verschiedene Verlaufsformen unterteilt werden: die mit 85-90% häufigste Form (Hafler, 2004) ist die schubförmige MS, in der es zwischen zwei Schüben zur vollständigen Remission der Symptome kommt. Diese kann in eine sekundär progressive Form übergehen, bei der sich der klinische Zustand progredient verschlechtert. Sowohl Schübe als auch Remissionen treten dabei typischerweise nicht

mehr auf. Ein Schub wird als neu aufgetretene, zeitlich abgrenzbare klinische Symptomatik mit mindestens 30 Tagen Abstand zum letzten Schub definiert. Dabei dürfen die Veränderungen weder durch Änderungen der Körpertemperatur noch durch eine Infektion erklärbar sein (Bender, 2015). Die MS kann auch von Beginn an ohne Schübe primär progredient verlaufen, wobei sich der klinische Zustand stetig verschlechtert. Die schubförmige MS zeigt einige Merkmale einer klassischen Autoimmunerkrankung, wie etwa das epidemiologische Verteilungsmuster und das vermehrte Auftreten nach bestimmten Infektionen (z.B. symptomatische EBV-Infektion) (Rejdak K, 2010). Diese Merkmale fehlen bei den progressiven Formen, welche eher Gemeinsamkeiten mit neurodegenerativen Erkrankungen zeigen (Stys, 2012). Das Krankheitsrisiko ist annähernd gleich zwischen den Geschlechtern verteilt und der Erkrankungsgipfel liegt im 4. bis 5. Lebensjahrzehnt, und somit 10 bis 20 Jahre später als bei der schubförmigen MS.

Diagnostisch zeigen sich neben den fokal neurologischen Defiziten elektrophysiologisch Zeichen der zentralnervösen Demyelinisierung im Sinne von Latenzverlängerungen der evozierten Potentiale (Pihl-Jensen, 2017). In der Liquoruntersuchung zeigen sich außerdem liquorspezifische oligoklonale IgG-Banden. Diese stellen das laborchemische Korrelat der intrathekalen IgG-Synthese dar (Bender, 2015). In Magnetresonanz-Tomographie (MRT) Aufnahmen zeigen sich entzündliche demyelinisierte Läsionen, die sowohl in der weißen als auch in der grauen Substanz lokalisiert sind (Stys, 2012). Dort treten sie typischerweise subkortikal, periventrikulär sowie in den Nervi optici, im Hirnstamm und im Rückenmark auf (Nylander, 2012). Aktive Läsionen zeigen durch eine in diesem Bereich gestörte Integrität der Blut-Hirn-Schranke eine Aufnahme des Kontrastmittels Gadolinium. Solche entzündlichen Veränderungen kommen bei den progredienten Verlaufsformen weniger häufig vor (Gold, 2012). Die 2017 überarbeiteten McDonald Diagnose-Kriterien der MS setzen eine räumliche und zeitliche Dissemination dieser MRT-Läsionen voraus (Thompson, 2018). Besteht eine typische Symptomatik, allerdings ohne zeitliche Dissemination, wie es häufig im Frühstadium der Erkrankung der Fall ist, spricht man vom klinisch isolierten Syndrom, kurz CIS (Gold, 2012).

MS Läsionen können histopathologisch in verschiedene Stadien eingeteilt werden. Aktive Läsionen sind hyperzellulär und diffus von Immunzellen infiltriert. Sie lassen sich anhand des Vorhandenseins von Myelin-Abbauprodukten, die durch die Phagozytose von Myelin durch Mikrogliazellen/Makrophagen entstehen, in demyelinisierend und post-demyelinisierend unterteilen. Gemischt-aktiv/inaktive Läsionen sind demyelinisiert mit hypozellulärem Zentrum und hyperzellulärem Randsaum aus Makrophagen und

Mikrogliazellen. Inaktive Läsionen sind scharf begrenzt, hypozellulär und praktisch frei von reifen Oligodendrozyten sowie Myelin (Kuhlmann , 2016). Es kommt in den Läsionen außerdem zu einer Proliferation von Astrozyten und Mikrogliazellen. Die MS führt somit zu Veränderungen aller drei Haupttypen von Gliazellen. Dabei gehen allerdings spezifisch Oligodendrozyten unter, während Astrozyten und Mikrogliazellen im selben Mikro-Milieu proliferieren.

Oligodendrozyten bilden im ZNS die Myelinscheiden aus, die wichtig für die schnelle und energieeffiziente Weiterleitung von Aktionspotentialen sind (Philips, 2017). Sie versorgen außerdem die Internodien mit Nährstoffen (Fünfschilling, 2012) und stellen schnellen axonalen Transport sicher (Edgar, 2004). Aus den Vorläuferzellen, den sogenannten Oligodendrozyten Progenitor Zellen (OPCs), entwickeln sich durch verschiedene externe und interne Stimuli reife Oligodendrozyten. Diese umgeben mit ihren Ausläufern verschiedene Axonabschnitte mit unterschiedlich dicken Schichten aus Myelin (Mitew, 2013). Dabei durchlaufen sie ein komplexes Programm aus Proliferation, Migration und Differenzierung bis hin zur eigentlichen Myelinisierung (Teske, 2018). Der Prozess der Myelinisierung überschreitet den Zeitraum der Gehirnentwicklung bei Weitem und setzt sich bis in das höhere Erwachsenenalter fort. Dies ist wichtig, um auch über die reine Hirnentwicklung hinaus neuronale Plastizität zu gewährleisten, wie sie u. a. für Lernprozesse erforderlich ist (Bergles, 2015).

Die Synthese von Phospholipiden, dem Hauptbestandteil des Myelins, findet zellulär am glatten endoplasmatischen Retikulum (ER) statt (Lodish, 2000). Das ER ist zeitgleich das zentrale Zellorganell für die Translokation, Faltung und Modifikation sekretorischer Proteine (Sano, 2013) sowie von Membranproteinen, wie z.B. Myelinproteinen. Im ER-Lumen herrscht ein oxidatives Mikro-Milieu, das für die Ausbildung von Disulfidbrücken wichtig ist. Disulfidbrücken sind unter anderem Voraussetzung für die regelhafte Faltung von Proteinen (Xu, 2005). Um den vollständigen Grad der Myelinisierung in einem Gehirn zu erreichen und zu erhalten ist das ER von Oligodendrozyten hohem, und für diese Zellart spezifischem Stress ausgesetzt.

Unter Stress versteht man einen meist länger andauernden Belastungszustand. Auf zellulärer Ebene sind verschieden Stressreaktionen bekannt, zu denen z.B. die Stressantworten des ERs zählen. Viele verschiedene zellschädigende Einflüsse, wie etwa Schwermetalle, virale Infektionen oder freie Radikale, können zu einer Funktionsstörung bzw. Stressreaktion des ERs führen. Diese wird aufgrund des vermehrten Anfalls fehlgefalteter Proteine als (engl.) *unfolded protein response* (UPR) bezeichnet

(Kozutsumi, 1988). Die UPR geht unter anderem mit einer vermehrten Expression spezifischer Stressgene des ERs einher. Die klassische Kaskade wird durch 3 ER-Transmembran-Proteine initiiert bzw. koordiniert: *Inositol-requiring Enzyme 1* (Ire1), *Protein Kinase RNA-like Endoplasmic Reticulum Kinase* (PERK) und *Activating Transcrpiton Factor 6* (ATF6). In der Folge wird durch die Phosphorylierung des *eukaryotic Initiation Factor 2 alpha* (eIF2α) die globale zelluläre Translation vermindert, während die Translation von Chaperonen und anderen zytoprotektiven Proteinen induziert wird (Lin, 2012). Bei anhaltendem zellulärem Stress werden schließlich auch pro-apoptotische Proteine, wie der Transkriptionsfaktor DNA damage-inducible transcript 3 (DDIT3) (Rutkowski, 2006) oder *Activating Transcription Factor 3* (ATF3) (Edagawa, 2014) induziert. Überwiegen solche pro-apoptotischen Signale in einer Zelle wird die Apoptose eingeleitet. Die zellulären Mechanismen der Oligodendrozyten Degeneration sind nur unzureichend verstanden. Sie stellen einen möglichen therapeutischen Angriffspunkt dar, um Demyelinisierung zu verhindern bzw. abzuschwächen.

Zur experimentellen Untersuchung der MS werden vor allem zwei Tiermodelle verwendet. Die experimentelle Autoimmune-Enzephalomyelitis (EAE) dient als Modell des T-Zell vermittelten, inflammatorischen Aspekts der Erkrankung (Kipp, 2017). In den Tieren wird eine Immunantwort gegen Myelinbestandteile herbeigeführt. Dies führt im Verlauf zu neurologischen Ausfällen im Sinne von am Schwanz beginnenden nach kranial aufsteigenden Paresen. Die Beurteilung des aktuellen klinischen Zustands des Tieres sowie des Verlaufs erfolgt durch ein festgelegtes Scoring-System. Dabei werden das Ausmaß der aufsteigenden Paresen und die damit verbundenen Mobilitätseinschränkungen beurteilt. In diesem Aspekt ist das System ähnlich zum klinisch angewandten EDSS-Score. Histopathologisch kommt es bereits vor klinischen Auffälligkeiten zu strukturellen und funktionellen Veränderungen des Rückenmarks, unter anderem einer Aktivierung von Astrozyten (Alvarez, 2015), einer Verminderung der Expression von Myelin-Genen (Evangelidou, 2014) und der perivaskulären Ansammlung von Mikrogliazellen (Baranzini, 2005). Im zweiten Tiermodell, dem toxischen Cuprizone Modell (bis-cyclohexanone-oxaldihydrazone), kommt es zu einer T-Zell unabhängigen Demyelinisierung. Diese beruht auf einer primären Oligodendrozyten Apoptose mit begleitender Mikroglia- und Astrozytenaktivierung (Kipp, 2017). Cuprizone führt dabei zu einer Erhöhung des oxidativen Zellstresses., u. a. durch Hemmung von Komplex IV der Atmungskette (Acs, 2013). Im Cuprizone Modell können

histologisch verschiedene Phasen unterschieden werden.. In der Frühphase (bis ca. 1 Woche nach Intoxikationsbeginn) kann die Induktion von zellulärem Stress, z.B. ER-Stress oder pro-apoptotischen Signalen, nachgewiesen werden. Ab Woche 3 lässt sich der Untergang von Oligodendrozyten mit folgender Demyelinisierung sowie der Aktivierung von Mikrogliazellen und Astrozyten feststellen. Diese Veränderungen nehmen bis Woche 5 weiter zu (Kipp, 2009). Die Ausdifferenzierung von OPCs zu reifen Oligodendrozyten führt ca. ab Woche 6 zu einem Wiederanstieg der Oligodendrozyten Zellzahl im ZNS der Versuchstiere (Mason, 2000).

Die molekularen Mechanismen, welche im Cuprizone Modell zur Oligodendrozyten Apoptose und Demyelinisierung führen, waren bisher nicht bekannt. Daher untersuchten wir zu welchen Expressionsänderung es im Genom durch die Cuprizone Intoxikation kommt. Dabei zeigte sich, dass unter anderem die Expression von Genen der ER-Stresskaskade bereits nach kurzer Intoxikationsdauer induziert wird. Die stärkste Expressionsänderung konnten wir unter allen ER-Stressfaktoren für den pro-apoptotischen Transkriptionsfaktor DDIT3 nachweisen. Mit Immunfluoreszenz Doppelfärbungen untersuchten wir welche Zellen jeweils zu verschiedenen Zeitpunkten im Tiermodell DDIT3 exprimieren. Es zeigte sich, dass DDIT3 in der Frühphase (1 Woche Cuprizone) hauptsächlich von Oligodendrozyten exprimiert wird. Im weiteren Verlauf (3 und 5 Wochen Cuprizone) konnte aber auch in Astrozyten eine nukleäre DDIT3 Expression nachgewiesen werden. Die nach anfänglicher Stressreaktion folgende Oligodendrozyten Apoptose setzt sich bis Woche 5 fort. Für eine funktionelle Aussage über DDIT3 im Cuprizone Modell verglichen wir eine globale *Ddit3*$^{-/-}$ Maus mit dem Wildtyp nach 3 Wochen Cuprizone Intoxikation. Hier zeigte sich bei *Ddit3*$^{-/-}$ Mutanten eine verminderte Oligodendrozyten Apoptose, Demyelinisierung, Mikrogliose, Astrozytose und axonaler Schaden. Somit ist DDIT3 ein wichtiger Transkriptionsfaktor für den frühen Oligodendrozyten Schaden im Cuprizone Modell und führt bei vermehrter Expression zum Untergang dieser Zellart mit einhergehender Demyelinisierung.

Die zweite Publikation beschäftigt sich mit der Frage, ob in der Frühphase der entzündlichen Demyelinisierung im EAE-Modell Gangstörungen nachgewiesen werden können. Dazu wurde in den Versuchstieren eine EAE induziert. Im Verlauf wurden neben dem beschriebenen Scoring-System tägliche Ganguntersuchungen durchgeführt. Mittels (engl.) „*High Speed Ventral Plane Videography*“ wurde das Gangbild analysiert. Es erfolgte dabei eine Unterteilung in 39 Gangparameter der Vorderpfoten und 43 Gangparameter der Hinterpfoten. Nach Abschluss der klinischen Tests wurden die

Versuchstiere histologisch auf das Vorliegen von entzündlichen ZNS Läsionen untersucht. Es zeigte sich, dass während der Entwicklung neuer inflammatorischer ZNS Herde verschiedene Gangdefizite auftreten. Dabei kommt es unter anderem zu einer verlängerten Schwungphase bei verkürzter Standphase. Die Veränderungen des Gangmusters treten dabei auf, bevor die Versuchstiere im EAE Scoring System Auffälligkeiten zeigen.

Eigenleistung an beiden Publikationen

Arbeitsanteil an der ersten Publikation (Fischbach et al. ‘Cuprizone-induced graded oligodendrocyte vulnerability is regulated by the transcription factor DNA damage-inducible transcript 3.’; Glia):

- Beteiligung an der Durchführung der Tierexperimente
- Literaturrecherche
- Experimentplanung
- Immunhistochemie und Immunfluoreszenzstudien
- Auswertung des 3D elektronenmikroskopischen Datensatzes
- Revision einschließlich der nötigen Experimente, Abschlusskorrekturen und Visualisierung der Daten

Arbeitsanteil an der zweiten Publikation (Zhan et al. ‘High Speed Ventral Plane Videography as a convenient Tool to quantify Motor Deficits during Pre-Clinical Experimental Autoimmune Encephalomyelitis.’; Cells):

- Beteiligung an der Durchführung der Tierexperimente
- Datenauswertung der Ganganalyse
- Literaturrecherche
- Abschlusskorrekturen

Veröffentlichung I

Fischbach F, Nedelcu N, Leopold P, Zhan J, Clarner T, Nellessen L, Beißel C, van Heuvel Y, Goswami A, Weis J, Denecke B, Schmitz C, Hochstrasser T, Nyamoya S, Victor M, Beyer C, Kipp M: ‚Cuprizone-induced graded oligodendrocyte vulnerability is regulated by the transcription factor DNA damage-inducible transcript 3.‘; *Glia*, 2019

Received: 3 April 2018 | Revised: 5 September 2018 | Accepted: 7 September 2018
DOI: 10.1002/glia.23538

GLIA
WILEY

RESEARCH ARTICLE

Cuprizone-induced graded oligodendrocyte vulnerability is regulated by the transcription factor DNA damage-inducible transcript 3

Felix Fischbach[1] | Julia Nedelcu[1] | Patrizia Leopold[1] | Jiangshan Zhan[1] | Tim Clarner[2] | Lara Nellessen[2] | Christian Beißel[2] | Yasemin van Heuvel[2] | Anand Goswami[3] | Joachim Weis[3] | Bernd Denecke[4] | Christoph Schmitz[1] | Tanja Hochstrasser[1] | Stella Nyamoya[1,2] | Marion Victor[2] | Cordian Beyer[2] | Markus Kipp[1,5]

[1]Faculty of Medicine, LMU Munich, Chair of Neuroanatomy, Institute of Anatomy, Munich, Germany

[2]Faculty of Medicine, RWTH Aachen University, Institute of Neuroanatomy, Aachen, Germany

[3]Institute of Neuropathology, RWTH Aachen University, Aachen, Germany

[4]Interdisciplinary Center for Clinical Research Aachen (IZKF Aachen), RWTH Aachen University, Aachen, Germany

[5]Institute of Anatomy, Rostock University Medical Center, Rostock, Germany

Correspondence
Markus Kipp, Institute of Anatomy, University of Rostock, 18057, Rostock, Germany.
Email: markus.kipp@med.uni-rostock.de

Funding information
Dr. Robert Pfleger Stiftung, Grant/Award Number: None; Deutsche Forschungsgemeinschaft, Grant/Award Number: KI 1469/8-1; Robert-Pfleger Stiftung

Abstract

Oligodendrocytes are integral to efficient neuronal signaling. Loss of myelinating oligodendrocytes is a central feature of many neurological diseases, including multiple sclerosis (MS). The results of neuropathological studies suggest that oligodendrocytes react with differing sensitivity to toxic insults, with some cells dying early during lesion development and some cells being resistant for weeks. This proposed graded vulnerability has never been demonstrated but provides an attractive window for therapeutic interventions. Furthermore, the biochemical pathways associated with graded oligodendrocyte vulnerability have not been well explored. We used immunohistochemistry and serial block-face scanning electron microscopy (3D-SEM) to show that cuprizone-induced metabolic stress results in an "out of phase" degeneration of oligodendrocytes. Although expression induction of stress response transcription factors in oligodendrocytes occurs within days, subsequent oligodendrocyte apoptosis continues for weeks. In line with the idea of an out of phase degeneration of oligodendrocytes, detailed ultrastructural reconstructions of the axon–myelin unit demonstrate demyelination of single internodes. In parallel, genome wide array analyses revealed an active unfolded protein response early after initiation of the cuprizone intoxication. In addition to the cytoprotective pathways, the pro-apoptotic transcription factor DNA damage-inducible transcript 3 (DDIT3) was induced early in oligodendrocytes. In advanced lesions, DDIT3 was as well expressed by activated astrocytes. Toxin-induced oligodendrocyte apoptosis, demyelination, microgliosis, astrocytosis, and acute axonal damage were less intense in the *Ddit3*-null mutants. This study identifies DDIT3 as an important regulator of graded oligodendrocyte vulnerability in a MS animal model. Interference with this stress cascade might offer a promising therapeutic approach for demyelinating disorders.

KEYWORDS

apoptosis, cuprizone, demyelination, multiple sclerosis, oligodendrocytes

1 | INTRODUCTION

Multiple sclerosis (MS) lesions are characterized by oligodendrocyte death, demyelination, gliosis, axonal damage, and peripheral immune cell recruitment. The feature that distinguishes MS from other neurological disorders is the formation of confluent demyelinated plaques. For this reason, any pathogenetic concept of MS must provide an explanation for this highly specific destruction of myelin and oligodendrocytes. The sequence of molecular events leading to oligodendrocyte loss, and consequently, demyelination is not fully understood, but involved mechanisms may include oxidative stress, mitochondrial dysfunction, protein misfolding, or inflammatory cytokine exposure. It is important to note that viable oligodendrocytes and an intact myelin sheath are indispensable for neuronal health. Oligodendrocytes

provide nutritional support to neurons (Funfschilling et al., 2012), and fast axonal transport depends on oligodendrocytes (Edgar et al., 2004). Mice deficient in mature myelin proteins show severe neurodegeneration (Uschkureit, Sporkel, Stracke, Bussow, & Stoffel, 2000). It has been suggested that during active demyelination, distinct oligodendrocyte populations are more vulnerable than others, resulting in an asynchronous oligodendrocyte degeneration during MS lesion development (Lucchinetti et al., 1999).

Oligodendrocyte stress may perturb the function of the endoplasmic reticulum (ER), resulting in ER stress. ER stress triggers an adaptive pathway in mammalian cells that controls the response to ER stress through transcriptional activation of genes coding for essential ER chaperones (Kozutsumi, Segal, Normington, Gething, & Sambrook, 1988). This adaptive response is termed the unfolded protein response (UPR). Classically, an UPR is initiated by three ER transmembrane proteins: inositol requiring 1 (IRE1), protein kinase RNA-like ER kinase (PERK), and activating transcription factor 6 (ATF6). The focal point of UPR induction is the phosphorylation of eukaryotic initiation factor 2 alpha, which diminishes global protein translation while selectively upregulating the translation of chaperones such as heat shock protein 5 (HSPA5) (Kohno, Normington, Sambrook, Gething, & Mori, 1993) and other cytoprotective proteins. When cell stress persists, components of the UPR, such as DNA damage-inducible transcript 3 (DDIT3), can mediate apoptosis (Gow & Wrabetz, 2009).

In this study, we describe that in a model of toxin-induced demyelination, oligodendrocyte stress is an early event that is characterized by the expression of UPR stress factors. Histological and immunohistochemical studies show that while oligodendrocyte degeneration starts within days, the vulnerability of oligodendrocytes differs, with some cells degenerating early and some cells being resistant for weeks. In addition, serial block-face scanning electron microscopy (SEM) demonstrated demyelination of selective internodes during acute demyelination. Genome wide array analyses and functional studies using knock-out animals showed that the transcription factor DDIT3 is an important regulator of cuprizone-induced demyelination.

2 | MATERIALS AND METHODS

2.1 | Animals and mating strategy

For the cuprizone intoxication studies, 8-week-old C57BL/6 male mice were purchased from Janvier Labs, Le Genest-Saint-Isle, France. To analyze the functional relevance of DDIT3 in the cuprizone model, *Ddit3*$^{-/-}$ mice were obtained from The Jackson Laboratory (Bar Harbor, Maine, USA) (005530-B6.129S[Cg]-Ddit3tm2.1Dron/J) and were mated with C57BL/6 mice to obtain a heterozygous F1-generation. The F1-mice were then mated to obtain *Ddit3*$^{-/-}$ and *Ddit3*$^{+/+}$ mice. Offspring of these F2-mice were used for experiments for a maximum of five generations. All experimental procedures were approved by the Review Board for the Care of Animal Subjects of the district government (Regierung Oberbayern; reference number 55.2-154-2532-73-15; Germany). The genotyping protocols are described elsewhere (https://www.jax.org/strain/005530).

2.2 | Cuprizone-induced demyelination and histological evaluation

Cuprizone intoxication was performed as described previously (Hochstrasser, Exner, Nyamoya, Schmitz, & Kipp, 2017; Slowik et al., 2015). In brief, 0.25 g cuprizone was weighed using precision scales and mechanically mixed with 100 g ground standard rodent chow using a commercially available kitchen machine (Kult X, WMF Group, Geislingen an der Steige, Germany). The chow was mixed at a low speed and manual agitation for 1 min and was then provided within the cage in two separate plastic Petri dishes. The number of animals used for the different experiments is provided in the figure legends. The following exclusion criteria were applied: severe weight loss (>10% within 24 hr), severe behavioral deficits (decreased locomotion, convulsions, and stupor), or infections. No single animal met the exclusion criteria during this study. At the end of the experiment, mice were deeply anaesthetized with ketamine (100 mg/kg i.p.) and xylazine (10 mg/kg i.p.) and transcardially perfused with ice-cold phosphate-buffered saline (PBS) followed by a 3.7% paraformaldehyde solution (PFA; pH 7.4) or tissue dissection. All histological investigations were performed with paraffin-embedded brain sections. For the gene and protein expression studies, the tissues were manually dissected after transcardial PBS perfusion, immediately frozen in liquid nitrogen, and kept at −80 °C until further processing. We kept the number of animals used to a minimum. To this end, the in vivo materials used during this study are currently being used for other studies and will be available for other research groups upon request to the authors.

Standard Haemotoxylin and Eosin (H&E) stains were prepared for the evaluation of apoptosis using established morphological criteria, such as condensed and fragmented cell nuclei (Hesse et al., 2010). Previously established protocols were used to conduct the immunohistochemistry (Baertling et al., 2010; Ruther et al., 2017; Slowik et al., 2015). In brief, sections were rehydrated, and if necessary, antigens were unmasked with heating in Tris/ethylenediaminetetraacetic acid (EDTA) (pH 9.0) or citrate (pH 6.0) buffer. After washing in PBS, the sections were incubated overnight (4 °C) with the primary antibodies diluted in blocking solution (serum of species in which the secondary antibody was produced). A list of antibody characteristics is provided in Supporting Information Supplementary Table S1. The next day, the slides were incubated with biotinylated secondary antibodies for 1 hr and then with peroxidase-coupled avidin-biotin complex (ABC kit (Burlingame, California, USA); Vector Laboratories, Peterborough, USA), followed by treatment with 3,3′-diaminobenzidine (DAKO, Hamburg, Germany) as a peroxidase substrate. The stained and processed sections were digitalized using a Nikon ECLIPSE E200 microscope (Nikon Instruments, Düsseldorf, Germany) equipped with a DS-Vi1 camera. If not stated otherwise, histological parameters were evaluated at the levels of the anterior commissure and the ventral hippocampus. To analyze cell densities, the area of the region of interest (ROI) (i.e., midline of the corpus callosum) was manually outlined using ImageJ (NIH, Bethesda, MD), and positive cells were counted by at least two evaluators blinded to the treatment groups, and then, the results were averaged and given as cells/mm^2. To evaluate demyelination in Luxol fast blue (LFB)-stained sections, the magnitude of

myelination was scored in the midline of the corpus callosum between 100 and 0 by two blinded evaluators and the results were averaged. A score of 100 is equivalent to the myelin status of a control mouse, whereas zero is equivalent to a fully demyelinated corpus callosum. Anti-Myelin proteolipid protein (PLP) stained sections were evaluated by densitometry of the staining intensity using ImageJ and automated thresholding.

Immunofluorescence double-labeling experiments were performed with the following combinations of primary antibodies: (a) anti-DDIT3 (1:50; Abcam (Cambridge, UK), catalogue number ab11419, RRID:AB_298023) combined with anti-oligodendrocyte transcription factor 2 (OLIG2) (1:1,000; Millipore (Burlington, Massachusetts, USA), catalogue number AB9610, RRID:AB_570666), (b) anti-DDIT3 (1:200; Santa-Cruz (California, USA), catalogue number sc-575, RRID:AB_631365) combined with either anti-ionized calcium-binding adapter molecule 1 (IBA1) (1:1,000; Abcam, catalogue number ab107159, RRID:AB_10972670) or with anti-glial fibrillary acidic protein (GFAP) (1:1,000; Abcam, catalogue number ab4674, RRID_AB304558), (c) anti-ATF3 (1:200; Santa-Cruz, catalogue number sc-188, RRID:AB_2258513) combined with either anti-OLIG2 (1:100; Millipore, catalogue number MABN50, RRID:AB_10807410), anti-IBA1 (1:1,000; Abcam, catalogue number ab107159, RRID:AB_10972670) or anti-GFAP (1:1,000; Abcam, catalogue number ab4674, RRID_AB304558). Appropriate Alexa Fluor-coupled secondary antibodies (Life Technologies, Germany) were used to visualize the antigen–antibody complexes. For immunofluorescence double-staining experiments, DDIT3 was visualized by incubating slides first with anti-mouse biotinylated secondary antibodies (1:200; Vector, catalogue number. BA-9200, RRID:AB_2336171) followed by Alexa Fluor 488-coupled streptavidin antibodies (1:100; Invitrogen (Carlsbad, California, USA), catalogue number S11223).

Appropriate negative controls (i.e., omission of primary antibodies or incubation with the "wrong" secondary antibody) were performed in parallel as previously described (Baertling et al., 2010). For immunofluorescence double-labeling experiments, cell nuclei were counterstained with Hoechst 33342 (Invitrogen, Germany). Sections were viewed using a Leica DMI6000 B inverted microscope. Nuclear localization of DDIT3 was verified by confocal microscopy using a Zeiss LSM 7 Duo microscope (Oberkochen, Germany).

2.3 | Ultrastructural analysis via serial block-face SEM

Myelinated and demyelinated corpora callosa (i.e., 3 weeks cuprizone) were analyzed by 3D-SEM. To this end, mice were perfused with 2.5% (wt/vol) glutaraldehyde and 4% PFA, the brains were removed, stained with heavy metals, and embedded in resin as previously described (Ohno et al., 2014). Serial block-face SEM was performed by using a SigmaVP SEM (Carl Zeiss, Munich, Germany) equipped with a 3View in-chamber ultramicrotome system (Gatan). Serial image sequences were generated at 80-nm steps, providing image stacks that were 204.54 μm × 61.36 μm wide at a resolution of 0.001 μm per pixel. The images were processed and measured with the open source programme *Reconstruct* (BU, Boston, MA). The focus of this analysis was to detect partial axonal demyelination (i.e., demyelinated internodes flanked at least at one site by a myelinated internode). The analyzed tissue volume was small enough to avoid any bias of the results because of regional heterogeneity in oligodendrocyte susceptibility against the cuprizone intoxication (Xing et al., 2014).

2.4 | Gene expression analyses

Tissues were lysed in RNAPure™ solution (peqGOLD VWR, Dresden, Germany) using the homogenisator Precellys® 24 (VWR, Dresden, Germany). Astrocyte cultures were directly lysed in RNAPure™ solution. After RNA isolation and cDNA synthesis, gene expression levels were measured by real-time reverse transcription-polymerase chain reaction (RT-qPCR; Bio-Rad, Munich, Germany) using SensiMix Plus SYBR and fluorescein (Quantace, Bioline, Luckenwalde, Germany) with a standardized protocol as described previously by our group (Slowik et al., 2015). The primer sequences and individual annealing temperatures are shown in Supporting Information Supplementary Table S2. Relative quantification was performed using the ΔΔCt method using *Hprt* and/or *18S* as the reference gene. Melting curves and gel electrophoresis of the PCR products were routinely performed to determine the specificity of the PCR reactions (data not shown). Negative controls were performed during the cDNA synthesis and PCR to check for contamination of the products. For the PCR analysis of spliced and non-spliced *Xbp-1* mRNA, a primer set was designed to simultaneously detect both mRNA variants. The presence of spliced and non-spliced mRNA results in two distinct PCR products, which were separated by agarose gel electrophoresis. The cDNA from tunicamycin-exposed OliNeu cells (50 μg/ml for 24 hr; Sigma-Aldrich, Taufkirchen, Germany) served as a positive control. Commercial fluorescence in situ hybridization (ISH) kits (QuantiGene View RNA ISH tissue assay; Affymetrix-Panomics, Waltham, MA, USA) were used for the detection of *Plp* mRNA in the formalin-fixed, paraffin-embedded tissues, following published protocols (Clarner et al., 2015).

2.5 | Western-blotting analyses

For protein expression studies, the tissues were manually dissected after transcardial PBS perfusion, immediately frozen in liquid nitrogen, and kept at −80 °C until further processing. The tissues were lysed in ice-cold RIPA buffer (New England BioLabs (Ipswich, Massachusetts, USA), catalogue number 9806S) containing protease-inhibitor (New England BioLabs, catalogue number 5871S), and phosphatase-inhibitor (New England BioLabs, catalogue number 5870S) using the homogenisator Precellys® 24 (VWR, Germany). Lysed protein solutions were subsequently centrifuged at 2,000*g* for 5 min at 4 °C, and the supernatant was collected. The protein concentration of each sample was quantified using bovine serum albumin (BSA) as an internal standard (Thermo Fisher Scientific (Waltham, MA, USA), catalogue number 23209). A total of 20 μg of protein was denatured in Laemmli buffer containing sodium dodecyl sulfate (SDS; pH = 6.8) and NuPage sample reducing agent (Thermo Fisher Scientific, catalogue number NP0004). The proteins were separated in an 8–14% SDS-polyacrylamide gel electrophoresis and transferred to nitrocellulose membranes. The blots were blocked in 5% BSA (Cell signalling technology (Danvers, MA, USA), catalogue number 9998) in Tris-buffered

saline (TBS) and after a rinsing step, were incubated overnight (4 °C) in primary antibodies directed against DDIT3 (1:1,000; Cell signalling, catalogue number 2895, RRID:AB_2089254), β-actin (1:2,000; Sigma-Aldrich (Taufkirchen, Germany), catalogue number A5060, RRID: AB_476738), ubiquitin (1:1,000; DAKO, catalogue number Z0458, RRID:AB_2315524), or HSPA5 diluted in 5% BSA in TBS-Tween (TBST). The membranes were then washed three times in TBST, followed by incubation in appropriate horseradish peroxidase-conjugated secondary antibodies, and diluted in 5% BSA in TBST for 2 hr at room temperature. After rinsing in TBST (three times), the signal was detected via chemiluminescence (SignalFireTM ECL Reagent; Cell signalling, catalogue number 6883) and visualized with the FluorChem E system (ProteinSimple; San Jose, California).

2.6 | Primary astrocyte culture

Primary astrocyte cultures from the brains of P1–P3 mice were prepared as previously described with some modifications (Braun, Dang, Johann, Beyer, & Kipp, 2009). For the propagation, cells were grown in 75-cm^2 plastic cell culture flasks in Dulbecco's modified Eagle's medium (DMEM) with 4.5 g/L D-glucose, sodium pyruvate and L-glutamine (DMEM; Gibco Life Technologies (Carlsbad, California, USA), catalogue number 41966-029) and were supplemented with 1% penicillin/streptomycin (Pen/Strep; Gibco Life Technologies, catalogue number 15140-122), and 10% fetal bovine serum (FBS; Gibco Life Technologies, catalogue number 10500-064). The cells were cultured at 37 °C in a humidified 5% CO_2 atmosphere with medium replenishment every 2–3 days during cell maintenance. For the experiments, the cells were seeded onto 9.6 cm^2 (~5 × 10^5 cells) plastic culture dishes pre-coated with 10 μg/ml poly-D-lysin (PDL, MW 70,000–150,000; Sigma-Aldrich (Taufkirchen, Germany), catalogue number P6407) in modified SATO-medium. The modified SATO was composed of DMEM with 1% N_2 supplement (Gibco Life Technologies, catalogue number 17502-048), 0.1% tri-iodo-thyronine (Sigma-Aldrich, catalogue number T6397), 0.016% L-thyroxin (Sigma-Aldrich, catalogue number T1775), and 0.05% gentamicin (Gibco Life Technologies, catalogue number 15710049). For more details see (Teske et al., 2018). The purity of the cultures was assessed by anti-IBA1 and anti-GFAP immunocytochemical stains and was greater than 90%. To analyze whether stimulation of the primary astrocyte cultures induces the expression of *Ddit3* and/or chemokines, the following substances were applied: interferon-γ (IFNγ; 560 U/ml; obtained from Sigma-Aldrich, catalogue number I4777), lipopolysaccharide (LPS; 100 ng/ml; obtained from Sigma-Aldrich, catalogue number L4391) or the complex-IV inhibitor sodium azide (SA; 10 mM; obtained from Sigma-Aldrich, catalogue number S2002). All toxins were prepared as stock solutions and properly stored, except of SA, which was always freshly prepared. The cultures were maintained in starving medium, which is composed of DMEM with 1% Pen/Strep (Gibco, catalogue number 15140122), 24 hr before stimuli application, and then, the stimulation lasted for 12 hr.

2.7 | Statistical analysis

All data are given as arithmetic means ± standard error of the mean. Differences between groups were statistically tested using the software package GraphPad Prism 5 (GraphPad Software Inc., San Diego, CA). The applied statistical procedures are provided in the figure legends. p values ≤.05 were considered statistically significant. The following symbols were used to indicate the level of significance: *p ≤ .05, **p ≤ .01, ***p ≤ .001, ns = not significant.

3 | RESULTS

3.1 | Sequential oligodendrocyte degeneration during cuprizone-induced demyelination

Initially, we wanted to analyze whether oligodendrocyte degeneration is an asynchronous or simultaneous process in the cuprizone model. To this end, we first quantified the densities of mature oligodendrocytes in the anti-CC1 (APC; adenomatous polyposis coli protein) stained sections. The densities of the mature oligodendrocytes gradually declined until week 3. After week 1 of cuprizone intoxication, the oligodendrocyte densities declined from 2,465.4 ± 98.5 to 403.5 ± 24.4 cells/mm^2, whereas oligodendrocyte densities were 79.9 ± 10.3 cells/mm^2 at week 3 (Figure 1a). Of note, the difference in oligodendrocyte densities between week 1 and week 3 was highly significant (p ≤ .001). Comparable results were obtained if sequential slides were evaluated for the presence of anti-OLIG2$^+$ cells, resembling both mature and immature oligodendrocytes (data not shown). Next, stressed oligodendrocytes were labeled by anti-ATF3 (activating transcription factor 3) staining (Goldberg et al., 2013), and their densities were related to apoptotic oligodendrocyte densities. As shown in Figure 1b–d, high densities of apoptotic cells were found between Day 2 and week 1. At weeks 3 and 5, oligodendrocyte apoptosis was still ongoing. Although it has been demonstrated that in the cuprizone model oligodendrocyte apoptosis is ongoing for weeks (Hesse et al., 2010; Sanadgol et al., 2017; Xing et al., 2018), we verified this aspect by staining sections with anti-OLIG2 antibodies and inspecting the corpus callosum for the presence of OLIG2$^+$ apoptotic bodies. As demonstrated in Figure 1e, apoptotic bodies decorated by anti-OLIG2 immunoreactivity could be clearly demonstrated at week 3. In control animals, virtually none of the CC1$^+$ mature oligodendrocytes expressed ATF3. After 2 days of cuprizone-intoxication, densities of the mature oligodendrocytes were comparable to the control groups, but most of them (approximately 70%) expressed the stress marker protein ATF3. In summary, these immunohistochemical results suggest sequential rather than simultaneous degeneration of oligodendrocyte subpopulations.

To verify this assumption, we performed serial block-face SEM of the corpora callosa from the control and 3 weeks cuprizone-intoxicated mice. If demyelination indeed occurs in a sequential manner, one should find axons with demyelinated internodes flanked by intact, normally myelinated internodes (i.e., internodal demyelination). In control animals, a node of Ranvier was always flanked on both sides by a compact myelin sheath, whereas in cuprizone-intoxicated animals, a myelin sheath was frequently missing at one side of the node but present at the other side (Figure 1f–h). In some cases, we observed a demyelinated internode flanked on both sides by a myelinated internode. To quantify the frequency of internodal

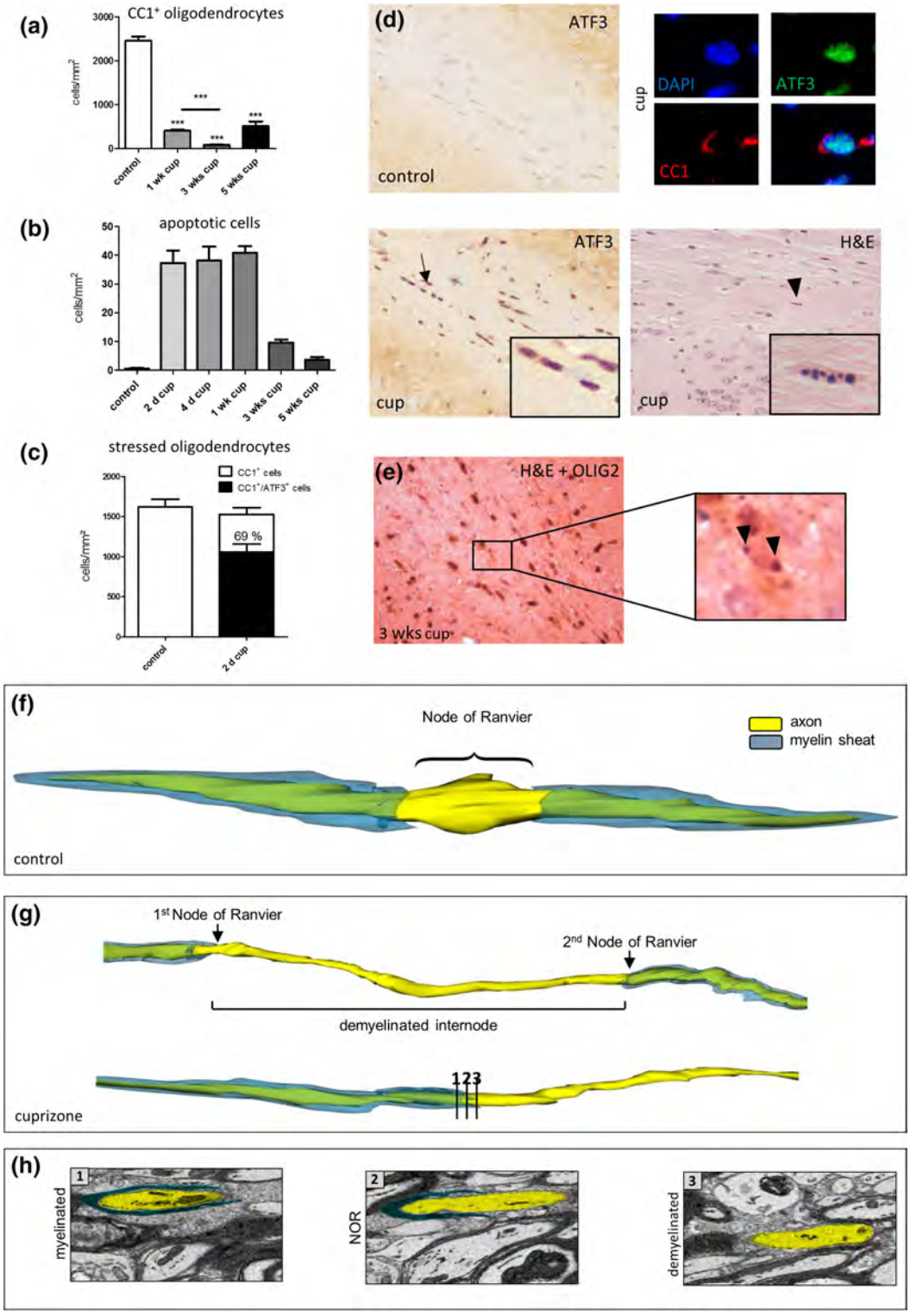

FIGURE 1 Sequential degeneration of oligodendrocytes. (a) Densities of $CC1^+$ mature oligodendrocytes during the course of cuprizone-induced demyelination. Six biological replicates were used. Statistical comparison was conducted using a one-way analysis of variance with the obtained *p* values corrected for multiple testing using the Dunnett's post hoc test. Significant differences with respect to the control animals are indicated by ***$p < .001$. (b) Densities of the apoptotic cells during the course of cuprizone-induced demyelination. At least six biological replicates were used. (c) Relative numbers of activating transcription factor 3 ($ATF3^+$) oligodendrocytes after 2 days of cuprizone intoxication. Three biological replicates were used. (d) Representative images illustrating the expression of *ATF3* in stressed oligodendrocytes after 2 days of cuprizone intoxication. Arrow indicates $ATF3^+$ oligodendrocytes. Arrowhead indicates an apoptotic oligodendrocyte. (e) Representative image illustrating positive anti-$OLIG2^+$ staining of an apoptotic oligodendrocyte after 3 weeks of cuprizone intoxication. Arrowheads indicate apoptotic bodies. (f) The 3D-reconstruction of a normal axon from a control animal. (g) The 3D-reconstruction from an axon with internodal demyelination after 3 weeks of cuprizone intoxication. Ultrastructural appearance of a node of Ranvier is shown in (h) at three consecutive planes [Color figure can be viewed at wileyonlinelibrary.com]

demyelination, 100 normally appearing axons (i.e., no axonal pathology or demyelination visible in the given plane) from four different animals were randomly selected, and their morphology was investigated in the entire 3D-stack. The results showed that 48% of these axons exhibited internodal demyelination. Taken together, these results convincingly demonstrate that oligodendrocyte stress occurs simultaneously, whereas degeneration of oligodendrocyte cell bodies and myelin sheaths occurs sequentially.

3.2 | DDIT3 is specifically expressed by oligodendrocytes during early cuprizone intoxication

To investigate which signaling pathways potentially orchestrate cuprizone-induced sequential oligodendrocyte apoptosis, we reanalyzed gene array data (control vs. 2 days cuprizone) obtained from the highly cuprizone-susceptible and oligodendrocyte-rich corpus callosum (Krauspe et al., 2015). In addition to *Atf3*, the expression of the transcription factor *Ddit3*, which is related to apoptosis, was found to be highly induced (Gow & Wrabetz, 2009). Furthermore, PANTHER GO-Slim over-representation analysis for the term "protein class" revealed enrichment of specific aminoacyl-tRNA synthetases (8.4-fold enrichment), which has recently been shown to be regulated by *Ddit3* (Han et al., 2013).

Next, we performed immunohistochemistry to analyze DDIT3 expression levels. DDIT3$^+$ cells were almost absent in the control animals. Immunoreactivity, if visible, was mainly observed in the perinuclear compartment (Figure 2e; arrow). After 4 days of cuprizone intoxication, the densities of CC1$^+$ mature oligodendrocytes were just marginally decreased (Figure 2a), but many DDIT3$^+$ cells were found (Figure 2b,e). As evidenced by bright field and confocal microscopy, most of the anti-DDIT3 signal was observed within the nuclear compartment, indicating the activity of this transcription factor. A more detailed time course analysis revealed high densities of DDIT3$^+$ cells from Day 2 until week 1, with lower densities at week 3 and week 5 (Figure 2c). A comparable *Ddit3* mRNA expression pattern was found by RT-qPCR studies (data not shown). Furthermore, higher DDIT3 protein levels were found by western blotting at Day 4 in the isolated corpus callosum (Figure 2d). To determine the cellular source of DDIT3 expression, we examined 1,689 representative DDIT3$^+$ nuclear profiles among 71 callosal ROIs derived from 12 short-term cuprizone-treated animals. This analysis showed that ~87% of DDIT3-positive nuclei were within the CC1$^+$ oligodendrocytes (Figure 2f). Co-localization experiments at Day 4 with anti-NeuN antibodies to label neurons, anti-IBA1 antibodies to label microglia, or anti-GFAP antibodies to label astrocytes displayed virtually no co-localization at this time point (Figure 2f).

3.3 | Induction of ER stress pathways during early cuprizone intoxication

DDIT3 is known as a central regulator of ER stress responses (Gow & Wrabetz, 2009). We next looked for the induction of ER stress in the cuprizone model. First, gene array data (control vs. 2 days cuprizone intoxication) were manually screened for the transcriptional induction of genes related to ER stress. The following gene ontology terms were included in this search strategy: "protein folding," "endoplasmic reticulum," "ER overload response," and "endoplasmic reticulum unfolded protein response." A number of genes related to these terms displayed significantly higher expression levels in the corpus callosum of cuprizone-exposed animals compared to the controls (for abbreviations and gene ID numbers, see Supporting Information Supplementary Table S3). Induced expression of the five known DDIT3 target genes *Gadd34* (Marciniak et al., 2004), *Aars*, *Lars*, *Yars*, and *Gars* (Han et al., 2013) was verified by RT-qPCR (Figure 3a).

Another component of the ER stress response is the selective and regulated degradation of mRNA, termed regulated IRE1-dependent decay (RIDD) (Hollien et al., 2009; Maurel, Chevet, Tavernier, & Gerlo, 2014), which relieves ER stress by reducing the amount of the ER protein load. As shown in Figure 3b, the levels of oligodendrocyte-specific mRNAs were already dramatically reduced 2 days after initiation of the cuprizone intoxication. The reduction of myelin-related genes (i.e., *Plp*) was confirmed by ISH in a separate cohort of animals (Figure 3c). As another indicator of an active UPR, western-blotting experiments revealed higher protein levels of the ER resident chaperone BIP/HSPA5 (Kohno et al., 1993) (Figure 3d, upper row). Perturbation of ER homeostasis also results in protein degradation by the ubiquitin-proteasome system (Hiller, Finger, Schweiger, & Wolf, 1996). As shown in Figure 3d (lower row), profound protein ubiquitination was found in cuprizone-intoxicated mice, indicating that cuprizone-induced ER stress is paralleled by ubiquitin-dependent protein degradation. Finally, we looked for splicing of the transcription factor X-box binding protein 1 (*Xbp1*) mRNA (Calfon et al., 2002), another marker of ER stress. As demonstrated by qualitative PCR, neither the corpus callosum tissues of the control nor the cuprizone-intoxicated animals contained high levels of spliced *Xbp1* mRNA (Figure 3e). In contrast, the spliced *Xbp1* product was readily visible in the tunicamycin-treated OliNeu cells. Because splicing of *Xbp1* mRNA is transient (Marciniak et al., 2004), for a more fine-grained analysis, we quantified the ratio of spliced versus non-spliced *Xbp1* by means of the more sensitive RT-qPCR method. This analysis revealed a doubling of the spliced versus non-spliced *Xbp1* ratio, indicating a modest activation of the IRE1 pathway.

3.4 | DDIT3 regulates cuprizone-induced demyelination

Although DDIT3 is classically regarded as a mediator of pro-apoptotic signaling cascades (Feng et al., 2003; He et al., 2012; Posey et al., 2012), results of some studies suggest that DDIT3 can equally orchestrate protective events (Chen, Wu, Chiang, Liao, & Liu, 2012; Engel et al., 2013). Therefore, we investigated the relevance of DDIT3 during cuprizone-induced sequential oligodendrocyte apoptosis. As shown in Figure 4a, the densities of apoptotic oligodendrocytes were lower in *Ddit3*-deficient compared to wild type (wt) animals after 1-week of cuprizone exposure, which was paralleled by higher densities of OLIG2$^+$ oligodendrocytes. Amelioration of the cuprizone-induced oligodendrocyte apoptosis in *Ddit3*$^{-/-}$ mice was also reflected by less intense microglia activation. Because chemokines orchestrate early microglia activation in the cuprizone model (Clarner et al., 2015), we next analyzed the expression levels of *Ccl2*, *Ccl3*, and *Cxcl10*. As

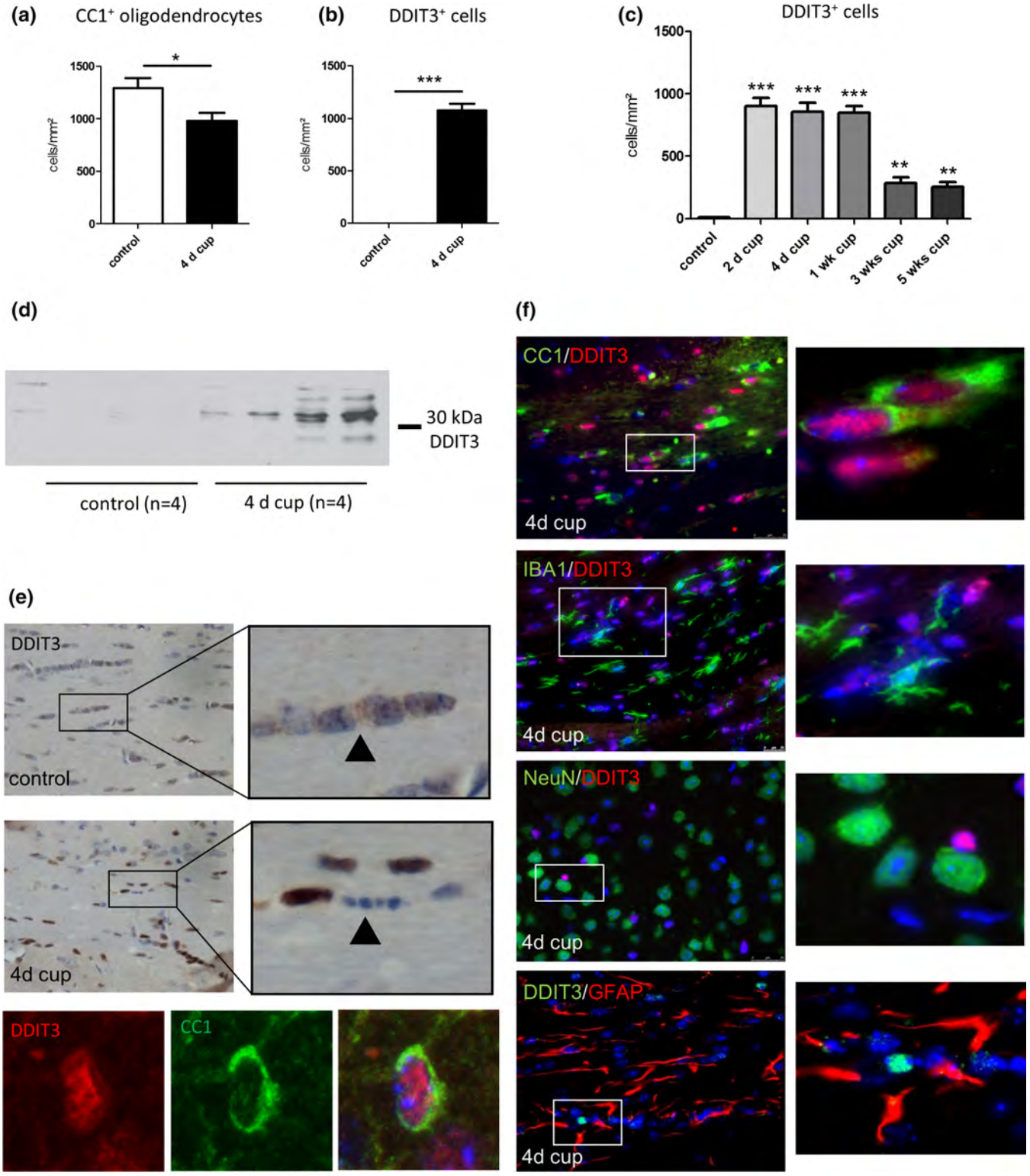

FIGURE 2 Selective expression of DNA damage-inducible transcript 3 (DDIT3) in oligodendrocytes during early cuprizone intoxication. (a) Densities of $CC1^+$ mature oligodendrocytes and (b) $DDIT3^+$ cells after 4 days of cuprizone intoxication. Six biological replicates were used. Statistical comparison was done using an unpaired *t*-test. Significant differences with respect to the control animals are indicated by $*p < .05$ or $***p < .001$. (c) Densities of the $DDIT3^+$ cells during the course of the cuprizone-induced demyelination. Six biological replicates were used. Statistical comparison was done using a one-way analysis of variance with the obtained *p* values corrected for multiple testing using the Dunnett's post hoc test. Significant differences with respect to the control animals are indicated by $**p < .01$ or $***p < .001$. (d) DDIT3-protein levels, determined by western blotting. Four biological replicates were used. (e) Representative images illustrating DDIT3 expression in the corpus callosum of control and cuprizone-intoxicated mice. Note that in the control animals, faint anti-DDIT3 staining can be observed around the cell nucleus (arrowhead), whereas in the cuprizone-exposed animals, the anti-DDIT3 signal shifts into the nucleus. The arrowhead highlights an apoptotic oligodendrocyte. (f) Representative images illustrating that DDIT3 co-localizes with $CC1^+$ mature oligodendrocytes but not with $NeuN^+$ neurons, $IBA1^+$ microglia, or $GFAP^+$ astrocytes after 4 days of cuprizone intoxication [Color figure can be viewed at wileyonlinelibrary.com]

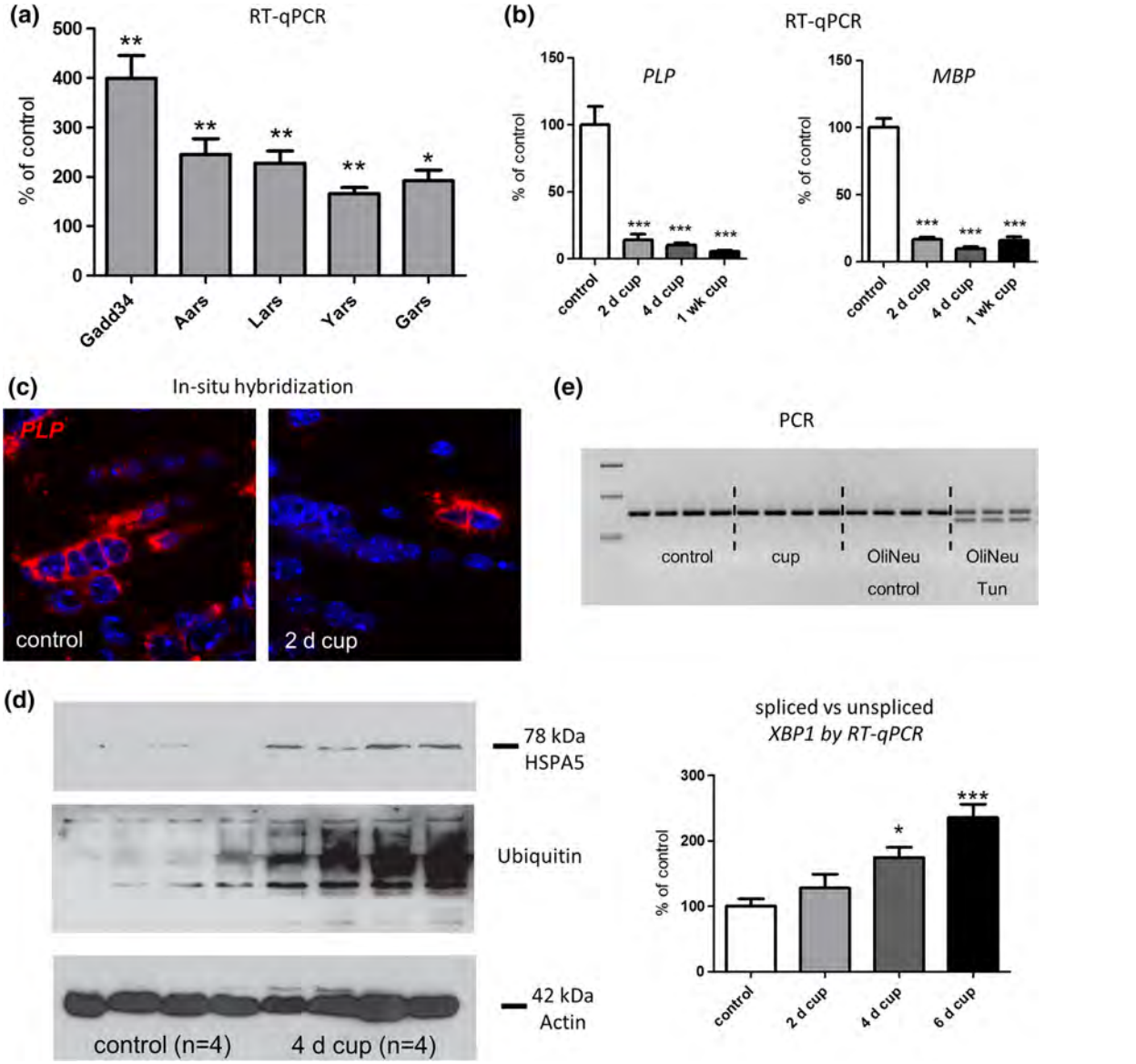

FIGURE 3 Induction of endoplasmic reticulum stress proteins in the cuprizone model. (a) Expression of DNA damage-inducible transcript 3 (DDIT3)-target genes after short-term cuprizone intoxication. Five biological replicates were used. Statistical comparison was done using an unpaired *t*-test. Significant differences with respect to the control animals are indicated by $*p < .05$ or $**p < .05$. (b, c) Early reduction of *Plp* and *Mbp* mRNA expression after short-term cuprizone intoxication, determined by real-time reverse transcription-polymerase chain reaction (RT-qPCR) (b) and in situ hybridization (c, for *Plp*). For RT-qPCR experiments at least four biological replicates were used. Statistical comparison was done using a one-way analysis of variance (ANOVA) with the obtained *p* values corrected for multiple testing using the Dunnett's post hoc test. Significant differences with respect to the control animals are indicated by $***p < .001$. (D) Induction of HSPA5 protein expression (upper row) and ubiquitination of proteins (lower row). Four biological replicates were used. (e) *Xbp1*-splicing, determined by qualitative (upper illustration) and quantitative (lower illustration) PCR. For the RT-qPCR experiments at least four biological replicates were used. Statistical comparison was done using a one-way ANOVA with the obtained *p* values corrected for multiple testing using the Dunnett's post hoc test. Significant differences with respect to the control animals are indicated by $*p < .05$ or $***p < .001$ [Color figure can be viewed at wileyonlinelibrary.com]

demonstrated in Figure 4b, expression induction of all three chemokines was less intense in *Ddit3*$^{-/-}$ compared to wt animals.

To determine whether this modest reduction of oligodendrocyte death resulted in a lasting protection from cuprizone, we examined myelination after a 3-week exposure period. As demonstrated in Figure 4c, demyelination was less severe in the corpus callosum of *Ddit3*$^{-/-}$ animals compared to the wt animals and was paralleled by a preservation of CC1^{+} mature oligodendrocytes. Furthermore, the accumulation of IBA1^{+} cells and MAC3^{+} (MAC3/LAMP2: lysosomal associated membrane protein 2) cells was less severe, indicating a diminished response of microglia cells in the Ddit3$^{-/-}$ mice. The same was true for the accumulation of ALDH1L1 (Aldehyde Dehydrogenase 1 Family Member L1)-reactive astrocytes. Because cuprizone-induced demyelination is paralleled by acute axonal damage (Hoflich et al., 2016), we investigated the densities of APP^{+} (Amyloid-Precursor-Protein)-spheroids in our cohorts. As demonstrated in Figure 4c (lower-right), the accumulation of APP^{+} spheroids was almost absent in Ddit3$^{-/-}$ mice. In summary, there is a clear protective effect of the homozygous *Ddit3* null mutation in the cuprizone model.

3.5 | DDIT3 is expressed by astrocytes and oligodendrocytes during acute demyelination

During the course of cuprizone-induced demyelination, oligodendrocyte degeneration is paralleled by the activation of astrocytes and microglia. Because innate immune responses can trigger UPR activation (Grootjans, Kaser, Kaufman, & Blumberg, 2016), we next asked if during the course of cuprizone-induced demyelination DDIT3 is expressed by cell types other than oligodendrocytes. To this end, brain sections from a separate cohort of mice were co-labeled with anti-DDIT3 antibodies and antibodies to visualize either

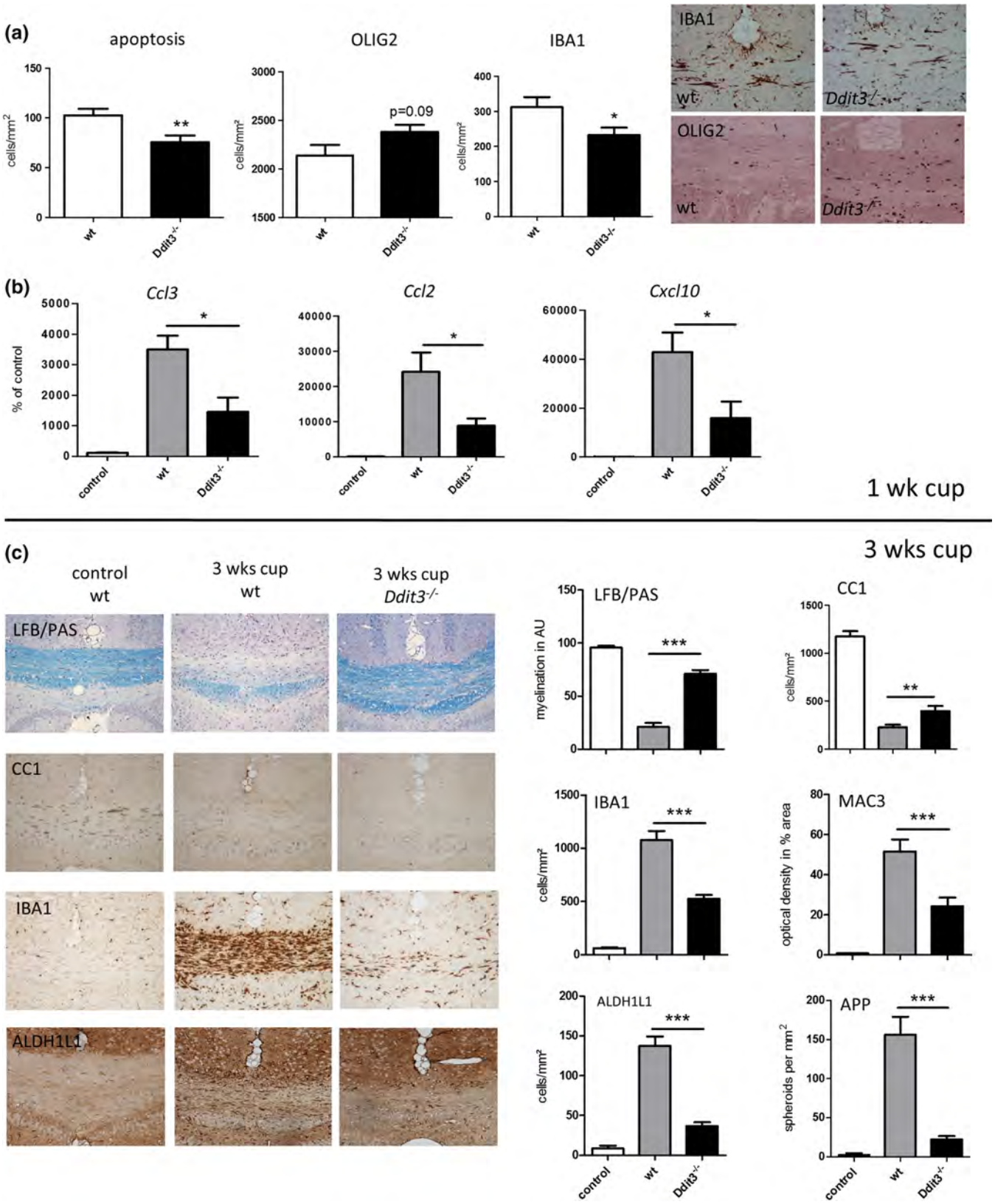

oligodendrocytes (anti-OLIG2), microglia (anti-IBA1), or astrocytes (anti-GFAP). In line with our previous results, at week 1, virtually all DDIT3$^+$ cells stained positive for OLIG2 but not GFAP or IBA1. In contrast, at weeks 3 and 5, DDIT3 was expressed by both oligodendrocytes and GFAP$^+$ astrocytes. At no time point did microglia express DDIT3 during the course of cuprizone-induced demyelination (data not shown). Astrocytes are well known to secrete diverse chemokines (Choi, Lee, Lim, Satoh, & Kim, 2014; Hennessy, Griffin, & Cunningham, 2015; Persidsky et al., 1999), and chemokines might amplify microglia activation and in consequence cuprizone-induced demyelination. Thus, we next examined whether astrocyte stimulation in vitro results in the induction of *Ddit3* expression and whether this is paralleled by an induction of chemokine expression. As demonstrated in Figure 5e, LPS-stimulated, but not SA- or INFγ-stimulated astrocyte cultures, expressed higher levels of *Ddit3*, *Ccl2*, and *Ccl3* compared to the control cultures. However, when we compared stimuli-induced chemokine expression levels in astrocyte cultures obtained from either wt or *Ddit3*$^{-/-}$ mice, no amelioration of stimuli-induced *Ccl2* or *Ccl3* expression was observed in the *Ddit3*$^{-/-}$ cultures (data not shown).

4 | DISCUSSION

This study demonstrates that oligodendrocytes display a graded vulnerability against toxin-induced demyelination, with some cells degenerating early and other cells being resistant for weeks. This graded oligodendrocyte vulnerability is most convincingly demonstrated by serial block-face SEM, which shows demyelinated internodes flanked at both sides by normal myelinated internodes. Furthermore, gene array experiments and functional studies revealed that the UPR-related transcription factor DDIT3 regulates oligodendrocyte apoptosis and subsequent demyelination in this model.

Why are oligodendrocytes selectively vulnerable (i.e., subjected to apoptosis while other cells proliferate)?

During development, myelinating cells produce an enormous amount of membrane components that wrap around the axon (Naughton, McMahon, & FitzGerald, 2015). In adults, the myelinating cells are probably less metabolically active but involved in myelin maintenance and replenishing of the myelin components that slowly turn over (Decker et al., 2006; Xing et al., 2014; Young et al., 2013). This renders oligodendrocytes specifically vulnerable at several different "Achilles' heels." First, because ATP-synthesis leads to the formation of hydrogen peroxide as a toxic by-product, oligodendrocytes are prone to experience excessive oxidative stress. On top of this, oligodendrocytes only have low levels of the anti-oxidative enzyme glutathione (GSH) (Thorburne & Juurlink, 1996). Furthermore, because of the high synthesis rate of membrane proteins, the capacity of the ER to produce and fold proteins properly seems to be a cellular "bottle neck." Therefore, simply being an oligodendrocyte seems to already put these cells at greater risk of damage under pathological conditions. In line with this assumption, we see the pro-apoptotic transcription factor DDIT3 is exclusively expressed in oligodendrocytes early after initiation of the cuprizone intoxication. At later time points (i.e., at weeks 3 and 5), DDIT3 is expressed by activated GFAP$^+$ astrocytes. Although not formally proven in this study, to the best of our knowledge, astrocyte apoptosis has never been shown in the cuprizone model (Gudi, Gingele, Skripuletz, & Stangel, 2014). This means that despite DDIT3 induction in activated astrocytes, apoptosis is not induced in this cell population. We speculate that other pro-apoptotic factors, such as the apoptosis-inducing factor (Veto et al., 2010) or ATF3 (Goldberg et al., 2013; Sun et al., 2017), have to be activated to induce apoptosis in DDIT3-expressing cells. This is best demonstrated by our findings (a) that not all DDIT3 expressing cells undergo immediate apoptosis and (b) that DDIT3 deficiency does not entirely protect against cuprizone-induced demyelination. Notably, it has been suggested that initially oligodendrocytes die because of caspase-3-dependent apoptosis, while later caspase-3-independent apoptosis predominates (Gudi et al., 2014; Veto et al., 2010). Thus, it appears that once astrocytes and/or microglia are activated, the environment influences the apoptotic machinery of the oligodendrocytes. However, the factors regulating this process are currently unknown.

Whether the robust protective effect observed at week 3 is mediated by DDIT3 deletion in oligodendrocytes or astrocytes remains to be clarified in future studies. As demonstrated in Figure 4, oligodendrocytes (i.e., OLIG2$^+$ or CC1$^+$ cells) are just moderately preserved in *Ddit3*$^{-/-}$ mice compared to wt mice. Of note, it has recently been suggested that the CC1 antigen could potentially be transiently downregulated during the course of cuprizone-induced demyelination (Xing et al., 2014). This would mean that the true extent of oligodendrocyte degeneration is underestimated in anti-CC1 stained sections. Considering the fact that global inhibition of protein translation is one of the protective UPR "strategies," it might well be that the extent of oligodendrocyte preservation in *Ddit3*$^{-/-}$ mice is the best estimated by evaluating apoptotic cell densities in H&E-stained sections. However, it is well known that the UPR influences inflammatory cytokine production on multiple levels, from stimulation of pattern recognition receptors, to modulation of inflammatory signaling pathways and the regulation of cytokine transcription factors (Smith, 2018).

FIGURE 4 Amelioration of cuprizone-induced demyelination in Ddit3$^{-/-}$ mice. (a) Densities of apoptotic cells, oligodendrocytes (OLIG2) or microglia (IBA1) after 1 week of cuprizone intoxication in wild type (wt) and Ddit3$^{-/-}$ mice. Representative images are shown on the right site. At least 14 biological replicates were used. Statistical comparison was done using an unpaired *t*-test. The *t*-test with Welch's correction was applied for the statistical comparison of IBA1 cell densities. Significant differences with respect to the control animals are indicated by $*p < .05$ or $**p < .01$. (b) Chemokine expression after 1 week of cuprizone intoxication in wt and Ddit3$^{-/-}$ mice. At least five biological replicates were used. Statistical comparison was done using an unpaired *t*-test. Significant differences between wt and Ddit3$^{-/-}$ mice are indicated by $*p < .05$. (c) Myelination (LFB/PAS), densities of the mature oligodendrocytes (CC1), microgliosis (IBA1; MAC3), astrocytosis (ALDH1L1), and the extent of acute axonal injury (APP) after 3 weeks of cuprizone intoxication in wt and Ddit3$^{-/-}$ mice. At least 14 biological replicates were used. Statistical comparison was done using an unpaired *t*-test. The *t*-test with Welch's correction was applied for the statistical comparison of IBA1, ALDH1L1, and APP cell/spheroid densities. Significant differences between wt and Ddit3$^{-/-}$ mice are indicated by $*p < .05$, $**p < .01$, or $***p < .001$ [Color figure can be viewed at wileyonlinelibrary.com]

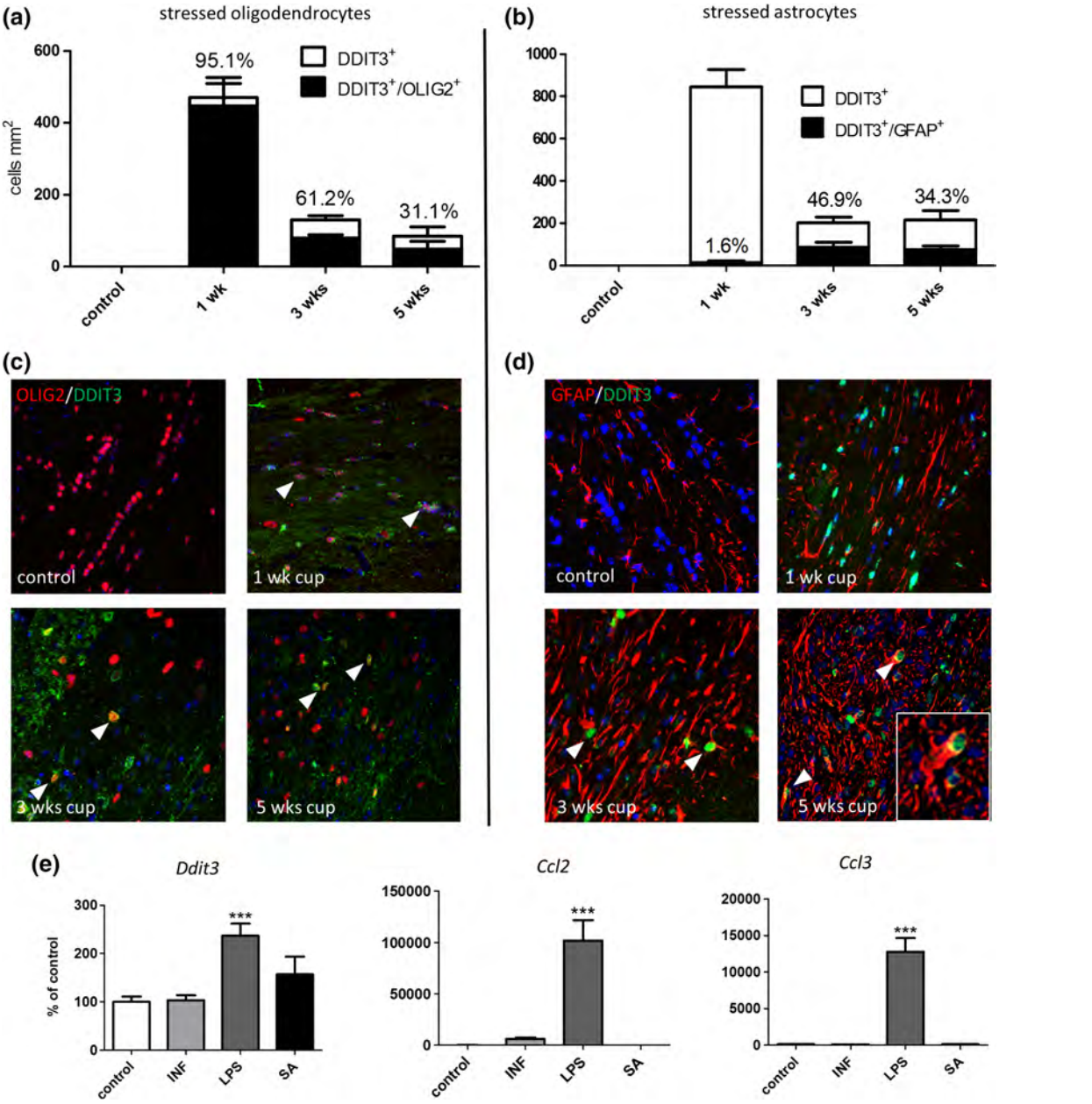

FIGURE 5 Expression of DNA damage-inducible transcript 3 (DDIT3) in oligodendrocytes and astrocytes after cuprizone-induced demyelination, and astrocytes in vitro. (a) Relative densities of DDIT3$^+$ oligodendrocytes during the course of cuprizone-induced demyelination. Three biological replicates were used. White bars indicate the total densities of DDIT3 expressing cells (DDIT3$^+$). Black bars indicate the densities of DDIT3-expressing oligodendrocytes (DDIT3$^+$/OLIG2$^+$). (b) The relative numbers of DDIT3$^+$ astrocytes during the course of cuprizone-induced demyelination. Three biological replicates were used. White bars indicate total densities of DDIT3 expressing cells (DDIT3$^+$). Black bars indicate densities of DDIT3-expressing astrocytes (DDIT3$^+$/GFAP$^+$). Note that almost half (46.9%) of the astrocytes expressed DDIT3 at week 3. (c, d) Representative images illustrating expression of DDIT3 in oligodendrocytes and astrocytes. (E) Expression of *Ddit3*, *Ccl2*, and *Ccl3* in stimulated primary astrocyte cultures. At least five biological replicates were used. Statistical comparison was done using a one-way analysis of variance with the obtained *p* values corrected for multiple testing using the Dunnett's post hoc test. Significant differences with respect to control animals are indicated by ***$p < .001$ [Color figure can be viewed at wileyonlinelibrary.com]

Consequently, the UPR/ER stress responses have been increasingly recognized in a variety of autoimmune and inflammatory diseases, including MS. Because chemokine expression can be induced during ER stress (Zhang et al., 2014), and astrocytes have been shown to release demyelination promoting chemokines (Clarner et al., 2015), DDIT3 may trigger the release of diverse chemokines by astrocytes, which in turn promote demyelination by the activation of microglia. Although we did not find any evidence of reduced *Ccl3* or *Ccl3* expression levels in *Ddit3*$^{-/-}$ primary astrocyte cultures, a broader screening approach would be required to address this aspect in more detail.

What activates the UPR in cuprizone-intoxicated mice? It is suggested that the Cu^{2+} chelating agent cuprizone causes mitochondria dysfunction leading to decreased ATP production and increased reactive oxygen species (ROS) formation (Faizi et al., 2016). In support of this assumption, we recently demonstrated that cuprizone induces the

activation of the nuclear factor erythroid 2-related factor 2 (Nrf2) pathways, which is the main transcriptional regulator of the antioxidant stress defense (Draheim et al., 2016). In parallel, brain GSH levels were decreased days after initiation of the cuprizone intoxication (unpublished data, own observations) indicating that cuprizone-induced oligodendrocyte apoptosis occurs in an oxidative stress environment. Here, we show that this metabolic disturbance induces a cellular response that shares several features of an UPR (Way & Popko, 2016), including mRNA (RIDD) and protein degradation (ERAD), increased chaperone production, and activation of ER-related apoptotic pathways (DDIT3). Indeed, it has been shown that Nrf2 is a critical UPR effector (Cullinan et al., 2003; Pajares, Cuadrado, & Rojo, 2017). The relevance of UPR activation for oligodendrocyte maintenance and (re-) myelination appears to be context dependent. For example, in a model of vanishing white matter disease, PERK activation in oligodendrocytes during development induced oligodendrocyte and myelin pathology (Lin et al., 2014). In contrast, moderate PERK activation in response to ER stress preserves the viability and function of myelin-producing cells (Lin & Popko, 2009). Another study showed that DDIT3 induction promotes survival of ER-stressed myelinating oligodendrocytes in a mouse model of Pelizaeus-Merzbacher disease (Southwood, Garbern, Jiang, & Gow, 2002). We provide strong and convincing evidence that in the applied metabolic oligodendrocyte injury model, DDIT3 exerts pro-apoptotic effects and promotes demyelination. Notably, key markers of the UPR pathway, including DDIT3, are upregulated in brain tissue from patients with MS (Cunnea et al., 2011; McMahon, McQuaid, Reynolds, & FitzGerald, 2012; Mhaille et al., 2008). Thus, our findings might well have direct relevance for the human disease.

It is currently unknown why oligodendrocytes display a graded vulnerability against toxin-induced demyelination; however, differences in the amount of myelin produced by a single oligodendrocyte might render them more or less susceptible against any kind of metabolic injury. For example, the length and number of internodes myelinated by a single oligodendrocyte varies substantially (Young et al., 2013). In one study, adult-born oligodendrocytes elaborated much shorter but many more internodes than oligodendrocytes generated during early postnatal life (Young et al., 2013). In another study, three-dimensional analysis of optic nerve oligodendrocyte processes showed that the number of internodes myelinated by a single mature oligodendrocyte range from 12 to 35 and the length of internodes ranges from 50 to 350 microns (Butt, Colquhoun, Tutton, & Berry, 1994). Furthermore, studies that have estimated the number of sheaths maintained by individual oligodendrocytes and the internodal lengths of individual myelin sheaths indicate an inverse relationship with fiber diameter (Blakemore & Murray, 1981; Hess & Young, 1949; McDonald & Ohlrich, 1971). We speculate that those oligodendrocytes that die early after the initiation of the cuprizone-induced demyelination process are the ones myelinating thicker axons and thus providing more myelin to the axons. Future studies need to show whether this is true and whether such oligodendrocytes are more prone to ER-stress.

In summary, this study provides strong evidence that at least parts of the cuprizone-induced demyelinating effects are mediated by an active UPR, in particular by DDIT3. Manipulation of this pathway might be an attractive therapeutic option to ameliorate oligodendrocyte degeneration and subsequent demyelination in various neurological diseases, including MS.

ACKNOWLEDGMENTS

This work was supported by the Robert-Pfleger Stiftung and the Deutsche Forschungsgemeinschaft (KI 1469/8-1; M.K.). We thank Petra Ibold, Helga Helten, and Sarah Wübbel for their excellent and valuable technical assistance.

ORCID

Markus Kipp https://orcid.org/0000-0001-5043-9052

REFERENCES

Baertling, F., Kokozidou, M., Pufe, T., Clarner, T., Windoffer, R., Wruck, C. J., … Kipp, M. (2010). ADAM12 is expressed by astrocytes during experimental demyelination. *Brain Research*, *1326*, 1–14. https://doi.org/10.1016/j.brainres.2010.02.049

Blakemore, W. F., & Murray, J. A. (1981). Quantitative examination of internodal length of remyelinated nerve fibres in the central nervous system. *Journal of the Neurological Sciences*, *49*(2), 273–284.

Braun, A., Dang, J., Johann, S., Beyer, C., & Kipp, M. (2009). Selective regulation of growth factor expression in cultured cortical astrocytes by neuro-pathological toxins. *Neurochemistry International*, *55*(7), 610–618. https://doi.org/10.1016/j.neuint.2009.06.004

Butt, A. M., Colquhoun, K., Tutton, M., & Berry, M. (1994). Three-dimensional morphology of astrocytes and oligodendrocytes in the intact mouse optic nerve. *Journal of Neurocytology*, *23*(8), 469–485.

Calfon, M., Zeng, H., Urano, F., Till, J. H., Hubbard, S. R., Harding, H. P., … Ron, D. (2002). IRE1 couples endoplasmic reticulum load to secretory capacity by processing the XBP-1 mRNA. *Nature*, *415*(6867), 92–96. https://doi.org/10.1038/415092a

Chen, C. M., Wu, C. T., Chiang, C. K., Liao, B. W., & Liu, S. H. (2012). C/EBP homologous protein (CHOP) deficiency aggravates hippocampal cell apoptosis and impairs memory performance. *PLoS One*, *7*(7), e40801. https://doi.org/10.1371/journal.pone.0040801 PONE-D-12-06584

Choi, S. S., Lee, H. J., Lim, I., Satoh, J., & Kim, S. U. (2014). Human astrocytes: Secretome profiles of cytokines and chemokines. *PLoS One*, *9*(4), e92325. https://doi.org/10.1371/journal.pone.0092325

Clarner, T., Janssen, K., Nellessen, L., Stangel, M., Skripuletz, T., Krauspe, B., … Kipp, M. (2015). CXCL10 triggers early microglial activation in the cuprizone model. *Journal of Immunology*, *194*(7), 3400–3413. https://doi.org/10.4049/jimmunol.1401459

Cullinan, S. B., Zhang, D., Hannink, M., Arvisais, E., Kaufman, R. J., & Diehl, J. A. (2003). Nrf2 is a direct PERK substrate and effector of PERK-dependent cell survival. *Molecular and Cellular Biology*, *23*(20), 7198–7209.

Cunnea, P., Mhaille, A. N., McQuaid, S., Farrell, M., McMahon, J., & FitzGerald, U. (2011). Expression profiles of endoplasmic reticulum stress-related molecules in demyelinating lesions and multiple sclerosis. *Multiple Sclerosis*, *17*(7), 808–818. https://doi.org/10.1177/1352458511399114

Decker, L., Desmarquet-Trin-Dinh, C., Taillebourg, E., Ghislain, J., Vallat, J. M., & Charnay, P. (2006). Peripheral myelin maintenance is a dynamic process requiring constant Krox20 expression. *The Journal of Neuroscience*, *26*(38), 9771–9779. https://doi.org/10.1523/jneurosci.0716-06.2006

Draheim, T., Liessem, A., Scheld, M., Wilms, F., Weissflog, M., Denecke, B., … Clarner, T. (2016). Activation of the astrocytic Nrf2/ARE system ameliorates the formation of demyelinating lesions in a multiple sclerosis animal model. *Glia*, *64*(12), 2219–2230. https://doi.org/10.1002/glia.23058

Edgar, J. M., McLaughlin, M., Yool, D., Zhang, S. C., Fowler, J. H., Montague, P., … Griffiths, I. R. (2004). Oligodendroglial modulation of fast axonal transport in a mouse model of hereditary spastic paraplegia. *The Journal of Cell Biology*, *166*(1), 121–131. https://doi.org/10.1083/jcb.200312012

Engel, T., Sanz-Rodgriguez, A., Jimenez-Mateos, E. M., Concannon, C. G., Jimenez-Pacheco, A., Moran, C., … Henshall, D. C. (2013). CHOP regulates the p53-MDM2 axis and is required for neuronal survival after seizures. *Brain*, *136*(Pt 2), 577–592. doi: aws337 [pii] https://doi.org/10.1093/brain/aws337

Faizi, M., Salimi, A., Seydi, E., Naserzadeh, P., Kouhnavard, M., Rahimi, A., & Pourahmad, J. (2016). Toxicity of cuprizone a Cu(2+) chelating agent on isolated mouse brain mitochondria: A justification for demyelination and subsequent behavioral dysfunction. *Toxicology Mechanisms and Methods*, *26*(4), 276–283. https://doi.org/10.3109/15376516.2016.1172284

Feng, B., Yao, P. M., Li, Y., Devlin, C. M., Zhang, D., Harding, H. P., … Tabas, I. (2003). The endoplasmic reticulum is the site of cholesterol-induced cytotoxicity in macrophages. *Nature Cell Biology*, *5*(9), 781–792. https://doi.org/10.1038/ncb1035 ncb1035 [pii]

Funfschilling, U., Supplie, L. M., Mahad, D., Boretius, S., Saab, A. S., Edgar, J., … Nave, K. A. (2012). Glycolytic oligodendrocytes maintain myelin and long-term axonal integrity. *Nature*, *485*(7399), 517–521. https://doi.org/10.1038/nature11007

Goldberg, J., Daniel, M., van Heuvel, Y., Victor, M., Beyer, C., Clarner, T., & Kipp, M. (2013). Short-term cuprizone feeding induces selective amino acid deprivation with concomitant activation of an integrated stress response in oligodendrocytes. *Cellular and Molecular Neurobiology*, *33*(8), 1087–1098. https://doi.org/10.1007/s10571-013-9975-y

Gow, A., & Wrabetz, L. (2009). CHOP and the endoplasmic reticulum stress response in myelinating glia. *Current Opinion in Neurobiology*, *19*(5), 505–510. https://doi.org/10.1016/j.conb.2009.08.007

Grootjans, J., Kaser, A., Kaufman, R. J., & Blumberg, R. S. (2016). The unfolded protein response in immunity and inflammation. *Nature Reviews. Immunology*, *16*(8), 469–484. https://doi.org/10.1038/nri.2016.62

Gudi, V., Gingele, S., Skripuletz, T., & Stangel, M. (2014). Glial response during cuprizone-induced de- and remyelination in the CNS: Lessons learned. *Frontiers in Cellular Neuroscience*, *8*, 73. https://doi.org/10.3389/fncel.2014.00073

Han, J., Back, S. H., Hur, J., Lin, Y. H., Gildersleeve, R., Shan, J., … Kaufman, R. J. (2013). ER-stress-induced transcriptional regulation increases protein synthesis leading to cell death. *Nature Cell Biology*, *15*(5), 481–490. https://doi.org/10.1038/ncb2738

He, Z., Ostrowski, R. P., Sun, X., Ma, Q., Huang, B., Zhan, Y., & Zhang, J. H. (2012). CHOP silencing reduces acute brain injury in the rat model of subarachnoid hemorrhage. *Stroke*, *43*(2), 484–490. https://doi.org/10.1161/strokeaha.111.626432

Hennessy, E., Griffin, E. W., & Cunningham, C. (2015). Astrocytes are primed by chronic neurodegeneration to produce exaggerated chemokine and cell infiltration responses to acute stimulation with the cytokines IL-1beta and TNF-alpha. *The Journal of Neuroscience*, *35*(22), 8411–8422. https://doi.org/10.1523/jneurosci.2745-14.2015

Hess, A., & Young, J. Z. (1949). Correlation of internodal length and fibre diameter in the central nervous system. *Nature*, *164*(4168), 490–491.

Hesse, A., Wagner, M., Held, J., Bruck, W., Salinas-Riester, G., Hao, Z., … Kuhlmann, T. (2010). In toxic demyelination oligodendroglial cell death occurs early and is FAS independent. *Neurobiology of Disease*, *37*(2), 362–369. https://doi.org/10.1016/j.nbd.2009.10.016

Hiller, M. M., Finger, A., Schweiger, M., & Wolf, D. H. (1996). ER degradation of a misfolded luminal protein by the cytosolic ubiquitin-proteasome pathway. *Science*, *273*(5282), 1725–1728.

Hochstrasser, T., Exner, G. L., Nyamoya, S., Schmitz, C., & Kipp, M. (2017). Cuprizone-containing pellets are less potent to induce consistent demyelination in the corpus callosum of C57BL/6 mice. *Journal of Molecular Neuroscience*, *61*(4), 617–624. https://doi.org/10.1007/s12031-017-0903-3

Hoflich, K. M., Beyer, C., Clarner, T., Schmitz, C., Nyamoya, S., Kipp, M., & Hochstrasser, T. (2016). Acute axonal damage in three different murine models of multiple sclerosis: A comparative approach. *Brain Research*, *1650*, 125–133. https://doi.org/10.1016/j.brainres.2016.08.048

Hollien, J., Lin, J. H., Li, H., Stevens, N., Walter, P., & Weissman, J. S. (2009). Regulated Ire1-dependent decay of messenger RNAs in mammalian cells. *The Journal of Cell Biology*, *186*(3), 323–331. https://doi.org/10.1083/jcb.200903014

Kohno, K., Normington, K., Sambrook, J., Gething, M. J., & Mori, K. (1993). The promoter region of the yeast KAR2 (BiP) gene contains a regulatory domain that responds to the presence of unfolded proteins in the endoplasmic reticulum. *Molecular and Cellular Biology*, *13*(2), 877–890.

Kozutsumi, Y., Segal, M., Normington, K., Gething, M. J., & Sambrook, J. (1988). The presence of malfolded proteins in the endoplasmic reticulum signals the induction of glucose-regulated proteins. *Nature*, *332*(6163), 462–464. https://doi.org/10.1038/332462a0

Krauspe, B. M., Dreher, W., Beyer, C., Baumgartner, W., Denecke, B., Janssen, K., … Kipp, M. (2015). Short-term cuprizone feeding verifies N-acetylaspartate quantification as a marker of neurodegeneration. *Journal of Molecular Neuroscience*, *55*(3), 733–748. https://doi.org/10.1007/s12031-014-0412-6

Lin, W., & Popko, B. (2009). Endoplasmic reticulum stress in disorders of myelinating cells. *Nature Neuroscience*, *12*(4), 379–385. https://doi.org/10.1038/nn.2273

Lin, Y., Pang, X., Huang, G., Jamison, S., Fang, J., Harding, H. P., … Lin, W. (2014). Impaired eukaryotic translation initiation factor 2B activity specifically in oligodendrocytes reproduces the pathology of vanishing white matter disease in mice. *The Journal of Neuroscience*, *34*(36), 12182–12191. https://doi.org/10.1523/jneurosci.1373-14.2014

Lucchinetti, C., Bruck, W., Parisi, J., Scheithauer, B., Rodriguez, M., & Lassmann, H. (1999). A quantitative analysis of oligodendrocytes in multiple sclerosis lesions. A study of 113 cases. *Brain*, *122*(Pt 12), 2279–2295.

Marciniak, S. J., Yun, C. Y., Oyadomari, S., Novoa, I., Zhang, Y., Jungreis, R., … Ron, D. (2004). CHOP induces death by promoting protein synthesis and oxidation in the stressed endoplasmic reticulum. *Genes & Development*, *18*(24), 3066–3077. https://doi.org/10.1101/gad.1250704

Maurel, M., Chevet, E., Tavernier, J., & Gerlo, S. (2014). Getting RIDD of RNA: IRE1 in cell fate regulation. *Trends in Biochemical Sciences*, *39*(5), 245–254. https://doi.org/10.1016/j.tibs.2014.02.008

McDonald, W. I., & Ohlrich, G. D. (1971). Quantitative anatomical measurements on single isolated fibres from the cat spinal cord. *Journal of Anatomy*, *110*(Pt 2), 191–202.

McMahon, J. M., McQuaid, S., Reynolds, R., & FitzGerald, U. F. (2012). Increased expression of ER stress- and hypoxia-associated molecules in grey matter lesions in multiple sclerosis. *Multiple Sclerosis*, *18*(10), 1437–1447. https://doi.org/10.1177/1352458512438455

Mhaille, A. N., McQuaid, S., Windebank, A., Cunnea, P., McMahon, J., Samali, A., & FitzGerald, U. (2008). Increased expression of endoplasmic reticulum stress-related signaling pathway molecules in multiple sclerosis lesions. *Journal of Neuropathology and Experimental Neurology*, *67*(3), 200–211. https://doi.org/10.1097/NEN.0b013e318165b239

Naughton, M. C., McMahon, J. M., & FitzGerald, U. (2015). Differential activation of ER stress pathways in myelinating cerebellar tracts. *International Journal of Developmental Neuroscience*, *47*(Pt B), 347–360. https://doi.org/10.1016/j.ijdevneu.2015.08.002

Ohno, N., Chiang, H., Mahad, D. J., Kidd, G. J., Liu, L., Ransohoff, R. M., … Trapp, B. D. (2014). Mitochondrial immobilization mediated by syntaphilin facilitates survival of demyelinated axons. *Proceedings of the National Academy of Sciences of the United States of America*, *111*(27), 9953–9958. https://doi.org/10.1073/pnas.1401155111

Pajares, M., Cuadrado, A., & Rojo, A. I. (2017). Modulation of proteostasis by transcription factor NRF2 and impact in neurodegenerative diseases. *Redox Biology*, *11*, 543–553. https://doi.org/10.1016/j.redox.2017.01.006

Persidsky, Y., Ghorpade, A., Rasmussen, J., Limoges, J., Liu, X. J., Stins, M., … Gendelman, H. E. (1999). Microglial and astrocyte chemokines regulate monocyte migration through the blood-brain barrier in human immunodeficiency virus-1 encephalitis. *The American Journal of Pathology*, *155*(5), 1599–1611. https://doi.org/10.1016/s0002-9440(10)65476-4

Posey, K. L., Coustry, F., Veerisetty, A. C., Liu, P., Alcorn, J. L., & Hecht, J. T. (2012). Chop (Ddit3) is essential for D469del-COMP retention and cell death in chondrocytes in an inducible transgenic mouse model of pseudoachondroplasia. *The American Journal of Pathology*,

180(2), 727–737. doi: S0002-9440(11)01028-5 [pii] https://doi.org/10.1016/j.ajpath.2011.10.035

Ruther, B. J., Scheld, M., Dreymueller, D., Clarner, T., Kress, E., Brandenburg, L. O., … Kipp, M. (2017). Combination of cuprizone and experimental autoimmune encephalomyelitis to study inflammatory brain lesion formation and progression. *Glia*, *65*(12), 1900–1913. https://doi.org/10.1002/glia.23202

Sanadgol, N., Golab, F., Tashakkor, Z., Taki, N., Moradi Kouchi, S., Mostafaie, A., … Sharifzadeh, M. (2017). Neuroprotective effects of ellagic acid on cuprizone-induced acute demyelination through limitation of microgliosis, adjustment of CXCL12/IL-17/IL-11 axis and restriction of mature oligodendrocytes apoptosis. *Pharmaceutical Biology*, *55*(1), 1679–1687. https://doi.org/10.1080/13880209.2017.1319867

Slowik, A., Schmidt, T., Beyer, C., Amor, S., Clarner, T., & Kipp, M. (2015). The sphingosine 1-phosphate receptor agonist FTY720 is neuroprotective after cuprizone-induced CNS demyelination. *British Journal of Pharmacology*, *172*(1), 80–92. https://doi.org/10.1111/bph.12938

Smith, J. A. (2018). Regulation of cytokine production by the unfolded protein response; implications for infection and autoimmunity. *Frontiers in Immunology*, *9*, 422. https://doi.org/10.3389/fimmu.2018.00422

Southwood, C. M., Garbern, J., Jiang, W., & Gow, A. (2002). The unfolded protein response modulates disease severity in Pelizaeus-Merzbacher disease. *Neuron*, *36*(4), 585–596.

Sun, M. M., Wang, Y. C., Li, Y., Guo, X. D., Chen, Y. M., & Zhang, Z. Z. (2017). Effect of ATF3-deletion on apoptosis of cultured retinal ganglion cells. *International Journal of Ophthalmology*, *10*(5), 691–695. https://doi.org/10.18240/ijo.2017.05.05

Teske, N., Liessem, A., Fischbach, F., Clarner, T., Beyer, C., Wruck, C., … Kipp, M. (2018). Chemical hypoxia-induced integrated stress response activation in oligodendrocytes is mediated by the transcription factor nuclear factor (erythroid-derived 2)-like 2 (NRF2). *Journal of Neurochemistry*, *144*(3), 285–301. https://doi.org/10.1111/jnc.14270

Thorburne, S. K., & Juurlink, B. H. (1996). Low glutathione and high iron govern the susceptibility of oligodendroglial precursors to oxidative stress. *Journal of Neurochemistry*, *67*(3), 1014–1022.

Uschkureit, T., Sporkel, O., Stracke, J., Bussow, H., & Stoffel, W. (2000). Early onset of axonal degeneration in double (plp−/−mag−/−) and hypomyelinosis in triple (plp−/−mbp−/−mag−/−) mutant mice. *The Journal of Neuroscience*, *20*(14), 5225–5233.

Veto, S., Acs, P., Bauer, J., Lassmann, H., Berente, Z., Setalo, G., Jr., … Illes, Z. (2010). Inhibiting poly(ADP-ribose) polymerase: A potential therapy against oligodendrocyte death. *Brain*, *133*(Pt 3), 822–834. https://doi.org/10.1093/brain/awp337

Way, S. W., & Popko, B. (2016). Harnessing the integrated stress response for the treatment of multiple sclerosis. *Lancet Neurology*, *15*(4), 434–443. https://doi.org/10.1016/s1474-4422(15)00381-6

Xing, B., Brink, L. E., Maers, K., Sullivan, M. L., Bodnar, R. J., Stolz, D. B., & Cambi, F. (2018). Conditional depletion of GSK3b protects oligodendrocytes from apoptosis and lessens demyelination in the acute cuprizone model. *Glia*, *0*, 1–14. https://doi.org/10.1002/glia.23453

Xing, Y. L., Roth, P. T., Stratton, J. A., Chuang, B. H., Danne, J., Ellis, S. L., … Merson, T. D. (2014). Adult neural precursor cells from the subventricular zone contribute significantly to oligodendrocyte regeneration and remyelination. *The Journal of Neuroscience*, *34*(42), 14128–14146. https://doi.org/10.1523/jneurosci.3491-13.2014

Young, K. M., Psachoulia, K., Tripathi, R. B., Dunn, S. J., Cossell, L., Attwell, D., … Richardson, W. D. (2013). Oligodendrocyte dynamics in the healthy adult CNS: Evidence for myelin remodeling. *Neuron*, *77*(5), 873–885. https://doi.org/10.1016/j.neuron.2013.01.006

Zhang, Y., Liao, S., Fan, W., Wei, W., Wang, C., & Sun, S. (2014). Tunicamycin-induced ER stress regulates chemokine CCL5 expression and secretion via STAT3 followed by decreased transmigration of MCF-7 breast cancer cells. *Oncology Reports*, *32*(6), 2769–2776. https://doi.org/10.3892/or.2014.3479

SUPPORTING INFORMATION

Additional supporting information may be found online in the Supporting Information section at the end of the article.

How to cite this article: Fischbach F, Nedelcu J, Leopold P, et al. Cuprizone-induced graded oligodendrocyte vulnerability is regulated by the transcription factor DNA damage-inducible transcript 3. *Glia*. 2019;67:263–276. https://doi.org/10.1002/glia.23538

Supplements Veröffentlichung I

Primary antibodies							
Antigen	**Manufacturer**	**Order number**	**Host**	**RRID**	**Dilution**	**Application**	**AGR**
ß-Actin	Sigma	A5060	rabbit	AB 476738	1:2000	Western blotting	not applicable
ALDH1L1	Abcam	ab-87117	rabbit	AB 10712968	1:1000	Immunohistochemistry	none
ATF3	Santa Cruz	Sc-188	rabbit	AB 2258513	1:200	Immunohistochemistry	Citrat buffer (pH 6.0)
ATF3	Santa Cruz	Sc-188	rabbit	AB 2258513	1:100	Immunoflourescence	Citrat buffer (pH 6.0)
CC1	Millipore	OP80	mouse	AB 2057371	1:100	Immunoflourescence	Tris/EDTA buffer (pH 9.0)
DDIT3	Santa Cruz	Sc-575	rabbit	AB 631365	1:400	Immunohistochemistry	Tris/EDTA buffer (pH 9.0)
DDIT3	Santa Cruz	Sc-575	rabbit	AB 631365	1:200	Immunoflourescence	Tris/EDTA buffer (pH 9.0)
DDIT3	Abcam	ab-11419	mouse	AB 298023	1:50	Immunoflourescence	Tris/EDTA buffer (pH 9.0)
DDIT3	Cell Signaling	2895	mouse	AB 2089254	1:1000	Western blotting	not applicable
GFAP	Abcam	ab-4674	chicken	AB 304558	1:1000	Immunoflourescence	Tris/EDTA buffer (pH 9.0)
IBA1	Abcam	ab-107159	goat	AB 10972670	1:2000	Immunohistochemistry	Tris/EDTA buffer (pH 9.0)
IBA1	Abcam	ab-107159	goat	AB 10972670	1:1000	Immunohistochemistry	Tris/EDTA buffer (pH 9.0)
IBA1	Wako	019-19741	rabbit	AB 839504	1:500	Immunoflourescence	Tris/EDTA buffer (pH 9.0)
MAC3	BD Pharmigen	550292	rat	AB 393587	1:800	Immunohistochemistry	Tris/EDTA buffer (pH 9.0)
NeuN	Millipore	MAB377	mouse	AB 2298772	1:2000	Immunoflourescence	Tris/EDTA buffer (pH 9.0)
OLIG2	Millipore	AB9610	rabbit	AB 570666	1:2000	Immunohistochemistry	Tris/EDTA buffer (pH 9.0)
OLIG2	Millipore	AB9610	rabbit	AB 570666	1:1000	Immunoflourescence	Tris/EDTA buffer (pH 9.0)
OLIG2	Millipore	MABN50	mouse	AB 10807410	1:200	Immunohistochemistry	Tris/EDTA buffer (pH 9.0)
OLIG2	Millipore	MABN50	mouse	AB 10807410	1:100	Immunoflourescence	Tris/EDTA buffer (pH 9.0)
PLP	Biorad	MCA839G	mouse	AB 2237198	1:5000	Immunohistochemistry	none
Ubiquitin	Dako	Z0458	rabbit	AB 2315524	1:1000	Western blotting	not applicable
Biotinylated secondary antibodies							
horse anti-mouse IgG	Vector	BA-2000	horse	AB 2313581	1:200		not applicable
goat anti-rabbit IgG	Vector	BA-1000	goat	AB 2313606	1:200	Imunnohistochemistry	not applicable
goat anti-rat IgG	Vector	BA-9400	goat	AB 2336202	1:200	Imunnohistochemistry	not applicable
goat anti-mouse IgG	Vector	BA-9200	goat	AB 2336171	1:200	Imunohistochemistry/-fluorescendce	not applicable
rabbit anti-goat IgG	Vector	BA-5000	rabbit	AB 2336126	1:200	Immunohistochemistry	not applicable
ABC Peroxidase Kit	Vectastain	PK-6100	avidin biotin complex	AB 2336819	1:50	Immunohistochemistry	not applicable
goat anti-rabbit	Cell Signaling	7074	goat	AB 2099233	1:1000	Western blotting	not applicable
goat anti-mouse	Cell Signaling	7076	goat	AB_330924	1:1000	Western blotting	not applicable
Flourescent secondary antibodies							
Alexa Fluor 488	Thermo Fisher Scientific	A11008	goat anti-rabbit	AB 143165	1:500	Immunofluorescence	not applicable
Alexa Fluor 488	Thermo Fisher Scientific	A21206	donkey anti-rabbit	AB 141708	1:500	Immunofluorescence	not applicable
Alexa Fluor 488	Thermo Fisher Scientific	A11055	donkey anti-goat	AB 2534102	1:500	Immunofluorescence	not applicable
Alexa Fluor 546	Thermo Fisher Scientific	A21133	goat anti-mouse	AB 2535772	1:500	Immunofluorescence	not applicable
Alexa Fluor 594	Thermo Fisher Scientific	A11042	goat anti-chicken	AB 142803	1:500	Immunofluorescence	not applicable
Alexa Fluor 594	Thermo Fisher Scientific	A21207	donkey anti-rabbit	AB 141637	1:500	Immunofluorescence	not applicable
Alexa Fluor 594	Thermo Fisher Scientific	A11058	donkey anti-goat	AB 2534105	1:500	Immunofluorescence	not applicable
Alexa Fluor 594	Thermo Fisher Scientific	A21203	donkey anti-mouse	AB 141633	1:500	Immunofluorescence	not applicable
Streptavidin Alexa Fluor 488	Thermo Fisher Scientific	S11223	streptavidin	AB 2336881	1:100	Immunofluorescence	not applicable

Supplementary Table 1: List of antibodies used. Different antibodies targeting the same antigen were used for different applications. The respective applications are provided in the "APPLICATION" column. RRID (Research Resource Identifiers)

Supplementary Table 2 List of primers used

Symbol	Name	Synonyms	sense	anstisense	AT in °C	product length in bp
Ppp1r15a	protein phosphatase 1, regulatory (inhibitor) subunit 15A	Gadd34, Myd116				
Aars	alanyl-tRNA synthetase		5'-ATG GAT GCC ACT TTA ACA GCA-3'	5'-TGG GTC GAT TGT GTT TAG GAA GA-3'	63	177
Lars	leucyl-tRNA synthetase		5'-CAT TTG GGA CAC ACG TTT TCC-3'	5'-GCA TAC CAG TAC AGT GCA ACC-3'	63	108
Yars	tyrosyl-tRNA synthetase		5'-TTA TCA AAG GCA CCG ACT ACC A-3'	5'-CGT CGT GTT GTG TGA CCA C-3'	63	83
Gars	glycyl-tRNA synthetase		5'-GGA GGC AGC ACT TTA TCC AAG-3'	5'-TCG GAA GCA CTC TCC GTT CT-3'	63	154
Plp	proteolipid protein (myelin) 1		5'-TGG CGA CTA CAA GAC CAC CA-3'	5'-GAC ACA CCC GCT CCA AAG AA-3'	60	115
MBP	myelin basic protein		5'-CCC AAA GAA TAA CTG GCA AGG C-3'	5'-GAA GCT CGT CGG ACT CTG AG-3'	56	136
18s	18S ribosomal RNA		5'-CGG CTA CCA CAT CCA AGG AA-3'	5'-GCT GGA ATT ACC GCG GCT-3'	60	187
Hprt1	hypoxanthine guanine phosphoribosyl transferase 1		5'-GCT GGT GAA AAG GAC CTC T-3'	5'-CAC AGG ACT AGA ACA CCT GC-3'	62	249
Ccl2	chemokine (C-C motif) ligand 2	MCP1	5'-TTA AAA ACC TGG ATC GGA ACC AA-3'	5'-GCA TTA GCT TCA GAT TTA CGG GT-3'	60	120
Ccl3	chemokine (C-C motif) ligand 3	MIP1a	5'-TTC TCT GTA CCA TGA CAC TCT GC-3'	5'-CGT GGA ATC TTC CGG CTG TAG-3'	62	99
Cxcl10	chemokine (C-X-C motif) ligand 10	IP10	5'-CCA AGT GCT GCC GTC ATT TTC-3'	5'-GGC TCG CAG GGA TGA TTT CAA-3'	62	157
Xbp-1 (unspliced)	X-box binding protein 1		5'-GAC AGA GAG TCA AAC TAA CGT GG-3'	5'-GCT CAG CAG GCA AGA AGG T-3'	59	190
Xbp-1 (spliced)	X-box binding protein 1		5'-AAG AAC ACG CTT GGG AAT GG-3'	5'-CTG CAC CTG CTG CGG AC-3'	63	113
Xbp-1 (qualitative PCR)	X-box binding protein 1		5'-ACA CGC TTG GGA ATG GAC AC-3'	5'-CCA TGG GAA GAT GTT CTG GG-3'	59	171 and 145

Gene name	Gene product	Gene-ID
Aars	Alanyl-TRNA Synthetase	234734
Alg8	ALG8, Alpha-1,3-Glucosyltransferase	381903
Calu	Calumenin	12321
Ccnd1	Cyclin D1	12443
Cln8	Ceroid-Lipofuscinosis, Neuronal 8	26889
Creb3l1	CAMP Responsive Element Binding Protein 3-Like 1	26427
Ddit3	DNA-Damage-Inducible Transcript 3	13198
Derl1	Derlin 1	67819
Dnaja3	DnaJ (Hsp40) Homolog, Subfamily A, Member 3	83945
Edem1	ER Degradation Enhancer, Mannosidase Alpha-Like 1	192193
Ero1l	Endoplasmic Reticulum Oxidoreductase Alpha	30001
Fads3	Fatty Acid Desaturase 3	60527
Gusb	Glucuronidase, Beta	110006
Hax1	HCLS1 Associated Protein X-1	23897
HMOX1	heme oxygenase (decycling) 1	15368
Hspa9	Heat Shock 70kDa Protein 9 (Mortalin)	15526
Moxd1	Monooxygenase, DBH-Like 1	59012
Nfe2l2	Nuclear Factor, Erythroid 2-Like 2	18024
Plcd4	Phospholipase C, Delta 4	18802
Ppp1r15b	Protein Phosphatase 1, Regulatory Subunit 15B	108954
Prnp	Prion Protein	19122
Rab21	RAB21, Member RAS Oncogene Family	216344
Sec24a	SEC24 Homolog A, COPII Coat Complex Component	77371
Sel1l	Sel-1 Suppressor Of Lin-12-Like	20338
Sgpl1	Sphingosine-1-Phosphate Lyase 1	20397
Slc24a6	Solute Carrier Family 8 (Sodium/Lithium/Calcium Exchanger), Member B1	170756
Tor3a	Torsin Family 3, Member A	30935
Trp53	Tumor Protein P53	22059
Tubb6	Tubulin, Beta 6 Class V	67951
Ube2g2	Ubiquitin-Conjugating Enzyme E2G 2	22213
Uxt	Ubiquitously-Expressed, Prefoldin-Like Chaperone	22294

Supplementary Table 3 List of UPR-related genes found to be induced after 2 days of cuprizone intoxication, (UPR = unfolded protein response)

Veröffentlichung II

Zahn J, Yakimov V, Rühling S, Fischbach F, Nikolova E, Joost S, Kaddatz H, Greiner T, Frenz J, Holzmann C, Kipp M: , High Speed Ventral Plane Videography as a Convenient Tool to Quantify Motor Deficits during Pre-Clinical ExperimentalAutoimmune Encephalomyelitis.'; *Cells*, 2019

cells

MDPI

Article

High Speed Ventral Plane Videography as a Convenient Tool to Quantify Motor Deficits during Pre-Clinical Experimental Autoimmune Encephalomyelitis

Jiangshan Zhan [1,2], Vladislav Yakimov [1,2], Sebastian Rühling [1,2], Felix Fischbach [1,2], Elena Nikolova [1,2], Sarah Joost [1], Hannes Kaddatz [1], Theresa Greiner [1], Julia Frenz [1], Carsten Holzmann [1] and Markus Kipp [1,*]

1 Institute of Anatomy, Rostock University Medical Center, 18057 Rostock, Germany; jiangshan.zhan@campus.lmu.de (J.Z.); vladislavvd15@gmail.com (V.Y.); sebastian.ruehling@tum.de (S.R.); felix@famfischbach.de (F.F.); evladimirovanikolova@gmail.com (E.N.); sarah.joost@med.uni-rostock.de (S.J.); hannes.kaddatz@uni-rostock.de (H.K.); theresa.greiner@uni-rostock.de (T.G.); julia.frenz97@gmx.de (J.F.); carsten.holzmann@med.uni-rostock.de (C.H.)

2 Institute of Anatomy II, Faculty of Medicine, LMU Munich, 80336 Munich, Germany

* Correspondence: markus.kipp@med.uni-rostock.de; Tel.: +49-381-494-8401

Received: 23 August 2019; Accepted: 11 November 2019; Published: 14 November 2019

Abstract: Experimental autoimmune encephalomyelitis (EAE) is the most commonly used multiple sclerosis animal model. EAE mice typically develop motor deficits in a caudal-to-rostral pattern when inflammatory lesions have already developed. However, to monitor more subtle behavioral deficits during lesion development (i.e., pre-clinical phase), more sophisticated methods are needed. Here, we investigated whether high speed ventral plane videography can be applied to monitor early motor deficits during 'pre-clinical' EAE. For this purpose, EAE was induced in C57BL/6 mice and gait abnormalities were quantified using the DigiGait™ apparatus. Gait deficits were related to histopathological changes. 10 out of 10 control (100%), and 14 out of 18 (77.8%) pre-clinical EAE mice could be evaluated using DigiGait™. EAE severity was not influenced by DigiGait™-related mice handlings. Most gait parameters recorded from day 6 post-immunization until the end of the experiment were found to be stable in control mice. During the pre-clinical phase, when conventional EAE scorings failed to detect any functional impairment, EAE mice showed an increased *Swing Time*, increased *%Swing Stride*, decreased *%Stance Stride*, decreased *Stance/Swing*, and an increased *Absolute Paw Angle*. In summary, DigiGait™ is more sensitive than conventional scoring approaches to study motor deficits during the EAE pre-clinical phase.

Keywords: DigiGait™; experimental autoimmune encephalomyelitis; multiple sclerosis; gait analysis

1. Introduction

Multiple sclerosis (MS) is an autoimmune, inflammatory, demyelinating disease of the central nervous system (CNS). On the histopathological level, MS lesions are characterized by large inflammatory plaques of white matter demyelination. Such focal inflammatory lesions are associated with oligodendrocyte destruction, reactive gliosis and axonal degeneration. The composition of established inflammatory infiltrates varies between patients and/or lesion stages but commonly includes $CD8^+$ T-lymphocytes and macrophages. In addition to focal white matter lesions, gray matter demyelination and/or atrophy and diffuse white matter injury are frequently observed [1–3]. While the characteristics of established lesions are well investigated, how such lesions develop is less well

understood. On one hand, it is discussed that early during the development of inflammatory MS lesions, autoreactive T- and B-cells invade the brain parenchyma, get reactivated, and promote the development of inflammatory demyelination. Other authors suggest, however, that the recruitment of peripheral immune cells is a secondary phenomenon, triggered by a local, brain intrinsic degenerative event [4,5]. For example, one post-mortem study has shown that early MS lesions are characterized by oligodendrocyte degeneration and microglia activation in the absence of overt peripheral immune cells [6]. Whatever is true, imaging studies clearly demonstrate that subtle CNS pathologies can be observed before symptoms become evident [7–9].

For the development of new therapeutic options in MS, several models are available and can be roughly broken down into the categories of autoimmune and non-autoimmune animal models. Experimental autoimmune encephalomyelitis (EAE) is the most commonly used animal model to study autoimmune-mediated aspects of the disease. In this model, experimental animals (commonly rodents) are immunized with a CNS-related antigen administered in a strong adjuvant, usually complete Freund's adjuvant (CFA). Following immunization, antigens are phagocytized by local professional antigen-presenting cells, transported to local lymph nodes or the spleen, where they trigger the development of encephalitogenic T_{h1}- and T_{h17}-cell immune responses. This finally leads to inflammation within different CNS regions, mainly the spinal cord and the cerebellum [10]. On the behavioral level, this model is characterized by an ascending paralysis that begins in the tail and spreads to involve the hind limbs and, finally, fore limbs. Although different grading systems exist, the disease is usually rated on a scale ranging from grades 0–5. Grade 1 is assigned to mice that have lost tail tonicity, whereas grade 2 is assigned to mice that additionally show hind limb weakness. As the disease progresses, through grade 3 and 4, fore limb motor dysfunction additionally develops.

In MS, especially the early stages of lesion pathophysiology are poorly understood. Several studies were able to demonstrate that discrete histopathological changes occur within the brain parenchyma before acute inflammatory lesions become visible. Such changes include fibrinogen deposition [11], oligodendrocyte injury [6], focal microglia activation [12], and the downregulation of neuronal and oligodendrocyte marker gene expression [13]. In EAE, clinical symptoms are generally applied to mark the onset of disease, because this coincides with autoimmune effector $CD4^+$ T-cell infiltration into the CNS parenchyma [14,15]. However, recent reports show that structural and functional changes take place within CNS tissues before the development of clinically overt symptoms. Such observed changes include, among others, the activation of endothelial cells and astrocytes [16], reductions in myelin gene expression [13], or altered glutamate transmission [17]. Furthermore, in vivo imaging studies nicely demonstrate intraluminal crawling of encephalitogenic T-cells [14] and perivascular clustering of microglia [18] prior to the onset of clinical symptoms. In line with the observation of changes in brain homeostasis prior to the development of overt, inflammatory lesions our group recently demonstrated that toxic damage to the oligodendrocyte-myelin unit not just leads to glia activation but at the same time triggers the recruitment of peripheral immune cells into the CNS in the predisposed host [4,5,19]. Together, these data strongly implicate that subclinical alterations take place in the CNS tissue during the development of EAE that might predispose it to immunopathology.

In recent years, an extensive body of literature has demonstrated benefits of early treatment of MS with disease modifying drugs. Specifically, research has shown that early treatment in relation to disease onset is associated with significantly improved physical and mental outcomes, including lower relapse rates and lower expanded disability status scale (EDSS) scores, both in the short- and long-term [20–23]. A better understanding of the pre-clinical pathological processes would allow the development of early and probably effective therapeutic options. This requires mechanistic studies during the largely invisible pre-clinical disease stage. While novel and sensitive imaging modalities are currently available to visualize pathological changes during pre-symptomatic EAE, appropriate modalities to measure functional deficits are still missing.

In this work, we aimed to investigate whether high speed ventral plane videography is appropriate for the quantification of pre-clinical functional deficits in EAE.

2. Materials and Methods

2.1. Animals

For this study, 10-week-old C57BL/6 female mice (n = 40) were purchased from Janvier Labs, Le Genest-Saint-Isle, France. All experimental procedures were approved by the Review Board for the Care of Animal Subjects of the district government (Regierung Oberbayern; reference number 55.2-154-2532-73-15; Germany). The mice were maintained in a pathogen-free environment with a maximum of five animals per cage and with *ad libitum* food and water. Cages were changed once per week and microbiological monitoring was performed according to the Federation of European Laboratory Animal Science Associations recommendations. Mice were acclimated at the housing conditions for at least one week before EAE induction.

2.2. EAE Induction, Disease Scoring, and Experimental Groups

To induce the formation of encephalitogenic T-cells in peripheral lymphatic tissues, the mice were subcutaneously immunized with an emulsion of myelin oligodendrocyte glycoprotein ($MOG_{35–55}$) peptide dissolved in complete Freund's adjuvant followed by intraperitoneal injections of pertussis toxin (PTx) in PBS on the day of and the day after immunization (Hooke Laboratories, Inc., Lawrence, USA) as previously published [4]. Disease severity was scored as follows: 1, The entire tail drops over the observer's finger when the mouse is picked up by the base of the tail; 2, the legs are not spread apart but held close together when the mouse is picked up by the base of the tail, and mice exhibit a clearly apparent wobbly gait; 3, the tail is limp and mice show complete paralysis of hind legs (a score of 3.5 is given if the mouse is unable to raise itself when placed on its side); 4, the tail is limp and mice show complete hind leg paralysis and partial front leg paresis, and the mouse is minimally moving around the cage but appears alert and feeding; 5, the mouse is euthanized due to severe paralysis. The parameter "*disease onset*" was defined as the day post immunization when the first clinical deficit (see above) was observed. The parameter "*maximum disease score*" was defined as the highest clinical score, reached by a mouse at any time-point during the experiment. The parameter "*cumulative disease score*" was calculated by adding all clinical scores, registered during the experiment for a single mouse.

The following treatment groups were included: $Control^{DigiGait}$ mice: Non-immunized mice were subjected to gait analyses; EAE^{Only} mice: EAE was induced by MOG_{35-55} immunization + CFA/PTx, but mice were not subjected to gait analyses; $EAE^{DigiGait}$ mice: EAE was induced by MOG_{35-55} immunization + CFA/PTx, and mice were subjected to gait analyses starting at day 6 post immunization; $PTx^{DigiGait}$ mice: Mice were injected with CFA and PTx, and mice were subjected to gait analyses starting at day 6 post immunization.

2.3. High Speed Ventral Plane Videography and Evaluation

Gait parameters were assessed using the DigiGait™ imaging system along with the DigiGait™ 15.0 analysis software (Mouse Specifics, Inc.; Quincy, MA, USA) [24]. The DigiGait™ apparatus consists of a clear plastic treadmill with a high speed under-mounted digital camera (Basler Technologies Inc.) used for imaging paw prints. The treadmill belt was accelerated gradually to 15 cm/s. Images were collected at a rate of 140 frames/s. and stored as audio video interleaved (AVI) files for later blinded analyses. To improve the contrast for automated foot print analysis, the tails of the mice were colored with black dye. The treadmill belt was cleaned with 70% (*v/v*) ethanol between each animal testing. Animals were habituated to the machine one day prior to testing. Data obtained from the training day were not included in the final data evaluation. The image analysis software digitally encoded the individual paw area and position relative to the tread-belt. Each paw of the animal was treated as a unique signature so that later analyses of foot movements could be performed on separate limbs. Following this strategy, the DigiGait™ analysis software computes 39 gait parameters for the fore limbs and 43 for the hind limbs of each animal. The minimal duration of each video sequence required for subsequent foot-print analyses was 5 s. Runs where mice could not run at 15 cm/s for a minimum

of 5 s were excluded from subsequent analyses. This number of strides has been validated as being sufficient to analyze treadmill walking behavior in mice [25]. Figure 1 illustrates the principal setup of the performed gait analyses.

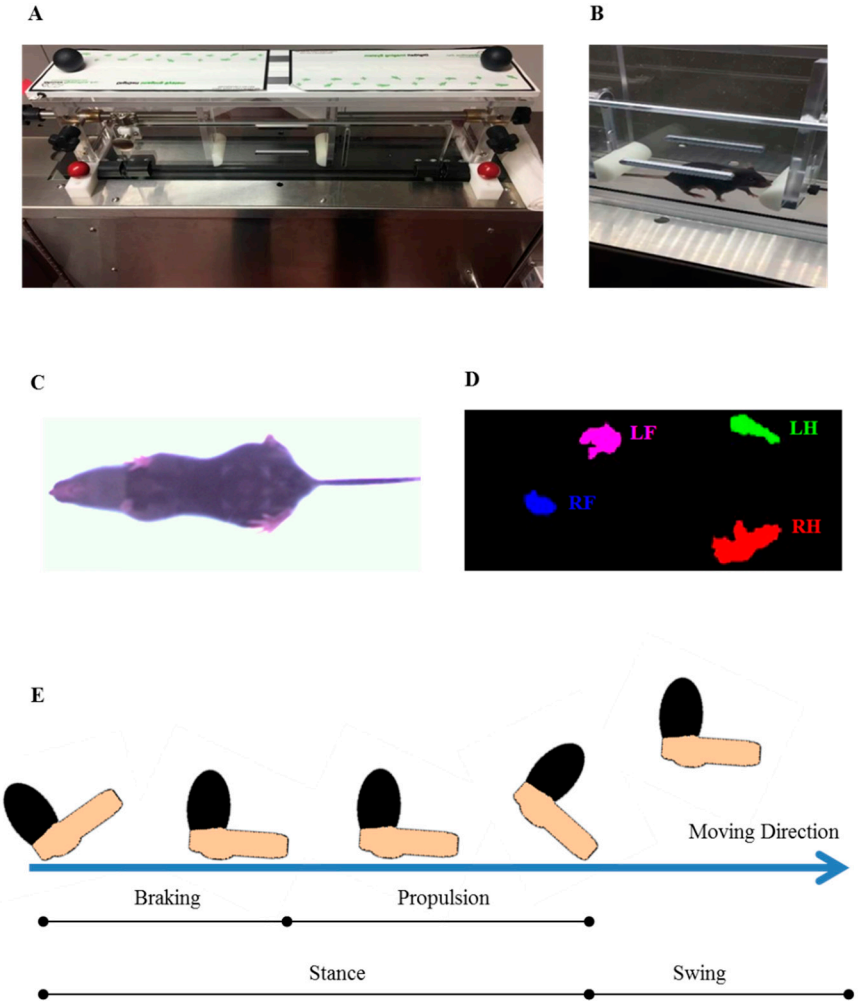

Figure 1. High speed ventral plane videography using the DigiGait™ setup. (**A**) Setup of the DigiGait™ imaging system. (**B**) DigiGait™ setup with a mouse in the running chamber during ventral plane videography recordings. (**C**) Representative image of a mouse during ventral plane videography recordings. (**D**) Representative image of the position of the single paws extracted from the ventral plane videography recordings by the provided analysis tool. (**E**) A graphical depiction of various aspects of a single mouse stride. Each stride can be subdivided into a stance and swing part. The stance part can be further subdivided into a braking and propulsion phase. LF: Left Fore; LH: Left Hind; RF: Right Fore; RH: Right Hind.

To analyze gait abnormalities during the pre-clinical disease stage, we first quantified fore limb and hind limb gait patterns in five control and 10 EAE-induced mice. This first group is referred to as Cohort#1. To verify results of this first experiment, hind limb gait patterns were analyzed in another cohort of five control and 10 EAE-induced mice, referred to as Cohort#2. Both cohorts were finally evaluated by a second evaluator blinded to the treatment groups (i.e., Evaluator 2).

2.4. Rotarod Analysis

To determine balance and motor coordination in control ($Control^{Rotarod}$; n = 10) and EAE ($EAE^{Rotarod}$; n = 8) mice, an accelerod system (TSE Systems, Bad Homburg, Germany) for small rodents was used (TSE Systems, Bad Homburg, Germany) as previously published by our group [26]. The apparatus consists of a base platform and a rotating rod (30 mm diameter, 114 mm width) with a non-skid surface. Each experimental mouse was subjected to three training sessions at a constant rotation speed of 5 rpm (rounds per min) for 2 min. These training sessions were conducted from day 3 to day 5 post immunization. Data obtained from the training sessions were not included in the data evaluation. During the testing session, an accelerating modus was used, which began at 4 rpm and accelerated to 40 rpm over a period of 300 s (i.e., 5 min). Two trials per test day were carried out, with a 60 min rest in between each trial. For each trial and each animal, latency, maximum speed, and walking distance before falling off were automatically recorded. The testing sessions were repeated from day 6 to day 13 post immunization. Only data obtained during pre-clinical disease stages were included for the final data evaluation.

2.5. Tissue Preparation and Histological Evaluation

For (immuno-) histological studies, mice were deeply anaesthetized with ketamine (100 $mg \cdot kg^{-1}$ i.p.) and xylazine (10 $mg \cdot kg^{-1}$ i.p.), and transcardially perfused with ice-cold phosphate-buffered saline (PBS) followed by a 3.7% formaldehyde solution (pH = 7.4). Tissues were postfixed overnight in a 3.7% formaldehyde solution, dissected, and embedded in paraffin. 5 µm thick sections were prepared using a slide microtome, dried at ambient temperature for at least 3 h, and subsequently dried overnight at 48 °C before starting the different staining procedures. For immunohistochemistry, sections were rehydrated and, if necessary, antigens were unmasked by heating in a Tris/EDTA (pH 9.0) buffer. After washing in PBS, sections were blocked in blocking solution (serum of the species in which the secondary antibody was produced) for 1 h. Then, sections were incubated overnight (4 °C) with primary antibodies diluted in blocking solution. The next day, slides were incubated in 0.3% hydrogen peroxide/PBS for 1 h and then incubated with biotinylated secondary antibodies for 1 h followed by peroxidase-coupled avidin-biotin complex (ABC kit; Vector Laboratories, Peterborough, UK). Sections were finally exposed to 3,3′-diaminobenzidine (DAKO, Santa Clara, CA, USA) as a peroxidase substrate. To visualize cell nuclei, sections were briefly stained with hematoxylin solution if appropriate. Negative control sections without primary antibodies were processed in parallel to ensure specificity of the staining. For microglia labelling anti-ionized calcium-binding adapter molecule 1 antibodies ([IBA1] 1:5000; Wako; #019-19741) were combined with anti-rabbit secondary antibodies (1:200; Vector; #BA-1000). For lymphocyte labelling, anti-CD3 antibodies ([CD3] 1:500; Abcam; ab11089) were combined with anti-rat secondary antibodies (1:200; Vector; #BA 9400). Luxol fast blue (LFB)/periodic acid-Schiff (PAS) stains were performed following standard protocols. Stained and processed sections were digitalized using a Leica DM6 B automated microscope (Leica Microsystems CMS GmbH, Wetzlar, Germany) equipped with a DMC6200 camera.

To analyse the extent of inflammatory demyelination in the spinal cord among $Control^{DigiGait}$, EAE^{Only}, and $EAE^{DigiGait}$ mice, the entire white matter was outlined in the digitalized images of LFB/PAS stained sections, and the areas of infiltrated white matter were measured using the open source program ImageJ 1.50. The measurements were conducted by one evaluator (J.Z.), blinded to the treatment groups. The areas of infiltrated white matter were then divided by the entire white matter area of the respective spinal cord section, and the result is given as relative infiltrated white matter area (in %). Representative images are shown in Figure 2C.

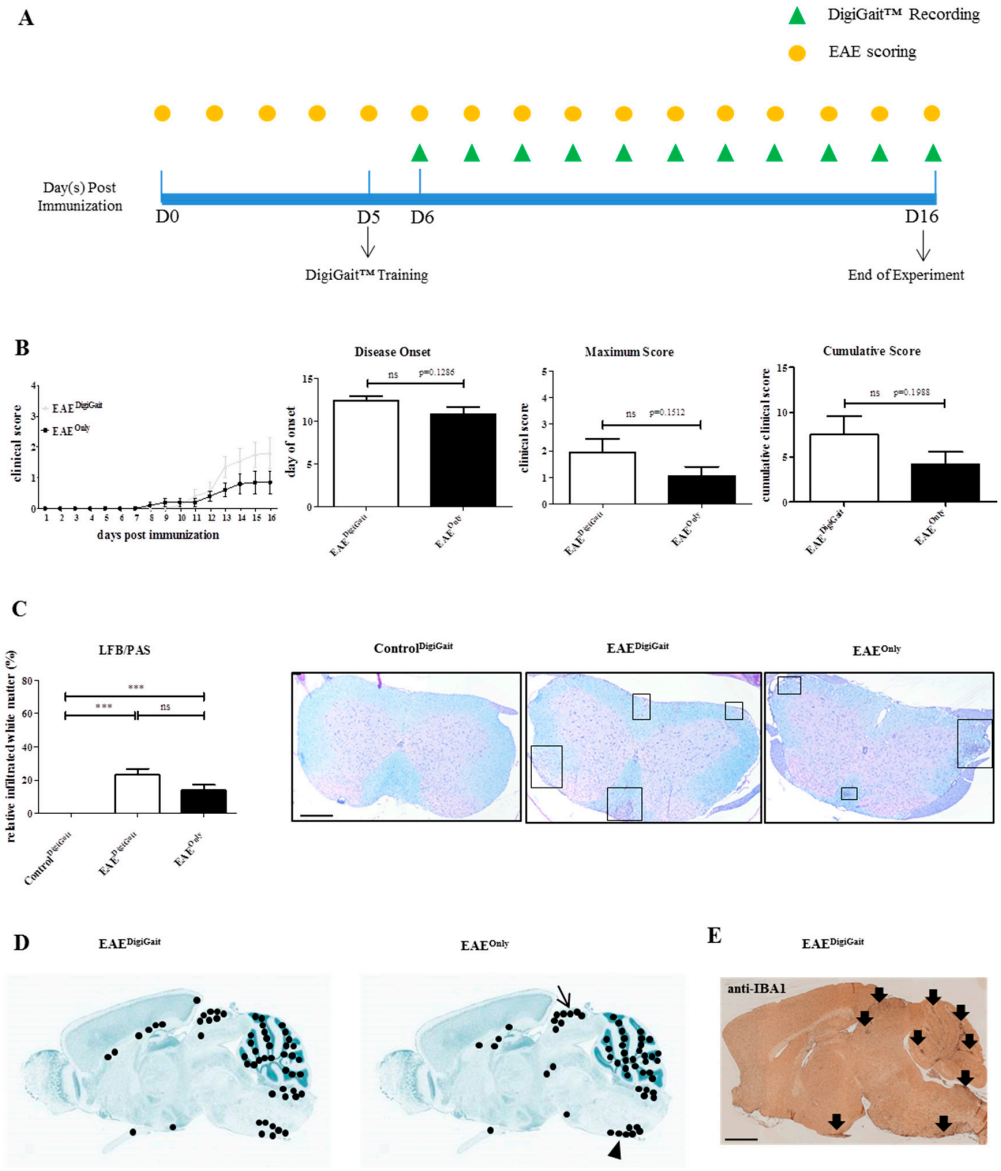

Figure 2. Manipulation during DigiGait™ recordings does not ameliorate EAE severity. (**A**) Schematic depiction of the experimental setup. D = days post immunization. The yellow circles indicate time points when EAE scoring was performed. The green triangles indicate time points when DigiGait^{TM}-measurements were performed. Note that at day 5 post immunization (D5), one DigiGait^{TM} training session was conducted. (**B**) Clinical course and evaluation of the disease parameters *disease onset*, *maximum score*, and *cumulative score* in EAE^{DigiGait} (n = 10) and EAE^{Only} (n = 10) mice. Note that 8 EAE^{DigiGait} and 6 EAE^{Only} mice, which developed clinical disease, were included to calculate the parameter *disease onset*. Data from all mice were included to calculate the parameters *maximum score* and *cumulative score*. Statistical comparison was done using an unpaired t-test. (**C**) Extent of inflammatory demyelination among Control^{DigiGait}, EAE^{DigiGait}, and EAE^{Only} mice evaluated in LFB/PAS stained sections (n = 72 sections). Black boxes highlight the inflammatory foci. Statistical comparison was done using a one-way analysis of variance with the obtained *p*-values corrected for multiple testing using the Dunnett's post hoc test. (**D**) Cumulative map of the spatial distribution of microgliosis in the CNS of EAE^{DigiGait} and EAE^{Only} mice, visualized by anti-IBA1 stains. Twenty sections from 10 individual animals were included per group. Each black dot shows the position of a focal IBA1^{+} lesion which was identified by both evaluators (J.Z. and H.K.). (**E**) Representative anti-IBA1 stain demonstrating IBA1^{+} lesions in an EAE^{DigiGait} mouse. Scale bar (**C**) = 300 µm; Scale bar (**E**) = 1 mm. EAE: Experimental Autoimmune Encephalomyelitis; LFB/PAS: Luxol fast blue/periodic acid-Schiff; CNS: Central Nervous System; IBA1: ionized calcium-binding adapter molecule 1. *** $p \leq 0.001$, ns = not significant.

To analyse the spatial distribution of microgliosis in mid-sagittal brain sections from EAE^{Only} and $EAE^{DigiGait}$ mice, sections were stained with anti-IBA1 antibodies and microgliosis sites were highlighted in a brain-template adopted from the Allen Mouse Brain Atlas [27]. Each black dot represents a single lesion per individual mouse (Figure 2D). These analyses were conducted by two evaluators blinded to the treatment groups (J.Z. and H.K.).

2.6. Statistical Analyses

All data are given as the arithmetic means ± SEM. Differences between groups were statistically tested using the software package GraphPad Prism 5 (GraphPad Software Inc., San Diego, CA, USA). The D'Agostino and Pearson test was applied to test for Gaussian distribution of the data. The definite statistical procedure applied for the different analyses is provided in the figure legends. p-value ≤ 0.05 were considered statistically significant. The following symbols are used to indicate the level of significance: * $p \leq 0.05$, ** $p \leq 0.01$, *** $p \leq 0.001$, ns = not significant.

3. Results

3.1. Manipulation of DigiGait™ Does Not Decrease EAE Severity

Previous studies have shown that stress might impact on EAE disease development [28]. Since the handling of the mice during DigiGait™ recordings might lead to additional stress, in a first step we systematically compared EAE severity in MOG_{35-55}-induced EAE mice which were subjected to DigiGait™ (n = 10; $EAE^{DigiGait}$) recordings or not (n = 10; EAE^{Only}). After immunization, the mice were evaluated daily for the occurrence and severity of clinical symptoms based on conventional evaluation protocols (see materials and methods section). The gait patterns were recorded daily starting six days post immunization until the mice reached an EAE score of ≥ 2 (equals hind limb paresis), or until day 16 post immunization (i.e., end of the experiment). A schematic depiction of the experimental setup is shown in Figure 2A.

As demonstrated in Figure 2B, both, EAE^{Only} and $EAE^{DigiGait}$ mice, exhibited motor behavioral deficits which are typical for MOG_{35-55}-induced EAE in C57BL/6 mice, starting with a limp tail and progressing towards hind limb paralysis. In the EAE^{Only} group, 6 out of 10 and in the $EAE^{DigiGait}$ group 8 out of 10 mice developed clinical deficits, respectively. Although the clinical symptoms in $EAE^{DigiGait}$ mice tended to be more severe compared to EAE^{Only} mice, no significant differences were observed for the parameters *time of disease onset* ($EAE^{DigiGait}$, 12.38 ± 0.5650 days versus EAE^{Only}, 10.83 ± 0.7923 days; $p = 0.1286$, just including mice which developed clinical disease), *maximum disease score* ($EAE^{DigiGait}$, 1.950 ± 0.4913 days versus EAE^{Only}, 1.050 ± 0.3452; $p = 0.1512$), and *cumulative disease score* ($EAE^{DigiGait}$, 7.500 ± 2.053 days versus EAE^{Only}, 4.200 ± 1.379 days; $p = 0.1988$) (Figure 2B). Next, we analyzed the extent of inflammatory infiltrates in $EAE^{DigiGait}$ and EAE^{Only} mice to correlate functional deficits with histopathological changes. For this purpose, three spinal cord sections (cervical to lumbar level) were collected in a random fashion for each mouse and the inflamed white matter area in relation to the entire spinal cord white matter area was quantified in LFB/PAS stained sections.

As demonstrated in Figure 2C, no significant difference was observed in the extent of inflammatory demyelination between $EAE^{DigiGait}$ and EAE^{Only} mice ($EAE^{DigiGait}$, 23.28% ± 3.549% versus EAE^{Only}, 13.99% ± 3.205%). Spearman's correlation analysis, including data from both experimental groups, revealed a highly significant correlation between spinal cord white matter inflammation and the extent of clinical deficits (r = 0.7221; r^2 = 0,52; 95% confidence interval = 0.59 to 0.82; p-value (two-tailed) ≤ 0.0001). Furthermore, we analyzed the spatial distribution of microgliosis in the brains of $EAE^{DigiGait}$ and EAE^{Only} mice. As demonstrated in Figure 2D,E, focal microgliosis was found in diverse brain regions such as the cerebellum, dorsal midbrain (arrow in Figure 2D), ventral medulla oblongata around the inferior olivary complex (arrowhead in Figure 2D), and to some extent around the third ventricle. In summary, both cohorts demonstrate widespread CNS inflammation with no quantitative differences in the extent of CNS lesion formation.

Beyond, we analyzed the densities of $CD3^+$ lymphocytes in the spinal cord dorsal column and the white matter of the cerebellum. As demonstrated in Figure 3, lymphocyte densities were low in $Control^{DigiGait}$, but high in $EAE^{DigiGait}$ and EAE^{Only} mice (Spinal cord dorsal column, $Control^{DigiGait}$ 10.87 ± 4.180 cells/mm^2, versus $EAE^{DigiGait}$, 134.5 ± 19.20 cells/mm^2 versus EAE^{Only}, 129.9 ± 21.00 cells/mm^2: Cerebellum white matter, $Control^{DigiGait}$ 1.367 ± 0.7197 cells/mm^2, versus $EAE^{DigiGait}$, 292.9 ± 56.61 cells/mm^2 versus EAE^{Only}, 225.9 ± 65.31 cells/mm^2). Of note, no significant differences were observed between $EAE^{DigiGait}$ and EAE^{Only} mice.

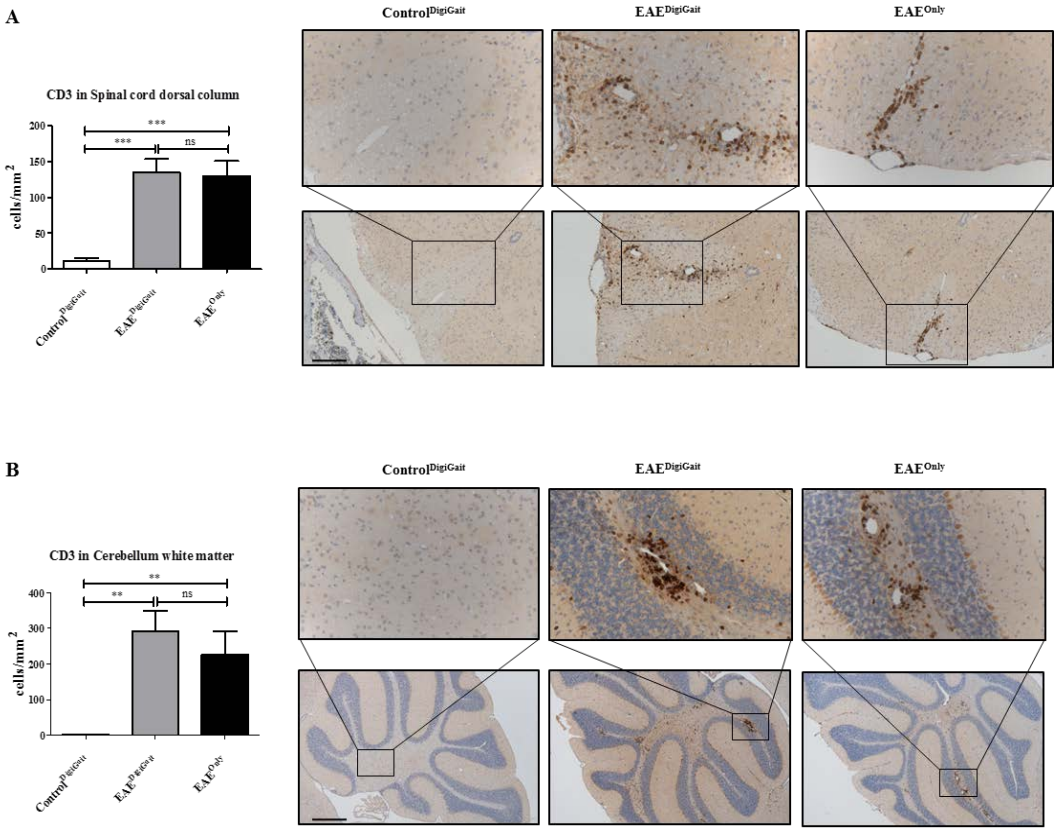

Figure 3. Lymphocyte densities in the spinal cord and cerebellar white matter. (**A**) Numbers of $CD3^+$ lymphocytes in the dorsal column of the spinal cord (n = 75 sections) in $Control^{DigiGait}$, $EAE^{DigiGait}$, and EAE^{Only} mice. (**B**) Numbers of $CD3^+$ lymphocytes in the white matter of the cerebellum (n = 25 sections) in $Control^{DigiGait}$, $EAE^{DigiGait}$, and EAE^{Only} mice. Statistical comparison was done using a one-way analysis of variance with the obtained p-values corrected for multiple testing using the Dunnett's post hoc test. Note that no significant difference has been observed between $EAE^{DigiGait}$ and EAE^{Only} mice. Scale bar (**A**) = 150 µm; Scale bar (**B**) = 300 µm. ** $p \leq 0.01$, *** $p \leq 0.001$, ns = not significant.

3.2. Most Gait Parameters Are Stable in Control Mice

Next, we investigated the reliability of the gait analysis procedure. To this end, gait analyses were conducted in control mice (n = 10, two separate experiments), and the coefficient of variation (CV), which is defined as the ratio of the standard deviation to the mean (SD/mean), was calculated. The term "high variability parameters" was defined as gait parameters which had a CV of higher than 30% [29]. As described in the materials and method section of this manuscript, the DigiGait™ computes 39 gait parameters for the fore limbs and 43 for the hind limbs, respectively. As listed in Table 1, 10 out of 39 (25.6%) fore limb, and 13 out of 43 (30.2%) hind limb parameters showed a high variability in control mice. This, on the one hand, indicates that not all of the gait parameters evaluated by the DigiGait^{Tm} software are adequate for the detection of a pathological gate, at least in mice at

the applied experimental settings. However, a significant proportion of gait parameters (i.e., 30) can reliably be measured using the DigiGait™ apparatus.

Table 1. High variability parameters in control mice. List of gait parameters which were found to be highly variable in control animals. High variability parameters were defined as gait metrics which show a coefficient of variation (CV) of more than 30% in control mice [29]. For more information, see the materials and methods section of this manuscript.

	Parameters with High Variability
Fore Limbs (10 out of 39 parameters) 25.6%	Absolute Paw Angle (Sum) Stride Width Variability Step Angle Variability Stance Width CV Step Angle CV Paw Area Variability at Peak Stance (Average) Overlap Distance (Average) Paw Placement Positioning (Average) Paw Angle (Left fore limb) Paw Angle (Right fore limb)
Hind Limbs (13 out of 43 parameters) 30.2%	Stride Length Variability (Average) Stride Width Variability Stride Length CV (Average) Stance Width CV Step Angle CV Paw Area Variability at Peak Stance (Average) Paw Placement Positioning (Average) Tau-Propulsion (Average) Overlap Distance (Average) Ataxia Coefficient (Average) Paw Angle (Left hind limb) Paw Angle (Right hind limb) Paw Drag (Average)

3.3. Mice Show Gait Abnormalities in Hind Limbs during the EAE Pre-Clinical Phase

In a next step, we asked whether gait abnormalities can be quantified during the pre-clinical EAE phase. For this purpose, we systematically compared changes of the gait parameters in control (referred to as Control^{DigiGait}; n = 10) and MOG_{35-55}-immunized (referred to as EAE^{DigiGait}; n = 18) mice. As it has been shown that the running speed can influence gait parameters in rodents [30], we used a constant speed of 15 cm/s.

As demonstrated in Figure 4, 18 out of 20 immunized animals developed clinical EAE. EAE was severe in some animals (#2 and #9 with a score of five) but moderate in others (for example, #6 with a transient score of one). MOG_{35-55} immunization severely influenced the success rate of gait analysis recordings. Just 3 out of 18 animals could be daily evaluated until the day of disease onset (i.e., mice #7, #17, and #18), whereas 6 out of 18 animals could be daily evaluated until the day BEFORE disease onset (#3, #11, and #12, additionally to the mice #7, #17, #18). Four animals could not be evaluated at any time point after MOG_{35-55} immunization (#4, #5, #9, and #14).

Mouse Number	Treatment	d6	d7	d8	d9	d10	d11	d12	d13	d14	d15	d16
#1		0	0	0	0	0 ×	0	0 ×	0 ×	0 ×	1	1.5
#2		0 ×	0 ×	0 ×	0	0	2	2.5	2.5	2.5	4	5
#3		0 ×	0 ×	0 ×	0 ×	0	1	1	3	3	3	3
#4		0	0	0	0	1	1	2	2	2.5	2.5	2.5
#5		0	0	0	0	0	0	0	2	3	2.5	2.5
#6		0 ×	0 ×	0 ×	0 ×	0 ×	0	0	1	1	1	0
#7		0 ×	0 ×	0 ×	0 ×	0 ×	0 ×	0 ×	1	1	1	1
#8		0 ×	0 ×	0 ×	0 ×	0 ×	0	0	2	2.5	2.5	2.5
#9	**EAE**$^{\text{DigiGait}}$	0	0	2.5	3	3	2.5	4	5	5	5	
#10		0 ×	0	0	0	0	0	2.5	2.5	2.5	3	
#11		0 ×	0 ×	0 ×	0 ×	0 ×	0	2	2.5	3	3	
#12		0 ×	0 ×	0	2.5	3	2.5	2.5	2.5	2.5	1.5	
#13		0 ×	0	0	0	0.5	1.5	2.5	2.5	2.5	2.5	
#14		0	0	0	2.5	3	3	2.5	2.5	2.5	2.5	
#15		0 ×	0 ×	0 ×	0	0	0	0	0	2.5	2.5	
#16		0 ×	0 ×	0	0	1	1.5	1.5	2.5	2.5	2.5	
#17		0 ×	0 ×	0 ×	0 ×	0 ×	0 ×	0 ×	1.5	2	2.5	
#18		0 ×	0 ×	0 ×	0 ×	0 ×	0 ×	1.5	3	3	3	
#19		0 ×	0 ×	0 ×	0 ×	0 ×	0 ×	0 ×	0 ×	0 ×	0 ×	
#20		0 ×	0 ×	0 ×	0 ×	0 ×	0 ×	0 ×	0 ×	0 ×	0 ×	
#21		0	0	0	0	0	0	0	0	0	0 ×	
#22		0 ×	0 ×	0 ×	0 ×	0 ×	0 ×	0 ×	0 ×	0 ×	0 ×	
#23	**PTx**$^{\text{DigiGait}}$	0 ×	0 ×	0	0	0	0	0 ×	0 ×	0 ×	0 ×	
#24		0 ×	0 ×	0 ×	0 ×	0 ×	0 ×	0 ×	0	0	0 ×	
#25		0 ×	0 ×	0 ×	0 ×	0 ×	0 ×	0 ×	0 ×	0 ×	0 ×	
#26		0 ×	0 ×	0 ×	0 ×	0 ×	0 ×	0 ×	0 ×	0 ×	0 ×	
#27		0	0	0	0	0	0	0	0	0	0 ×	
#28		0	0	0	0	0.5	0	0	0	0	0	
#29		0 ×	0 ×	0 ×	0 ×	0 ×	0 ×	0 ×	0 ×	0 ×	0 ×	0 ×
#30		0 ×	0 ×	0 ×	0 ×	0 ×	0 ×	0 ×	0 ×	0 ×	0 ×	0 ×
#31		0 ×	0 ×	0 ×	0 ×	0 ×	0 ×	0 ×	0 ×	0 ×	0 ×	0 ×
#32		0 ×	0 ×	0 ×	0 ×	0 ×	0 ×	0 ×	0 ×	0 ×	0 ×	0 ×
#33	**Control**$^{\text{DigiGait}}$	0 ×	0 ×	0 ×	0 ×	0 ×	0 ×	0 ×	0 ×	0 ×	0 ×	0 ×
#34		0 ×	0 ×	0 ×	0 ×	0 ×	0 ×	0 ×	0 ×	0 ×	0 ×	
#35		0 ×	0 ×	0 ×	0 ×	0 ×	0 ×	0 ×	0 ×	0 ×	0 ×	
#36		0 ×	0 ×	0 ×	0 ×	0 ×	0 ×	0 ×	0 ×	0 ×	0 ×	
#37		0 ×	0 ×	0 ×	0 ×	0 ×	0 ×	0 ×	0 ×	0 ×	0 ×	
#38		0 ×	0 ×	0 ×	0 ×	0 ×	0 ×	0 ×	0 ×	0 ×	0 ×	

Pattern	Illustration	**Control**$^{\text{DigiGait}}$ **(n=10)**	**PTx**$^{\text{DigiGait}}$ **(n=10)**	**EAE**$^{\text{DigiGait}}$ **(n=18)**
×	Time points included for data analyses	105	66	55
	Completed DigiGait assessments at 15cm/s	105	69	62
	Failed DigiGait assessments at 15cm/s	0	31	59
	Completed Ratio (%)	100	69	51

Figure 4. Summary of gait analyses experiments. Days with successfully conducted DigiGait^{TM} recordings are highlighted in green, whereas days on which no DigiGait^{TM} recordings could be performed are highlighted in red. Numbers in the boxes indicate the level of motor behavior deficits evaluated by classical EAE scoring. Yellow crosses indicate time points included for data analyses.

As outlined in the materials and method section, gait analyses were initiated at day 6 post immunization and continued daily until the animals (i) either reached a score of ≥ 2, (ii) were not able to run on the treadmill at the given velocity (i.e., 15 cm/s), or (iii) until day 16 post immunization. Following this strategy and pooling the data from two independent experiments, 105 gait analyses were performed in control animals for the different time points with a success rate of 100%. 121 gait analyses were performed in MOG_{35-55}-immunized mice with a success rate of 51% (equals 62 completed gait analyses). These results already suggest that although conventional EAE scoring protocols fail to detect overt changes (i.e., paralysis of the tail), the motor performance is already impaired at this 'pre-clinical' disease stage.

Blinded evaluations of the high speed ventral plane videography recordings were performed in two separate cohorts of animals, referred to as cohort#1 (five control animals and eight EAE animals) and cohort#2 (five control animals and 10 EAE animals). Only data obtained during the pre-clinical disease stages were included. In a first step, fore limb and hind limb gait parameters were evaluated in the cohort#1 mice and statistically compared. As one would expect in a model of ascending paralysis [31,32], more gait parameters were altered in the hind limbs (n = 15) compared to the fore limbs (n = 9) during the pre-clinical disease stage. As demonstrated in Table 2, 15 distinct hind limb gait metrics were found to be increased or decreased in $EAE^{DigiGait}$ compared to $Control^{DigiGait}$ mice during the pre-clinical disease stage. To verify these findings, the gait parameters which were found to be significantly different in the cohort#1 mice were re-evaluated in our cohort#2 mice. For the fore limb parameters, none of the 9 parameters were verified in the cohort#2 mice. In contrast, from the 15 gait parameters found to be different in the hind limbs of cohort#1 mice, 7 were verified in the second cohort. These were the gait metrics *Swing Time (Average), %Swing Stride (Average), %Stance Stride (Average), Stance/Swing (Average), Paw Angle-Left Hind, Paw Angle-Right Hind,* and *Absolute Paw Angle (Sum)*.

As demonstrated in the materials and methods section, the gait signals provided by the software requires some manual, thus subjective, adjustments. To verify that our results are indeed valid, another independent evaluator performed the analyses of cohort#1 and cohort#2 video sequences in a blinded manner. As demonstrated in Table 2, all 7 gait parameters were approved by the second evaluator.

Next, we were interested whether gait abnormalities during pre-clinical EAE can as well be detected using the Rotarod test which is widely used to evaluate the motor coordination of rodents [33,34]. To this end, performance in the rotarod test was compared between 10 control ($Control^{Rotarod}$) mice and 8 pre-clinical EAE mice ($EAE^{Rotarod}$). As demonstrated in Figure 5, $EAE^{Rotarod}$ mice showed comparable values in the Rotarod parameters *latency* ($EAE^{Rotarod}$, 212.7 ± 8.617 s versus $Control^{Rotarod}$, 195.7 ± 7.033 s; $p = 0.1106$), *maximum speed* ($EAE^{Rotarod}$, 29.39 ± 1.036 rpm. versus $Control^{Rotarod}$, 27.41 ± 0.8427 rpm.; $p = 0.1367$), and *walking distance* ($EAE^{Rotarod}$, 5.935 ± 0.3887 m versus $Control^{Rotarod}$, 5.239 ± 0.3128 m; $p = 0.1169$) when compared with $Control^{Rotarod}$ mice.

Table 2. Gait abnormalities during pre-clinical EAE. Summary of gait parameters found to be altered during pre-clinical EAE. Two independent experiments were performed, referred to as Cohort#1 and Cohort#2. Gait parameters were evaluated by two independent observers, referred to as Evaluator 1 and Evaluator 2. Arrows indicate whether gait metrics were increased or decreased during the pre-clinical EAE phase. During pre-clinical EAE, 9 fore limb gait parameters were found to be different in Cohort#1 mice, but not in Cohort#2 mice (indicated by ns = not significant). In contrast, 15 hind limb gait parameters were found to be different in Cohort#1 mice, and 7 of these were found to be as well different in the Cohort#2 mice (indicated by the respective *p*-value). All of these 7 parameters were verified by the Evaluator 2 (last column). The D'Agostino and Pearson test was applied to test for normal distribution of the data. *p*-values for the effect of EAE treatment were calculated using t-test or Mann-Whitney test according to data distribution. All videos were analyzed by two evaluators (J.Z. and V.Y.) blinded for the experimental groups. * $p \leq 0.05$, ** $p \leq 0.01$, *** $p \leq 0.001$, ns = not significant, ↑: increased; ↓: decreased.

	Parameter Number	Parameters	Evaluator 1 Cohort#1 (Change, Significance, *p*-Value)	Evaluator 1 Cohort#2 (Change, Significance, *p*-Value)	Evaluator 2 Cohort#1 and Cohort#2 (Change, Significance, *p*-Value)
Fore Limbs	#1	Paw Angle Variability (Average)	↓, *, 0.0483	↓, ns, 0.7092	
	#2	Stance Width	↑, *, 0.0241	↑, ns, 0.8720	
	#3	Stride Length Variability (Average)	↓, ***, 0.0008	↑, ns, 0.5670	
	#4	Stride Width Variability	↓, ***, 0.0001	↓, ns, 0.5056	
	#5	Stride Length CV (Average)	↓, *, 0.0101	↓, ns, 0.3456	
	#6	Stance Width CV	↓, ***, < 0.0001	↓, ns, 0.6412	
	#7	Paw Area at Peak Stance (Average)	↑, *, 0.0486	↑, ns, 0.1747	
	#8	Paw Area Variability at Peak Stance (Average)	↓, **, 0.0097	↓, ns, 0.2705	
	#9	Ataxia Coefficient (Average)	↓, **, 0.0082	↓, ns, 0.2659	
Hind Limbs	#1	Swing Time (Average)	↑, *, 0.0239	↑, ***, < 0.0001	↑, ***,< 0.0001
	#2	%Swing Stride (Average)	↑, *, 0.0278	↑, ***, < 0.0001	↑, ***,< 0.0001
	#3	%Stance Stride (Average)	↓, *, 0.0278	↓, ***, < 0.0001	↓, ***,< 0.0001
	#4	Stance/Swing (Average)	↓, *, 0.0274	↓, ***, < 0.0001	↓, ***, 0.0002
	#5	Paw Angle-Left Hind	↑, ***, < 0.0001	↑, ***, 0.0006	↑, ***, < 0.0001
	#6	Paw Angle-Right Hind	↑, ***, < 0.0001	↑, **, 0.005	↑, ***, < 0.0001
	#7	Absolute Paw Angle (Sum)	↑, ***, < 0.0001	↑, ***, 0.0002	↑, ***, < 0.0001
	#8	Stride Width Variability	↓, **, 0.0071	↓, ns, 0.5056	
	#9	Stance Width CV	↓, **, 0.0073	↓, ns, 0.6412	
	#10	Paw Area at Peak Stance (Average)	↓, ***, 0.0005	↑, ns, 0.4922	
	#11	Paw Area Variability at Peak Stance (Average)	↓, *, 0.0403	↑, ns, 0.2317	
	#12	MAX dA/dT (Average)	↓, **, 0.0010	↑, ns, 0.2313	
	#13	Tau-Propulsion (Average)	↓, *, 0.0198	↓, ns, 0.2448	
	#14	Midline Distance (Sum)	↑, ***, < 0.0001	↓, *, 0.0442	
	#15	Paw Drag (Average)	↑, ***, 0.0001	↑, ns, 0.7821	

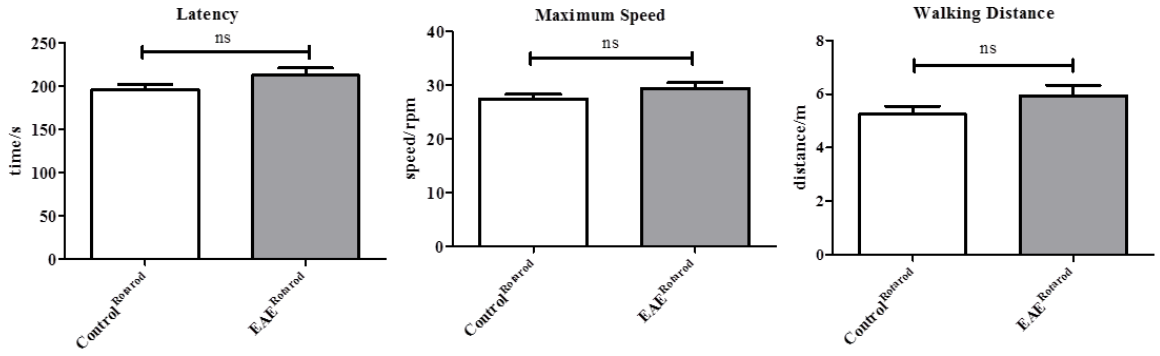

Figure 5. Gross locomotor ability in the Rotarod assay during pre-clinical EAE. Gait parameters were assessed in Control^{Rotarod} (n = 10) and EAE^{Rotarod} (n = 8) mice. Both cohorts were tested for their ability to run on a rotating cylinder that accelerated its speed with time (4–40 rpm in 300 s). Latencies to fall from the accelerating cylinder (i.e., *latency*), the *maximum speed* mice were able to run, and the *walking distance* on the rotating cylinder are presented as mean ± SEM. The D'Agostino and Pearson test was applied to test for normal distribution of the data. *p*-values for the effect of EAE treatment were calculated using t-test or Mann-Whitney test according to data distribution. ns = not significant.

3.4. Gait Abrnoramilties in Mice Sub-Immunized with CFA and PTx

Our analyses so far suggest that during pre-clinical EAE, motor abnormalities can be quantified using high speed ventral plane videography. Severe inflammation is characteristic for the clinical but not pre-clinical EAE phase. We, thus, assumed that diffuse, innate immune driven pathological processes account at least in part for the observed gait abnormalities. To mimic diffuse innate immune activation, we systematically investigated gait abnormalities in control mice and mice injected with CFA and PTx without the $MOG_{35–55}$ peptide (referred to as sub-immunization). Various studies have shown that the administration of CFA and PTx without the $MOG_{35–55}$ peptide induces diffuse innate immune activation in the CNS of mice [35–38]. In particular, we analyzed whether or not the identified gait metrics found to be altered during pre-clinical EAE are as well different in sub-immunized mice. We excluded the two parameters "paw-angle of the left hind limb" and "paw angle of the right hind limb" because both were found to be highly variable in control animals (see Table 1). Among the remaining five abnormal gait parameters during the EAE pre-clinical phase, we found that *Swing Time (Average)* was significantly different between sub-immunized (PTx^{DigiGait}) and fully immunized (EAE^{DigiGait}) mice. In contrast, such a difference was not observed for the other 4 gait parameters suggesting that most of the observed gait differences are due to diffuse innate immune system activation (Figure 6).

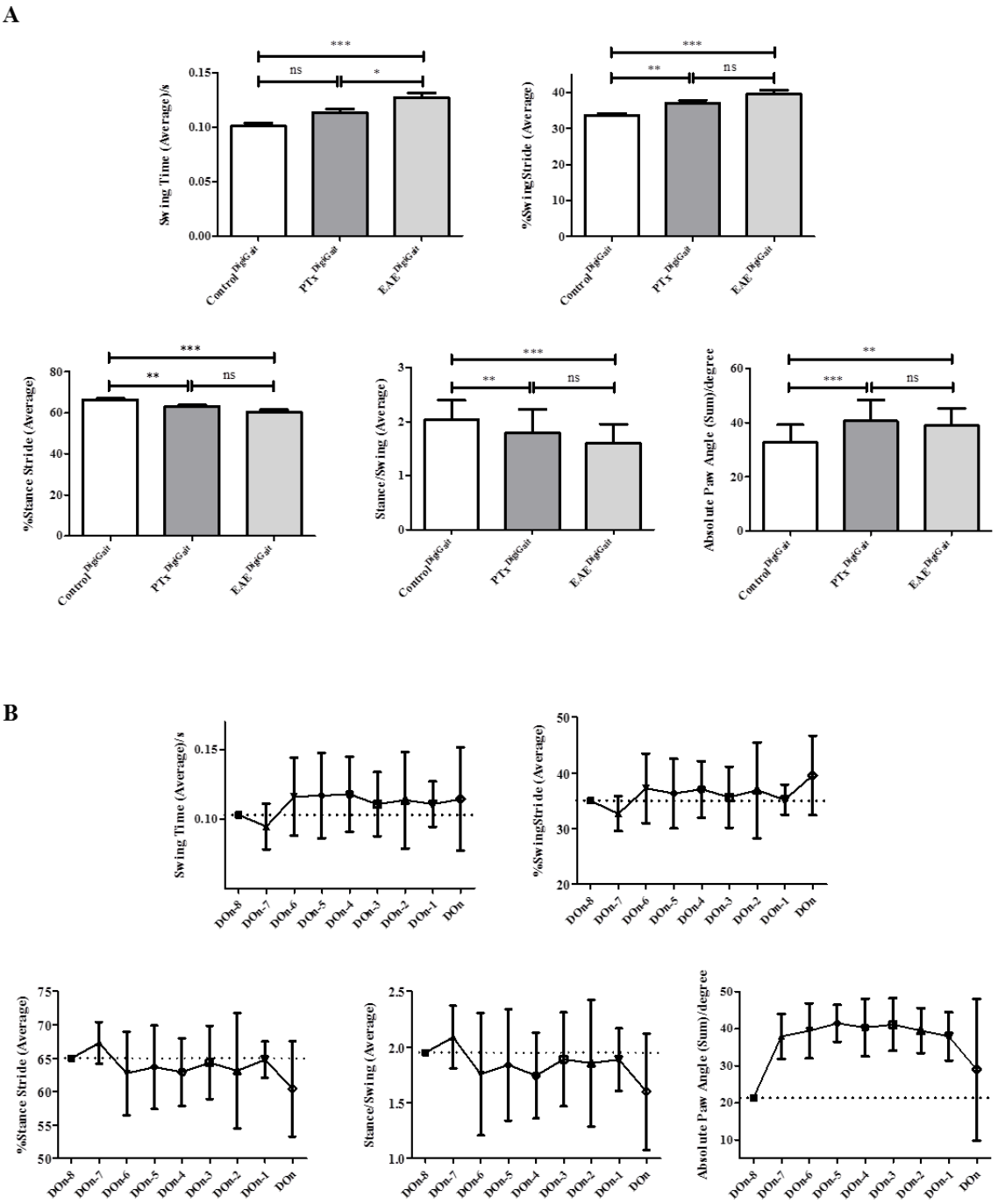

Figure 6. Effect of EAE sub-immunization on gait parameters. (**A**) Differences of the gait metrics in Control^{DigiGait}, PTx^{DigiGait}, and EAE^{DigiGait} mice. D'Agostino and Pearson test was applied to test for normal distribution of the data. *p*-values generated using one-way ANOVA with Bonferroni post-test for multiple comparisons of individual pairs of treatment. Note that the gait parameter *Swing Time* is significantly different between sub-immunized (PTx^{DigiGait}) and fully immunized (EAE^{DigiGait}) mice. (**B**) Gait parameters over time in fully immunized (EAE^{DigiGait}) mice. Don = day of onset, Don-1 = 1 day before onset, etc. * $p \leq 0.05$, ** $p \leq 0.01$, *** $p \leq 0.001$, ns = not significant.

4. Discussion

The most commonly used behavioral evaluation method in EAE is based on the severity of motor deficits, which is mainly driven by spinal cord pathology. In most studies, each mouse is graded daily and given a score ranging from 0 to 5 [39–41]. Parameters include limp tail or hind limb weakness when

EAE is mild and partial or complete hind limb and fore limb paralysis in severe EAE cases. Of note, this evaluation approach is neither very sensitive nor objective. Therefore, in order to detect minor motor deficits, more accurate and reliable EAE evaluation methods are urgently needed. In this study, we used the high speed ventral plane videography system DigiGait™ to characterize and quantify a set of different gait metrics during pre-clinical EAE. We were able to show (1) that manipulation during DigiGait™ measurements does not decrease EAE severity; (2) that many gait parameters are stable in control mice; (3) that the mice show hind limb gait abnormalities during pre-clinical EAE and, (4) that most of the observed gait abnormalities during pre-clinical EAE are probably driven by an interplay of innate and adaptive immune activation.

The expanded disability status scale (EDSS), which is the most commonly used measure of disability for MS, ranges from 0 to 10 in 0.5 unit increments that represent higher levels of disability and is based on the individual, subjective examination by a neurologist. EDSS steps 1.0 to 4.5 refer to people with MS who are able to walk without any aid and are based on measures of impairment in eight functional systems, among motor disturbances. Other measures of motor disability in MS include the timed 25 foot walk, which assesses ambulatory function, or walking [42], and the 9 hole peg test, which measures upper body function and manual dexterity [43]. Indeed, gait impairment is a hallmark of MS which significantly impacts on the quality of life of the individual [44]. Comparable to the human disease, MS models are characterized by gait abnormalities [4,5]. As already stated above, there is no standard EAE scoring system which research groups would use to measure EAE severity [45]. The use of different EAE scoring systems prohibits direct comparison of clinical EAE data published from different laboratories. Furthermore, the applied scoring systems rely on subjective rather than objective evaluations. An objective and quantitative approach would, therefore, be of great interest for pre-clinical trials using the EAE model.

Different automatic or semi-automatic systems have been applied to quantify gait abnormalities in different EAE models, among the CatWalk^{TM} XT system. The CatWalk^{TM} System consists of a glass walkway that is illuminated by fluorescent light. When the paw is in contact with the upper surface of the walkway, the print light is reflected, which is detected by an appropriate high speed color camera and detection software. Of note, the animal walks across the glass plate voluntarily which is different to the system applied in the current study. This method has been performed in the EAE model using different species such as Lewis rats [46], Brown Norway rats [47], or C57BL/6 mice [48]. In our study, we observed that MOG_{35-55} immunization severely influenced the success rate of gait analysis recordings. Just 3 out of 18 animals could be daily evaluated until the day of disease onset, whereas 6 out of 18 animals could be daily evaluated until the day BEFORE disease onset. This result clearly demonstrates that running at a velocity of 15 cm/s displays a motor-performance challenge which cannot be met by most of the mice during pre-clinical EAE. Bernardes et al. noted in their study that with disease progression, some animals were not able to cross the CatWalk^{TM} walkway after established EAE [48]. During pre-clinical EAE all animals were able to perform the gait analysis task which is in contrast to our results. However, one major difference between the CatWalk^{TM} and the DigiGait™ system is that in the former, mice gait is voluntary whereas in the latter, mice are forced to walk by the motorized treadmill. It is, thus, possible that forced movements are more demanding compared to voluntary ones. Nevertheless, in line with our results the authors found a decrease in *Swing Speed* which equals the observed increase of the *Swing Time* in our study.

In this study, we applied high speed ventral plane videography to analyze gait abnormalities during pre-clinical EAE. High speed ventral plane videography has been shown to be a useful approach to quantify subtle locomotors abnormalities in mouse models of neurodegenerative movement disorders, such as Amyotrophic lateral sclerosis (ALS), Huntington or cerebellar ataxia [49]. For example, altered hind limb movement, accompanied by some changes in coordination and stability characterized the gait abnormalities in SOD1 G93A transgenic mice, which is a model of ALS [49], whereas *Stride Length* and *Stride Frequencies* were found to be altered in a model of Parkinson's disease [50]. Gait analyses were as well found to be useful in non-neurological disorders such as in collagen-induced arthritis [51] or in a

model of muscular dystrophy [52]. We followed an exploratory approach (analyzing 39 different gait parameters for the fore limbs and 43 for the hind limbs) to study gait abnormalities during pre-clinical EAE. As many gait parameters change with running speed [30], the analyses were performed in this study at a constant speed of 15 cm/s (see Materials and Methods Section). Based on this extensive dataset, we identified a small set of relevant gait parameters which were different in pre-clinical EAE compared to control mice. These parameters, namely *Swing Time*, *%Swing Stride*, *%Stance Stride*, *Stance/Swing*, *Paw Angle-Left Hind*, *Paw Angle-Right Hind*, and *Absolute Paw Angle*, may be used in following studies to assess potential therapeutic effects during pre-clinical EAE. The definition of these parameters, as provided by the manufacturer of the DigiGait™ system are as follow: *Swing Time*—Time duration of the swing phase (no paw contact with belt) given in seconds; *%Swing Stride*—Percent of the total stride duration that the paw is in the air (swing phase); *%Stance Stride*—% of the total stride duration that the paw is in any contact with the belt; *Stance/Swing*—Ratio of stance phase time to swing phase time; *Paw Angle-Left or Right Hind*—The angle that the paw makes with the long axis of the direction of motion of the animal; *Absolute Paw Angle*—Absolute value of the paw angle. Having these definitions in mind it is not surprising to find the parameters *Swing Time* and *%Swing Stride* to be increased while the gait parameter *%Stance Stride* is decreased. However, this particular finding nicely demonstrates the reliability of the used evaluation method. Worth to note that, in line with our findings of an increased *Paw Angle*, these gait deficits were found to be associated with ataxia, spinal cord injury, and demyelinating disease [53].

One major finding of the present study is that gait abnormalities during the pre-clinical EAE phase can be quantified. Such alterations have as well been observed by others. For example, Leva et al. found in SJL/J mice immunized with proteolipid protein ($PLP_{139–151}$) that the CatWalk™ gait parameter *Maximum Contact Area* decreased three days post immunization, at a time point were conventional disease scoring protocols failed to detect any disease activity [54]. Similar observations were reported by Silva et al. [46], as well using the CatWalk™ System in Lewis rats [46]. Of note, the gait parameter *Maximum Contact Area*, which is called *Paw Area at Peak Stance* in the DigiGait™ environment, was found to be decreased for the hind limbs in Cohort#1 animals, however, we were not able to reproduce this finding in Cohort#2 mice. In the later study, Silva et al. observed, besides a reduced *Maximum Contact Area* of the paw, reductions of the so-called *Regularity Index (RI)* during pre-clinical EAE. *RI* represents a gait metrics for motor coordination. For fully coordinated locomotion, each paw is placed exactly once every four steps. There are a total of six possible step sequence patterns that can be used by a rodent while walking. These patterns can be categorized into three groups: Alternate (Aa: [RF: Right front-RH: Right hind-LF: Left front-LH: Left hind]: RF-RH-LF-LH, Ab: LF-RH-RF-LH); cruciate (Ca: RF-LF-RH-LH, Cb: LF-RF-LH-RH); and rotary (Ra: RF-LF-LH-RH; Rb: LF-RF-RH-LH). The Ab pattern is the most commonly observed. The larger the number of missteps intersperse between regular step patterns, the lower is the *RI* [55]. The same gait parameter is not evaluated by the DigiGait™ software. However, it includes the metrics *Gait Symmetry* which computes the ratio of forelimb stepping frequency to hind limb stepping frequency. It has been shown that the parameter *Gait Symmetry* declines with age and treadmill training counteracted the decline of *Gait Symmetry* [56]. Of note, no differences with respect to the parameter *Gait Symmetry* were found during the pre-clinical EAE phase in our current study.

In a recent study, Kappos et al. analyzed the validity and reliability of the CatWalk™ system as a static and dynamic gait analysis tool for the assessment of functional nerve recovery in small animal models [55]. They found that among different gait parameters, *Swing Duration* was the most reliable and valid gait parameter. In our study, *Swing Time*, which is essentially the same as *Swing Duration*, was found to be increased in both experimental cohorts and the difference was verified by two independent observers. Of note, it has been shown that *Swing Duration* increases with pain [57–59], and pain, which is a frequent and disabling symptom in MS patients, as well characterizes EAE animals to some extent [60]. Of note, a recent study showed that pain can as well be observed during the

pre-clinical EAE phase [61]. It is, thus, possible that pain is the underlying mechanism of the observed increased *Swing Time* in our EAE mice. Further studies are needed to verify or reject this hypothesis.

Another important finding of our study is that sub-immunization of the mice with CFA and PTx is sufficient to induce moderate gait abnormalities in the experimental mice. In animal models of EAE, the disease is induced actively by immunization with myelin protein peptides, such as MOG or PLP peptide dissolved in CFA, or passively by activated neuroantigen-specific T-cells transfer. The incidence and severity of the disease induced by neuroantigens in CFA is promoted by PTx co-injection [62]. Although PTx has been widely used in EAE induction of rodents, the exact role of PTx in initiating EAE remains controversial. Historically, it was thought that this microbial product facilitates EAE by breaking down the blood-brain barrier and thereby helps pathogenic T-cells to migrate into the CNS. Further studies have shown that PTx increases the expression of endothelial adhesion molecules which triggers leukocyte infiltration into the brain [37]. PTx could also facilitate EAE induction through modulating the interaction between the innate and adaptive immune system in the response to self-antigens [36]. Moreover, PTx has other biological functions that could contribute to its activity in EAE such as inducing maturation of dendritic cells [38], enhancing T effector cells' cytokine production as well as reducing T regulatory cells' activity [63,64]. Murugesan et al. showed that CFA/PTx alone could cause widespread gene alterations that could prime the choroid plexus to unlock the CNS to T-cell infiltration during neuroinflammatory disease [65]. In this study, we used sub-immunization to uncover whether autoreactive T-cells are required to induce the observed gait abnormalities. As demonstrated in Figure 6A, the extent of gait alterations was found to be more severe in fully immunized mice compared to sub-immunized animals. These results suggest that both, innate and adaptive immunity, act in concert to induce gait abnormalities during pre-clinical EAE.

One major advantage of semi-automated gait analyses in EAE and other neurodegenerative diseases is that such metrics can be directly compared with measurement obtained during clinical trials. In a recent trial, Liparoti et al. investigated gait patterns in minimally disabled RRMS patients applying a three dimensional-gait analysis approach. They could show that, compared to healthy controls, RRMS show an increase of *Swing Time* [66]. Beyond, Novotna et al. were able to show that MS patients with no apparent disability (EDSS 0-1.5) showed abnormalities in the GAITRite gait analysis instrument [67], suggesting that particular aspects of human gait abnormalities can be investigated in mice.

Another important advantage of the DigiGait™ analysis system is the semi-automated analysis approach. Although some manual adjustments have to be performed during the video analysis procedure, false negative or positive results due to experimenter bias are less likely to occur. Nevertheless, blinding during the video analysis procedure is mandatory.

5. Conclusions

In summary, DigiGait™ is more sensitive than conventional scoring approaches to study motor deficits during the EAE pre-clinical phase. To evaluate such abnormalities we suggest to either quantify the numbers of successful runs on the treadmill and/or to quantify the gait parameters *Swing Time*, *% Swing Stride*, *%Stance Stride*, *Stance/Swing* ratio, or *Absolute Paw Angle*. Early detection of gait abnormalities in the EAE model may accelerate the development of therapies for MS.

Author Contributions: M.K. and J.Z. designed the concept of the present study and supervised it. J.Z., V.Y., and S.R. performed high speed ventral plane videography in mice. J.Z., V.Y., and F.F. performed data analyses. J.Z., E.N., S.J., T.G., J.F., and H.K. performed (immuno-) histochemistry and related analyses. J.Z., T.G., J.F., and C.H. performed Rotarod test and related analyses. J.Z. drafted the manuscript. M.K. critically revised the article for important intellectual content. All authors read and approved the final version of the manuscript.

Funding: This research was funded by the Deutsche Forschungsgemeinschaft (KI 1469/8-1; #398138584; M.K.).

Acknowledgments: J.Z. is financially supported by the China Scholarship Council for living stipend (CSC201706010354). We thank Frauke Winzer, Astrid Baltruschat, Sarah Wübbel, Beate Aschauer, Barbara Mosler, and Sabine Tost for their excellent and valuable technical assistance.

Conflicts of Interest: The authors declare no conflict of interest.

References

1. Elkjaer, M.L.; Frisch, T.; Reynolds, R.; Kacprowski, T.; Burton, M.; Kruse, T.A.; Thomassen, M.; Baumbach, J.; Illes, Z. Unique RNA signature of different lesion types in the brain white matter in progressive multiple sclerosis. *Acta Neuropathol. Commun.* **2019**, *7*, 58. [CrossRef]
2. Van der Poel, M.; Ulas, T.; Mizee, M.R.; Hsiao, C.C.; Miedema, S.S.M.; Adelia; Schuurman, K.G.; Helder, B.; Tas, S.W.; Schultze, J.L.; et al. Transcriptional profiling of human microglia reveals grey-white matter heterogeneity and multiple sclerosis-associated changes. *Nat. Commun.* **2019**, *10*, 1139. [CrossRef]
3. Vercellino, M.; Trebini, C.; Capello, E.; Mancardi, G.L.; Giordana, M.T.; Cavalla, P. Inflammatory responses in Multiple Sclerosis normal-appearing white matter and in non-immune mediated neurological conditions with wallerian axonal degeneration: A comparative study. *J. Neuroimmunol.* **2017**, *312*, 49–58. [CrossRef]
4. Ruther, B.J.; Scheld, M.; Dreymueller, D.; Clarner, T.; Kress, E.; Brandenburg, L.O.; Swartenbroekx, T.; Hoornaert, C.; Ponsaerts, P.; Fallier-Becker, P.; et al. Combination of cuprizone and experimental autoimmune encephalomyelitis to study inflammatory brain lesion formation and progression. *Glia* **2017**, *65*, 1900–1913. [CrossRef]
5. Scheld, M.; Ruther, B.J.; Grosse-Veldmann, R.; Ohl, K.; Tenbrock, K.; Dreymuller, D.; Fallier-Becker, P.; Zendedel, A.; Beyer, C.; Clarner, T.; et al. Neurodegeneration Triggers Peripheral Immune Cell Recruitment into the Forebrain. *J. Neurosci.* **2016**, *36*, 1410–1415. [CrossRef]
6. Barnett, M.H.; Prineas, J.W. Relapsing and remitting multiple sclerosis: Pathology of the newly forming lesion. *Ann. Neurol.* **2004**, *55*, 458–468. [CrossRef]
7. McDonnell, G.V.; Cabrera-Gomez, J.; Calne, D.B.; Li, D.K.; Oger, J. Clinical presentation of primary progressive multiple sclerosis 10 years after the incidental finding of typical magnetic resonance imaging brain lesions: The subclinical stage of primary progressive multiple sclerosis may last 10 years. *Mult. Scler.* **2003**, *9*, 204–209. [CrossRef]
8. De Groot, C.J.; Bergers, E.; Kamphorst, W.; Ravid, R.; Polman, C.H.; Barkhof, F.; van der Valk, P. Post-mortem MRI-guided sampling of multiple sclerosis brain lesions: Increased yield of active demyelinating and (p)reactive lesions. *Brain* **2001**, *124*, 1635–1645. [CrossRef]
9. Laule, C.; Vavasour, I.M.; Whittall, K.P.; Oger, J.; Paty, D.W.; Li, D.K.; MacKay, A.L.; Arnold, D.L. Evolution of focal and diffuse magnetisation transfer abnormalities in multiple sclerosis. *J. Neurol.* **2003**, *250*, 924–931. [CrossRef]
10. Kipp, M.; Nyamoya, S.; Hochstrasser, T.; Amor, S. Multiple sclerosis animal models: A clinical and histopathological perspective. *Brain Pathol.* **2017**, *27*, 123–137. [CrossRef]
11. Lee, N.J.; Ha, S.K.; Sati, P.; Absinta, M.; Luciano, N.J.; Lefeuvre, J.A.; Schindler, M.K.; Leibovitch, E.C.; Ryu, J.K.; Petersen, M.A.; et al. Spatiotemporal distribution of fibrinogen in marmoset and human inflammatory demyelination. *Brain* **2018**, *141*, 1637–1649. [CrossRef]
12. Van der Valk, P.; Amor, S. Preactive lesions in multiple sclerosis. *Curr. Opin. Neurol.* **2009**, *22*, 207–213. [CrossRef]
13. Evangelidou, M.; Karamita, M.; Vamvakas, S.S.; Szymkowski, D.E.; Probert, L. Altered expression of oligodendrocyte and neuronal marker genes predicts the clinical onset of autoimmune encephalomyelitis and indicates the effectiveness of multiple sclerosis-directed therapeutics. *J. Immunol.* **2014**, *192*, 4122–4133. [CrossRef]
14. Bartholomaus, I.; Kawakami, N.; Odoardi, F.; Schlager, C.; Miljkovic, D.; Ellwart, J.W.; Klinkert, W.E.; Flugel-Koch, C.; Issekutz, T.B.; Wekerle, H.; et al. Effector T cell interactions with meningeal vascular structures in nascent autoimmune CNS lesions. *Nature* **2009**, *462*, 94–98. [CrossRef]
15. Flugel, A.; Berkowicz, T.; Ritter, T.; Labeur, M.; Jenne, D.E.; Li, Z.; Ellwart, J.W.; Willem, M.; Lassmann, H.; Wekerle, H. Migratory activity and functional changes of green fluorescent effector cells before and during experimental autoimmune encephalomyelitis. *Immunity* **2001**, *14*, 547–560. [CrossRef]
16. Alvarez, J.I.; Saint-Laurent, O.; Godschalk, A.; Terouz, S.; Briels, C.; Larouche, S.; Bourbonniere, L.; Larochelle, C.; Prat, A. Focal disturbances in the blood-brain barrier are associated with formation of neuroinflammatory lesions. *Neurobiol. Dis.* **2015**, *74*, 14–24. [CrossRef]

17. Centonze, D.; Muzio, L.; Rossi, S.; Cavasinni, F.; De Chiara, V.; Bergami, A.; Musella, A.; D'Amelio, M.; Cavallucci, V.; Martorana, A.; et al. Inflammation triggers synaptic alteration and degeneration in experimental autoimmune encephalomyelitis. *J. Neurosci.* **2009**, *29*, 3442–3452. [CrossRef]
18. Baranzini, S.E.; Bernard, C.C.; Oksenberg, J.R. Modular transcriptional activity characterizes the initiation and progression of autoimmune encephalomyelitis. *J. Immunol.* **2005**, *174*, 7412–7422. [CrossRef]
19. Chrzanowski, U.; Bhattarai, S.; Scheld, M.; Clarner, T.; Fallier-Becker, P.; Beyer, C.; Rohr, S.O.; Schmitz, C.; Hochstrasser, T.; Schweiger, F.; et al. Oligodendrocyte degeneration and concomitant microglia activation directs peripheral immune cells into the forebrain. *Neurochem. Int.* **2019**, *126*, 139–153. [CrossRef]
20. Masuda, H.; Mori, M.; Hirano, S.; Kojima, K.; Uzawa, A.; Uchida, T.; Ohtani, R.; Kuwabara, S. Relapse numbers and earlier intervention by disease modifying drugs are related with progression of less brain atrophy in patients with multiple sclerosis. *J. Neurol. Sci.* **2019**, *403*, 78–84. [CrossRef]
21. Landfeldt, E.; Castelo-Branco, A.; Svedbom, A.; Lofroth, E.; Kavaliunas, A.; Hillert, J. The long-term impact of early treatment of multiple sclerosis on the risk of disability pension. *J. Neurol.* **2018**, *265*, 701–707. [CrossRef]
22. PRISMS Study Group; The University of British Columbia MS/MRI Analysis Group. PRISMS-4: Long-term efficacy of interferon-beta-1a in relapsing MS. *Neurology* **2001**, *56*, 1628–1636. [CrossRef]
23. Kavaliunas, A.; Manouchehrinia, A.; Stawiarz, L.; Ramanujam, R.; Agholme, J.; Hedstrom, A.K.; Beiki, O.; Glaser, A.; Hillert, J. Importance of early treatment initiation in the clinical course of multiple sclerosis. *Mult. Scler.* **2017**, *23*, 1233–1240. [CrossRef]
24. Hampton, T.G.; Stasko, M.R.; Kale, A.; Amende, I.; Costa, A.C. Gait dynamics in trisomic mice: Quantitative neurological traits of Down syndrome. *Physiol. Behav.* **2004**, *82*, 381–389. [CrossRef]
25. Kale, A.; Amende, I.; Meyer, G.P.; Crabbe, J.C.; Hampton, T.G. Ethanol's effects on gait dynamics in mice investigated by ventral plane videography. *Alcohol. Clin. Exp. Res.* **2004**, *28*, 1839–1848. [CrossRef]
26. Schlegel, V.; Thieme, M.; Holzmann, C.; Witt, M.; Grittner, U.; Rolfs, A.; Wree, A. Pharmacologic Treatment Assigned for Niemann Pick Type C1 Disease Partly Changes Behavioral Traits in Wild-Type Mice. *Int. J. Mol. Sci.* **2016**, *17*, 1866. [CrossRef]
27. Lein, E.S.; Hawrylycz, M.J.; Ao, N.; Ayres, M.; Bensinger, A.; Bernard, A.; Boe, A.F.; Boguski, M.S.; Brockway, K.S.; Byrnes, E.J.; et al. Genome-wide atlas of gene expression in the adult mouse brain. *Nature* **2007**, *445*, 168–176. [CrossRef]
28. Perez-Nievas, B.G.; Garcia-Bueno, B.; Madrigal, J.L.; Leza, J.C. Chronic immobilisation stress ameliorates clinical score and neuroinflammation in a MOG-induced EAE in Dark Agouti rats: Mechanisms implicated. *J. Neuroinflamm.* **2010**, *7*, 60. [CrossRef]
29. Brown, C.E. *Applied Multivariate Statistics in Geohydrology and Related Sciences*; Springer Science & Business Media: Berlin, Germany, 2012.
30. Hruska, R.E.; Kennedy, S.; Silbergeld, E.K. Quantitative aspects of normal locomotion in rats. *Life Sci.* **1979**, *25*, 171–179. [CrossRef]
31. Butter, C.; Baker, D.; O'Neill, J.K.; Turk, J.L. Mononuclear cell trafficking and plasma protein extravasation into the CNS during chronic relapsing experimental allergic encephalomyelitis in Biozzi AB/H mice. *J. Neurol. Sci.* **1991**, *104*, 9–12. [CrossRef]
32. Oldendorf, W.H.; Towner, H.F. Blood-brain barrier and DNA changes during the evolution of experimental allergic encephalomyelitis. *J. Neuropathol. Exp. Neurol.* **1974**, *33*, 616–631. [CrossRef] [PubMed]
33. Nampoothiri, S.S.; Potluri, T.; Subramanian, H.; Krishnamurthy, R.G. Rodent Gymnastics: Neurobehavioral Assays in Ischemic Stroke. *Mol. Neurobiol.* **2017**, *54*, 6750–6761. [CrossRef] [PubMed]
34. Curzon, P.; Zhang, M.; Radek, R.J.; Fox, G.B. The Behavioral Assessment of Sensorimotor Processes in the Mouse: Acoustic Startle, Sensory Gating, Locomotor Activity, Rotarod, and Beam Walking. In *Methods of Behavior Analysis in Neuroscience*, 2nd ed.; Buccafusco, J.J., Ed.; CRC Press/Taylor & Francis: Boca Raton, FL, USA, 2009.
35. Munoz, J.J.; Bernard, C.C.; Mackay, I.R. Elicitation of experimental allergic encephalomyelitis (EAE) in mice with the aid of pertussigen. *Cell Immunol.* **1984**, *83*, 92–100. [CrossRef]
36. Hofstetter, H.H.; Shive, C.L.; Forsthuber, T.G. Pertussis toxin modulates the immune response to neuroantigens injected in incomplete Freund's adjuvant: Induction of Th1 cells and experimental autoimmune encephalomyelitis in the presence of high frequencies of Th2 cells. *J. Immunol.* **2002**, *169*, 117–125. [CrossRef]

37. Kerfoot, S.M.; Long, E.M.; Hickey, M.J.; Andonegui, G.; Lapointe, B.M.; Zanardo, R.C.; Bonder, C.; James, W.G.; Robbins, S.M.; Kubes, P. TLR4 contributes to disease-inducing mechanisms resulting in central nervous system autoimmune disease. *J. Immunol.* **2004**, *173*, 7070–7077. [CrossRef]
38. Shive, C.L.; Hofstetter, H.; Arredondo, L.; Shaw, C.; Forsthuber, T.G. The enhanced antigen-specific production of cytokines induced by pertussis toxin is due to clonal expansion of T cells and not to altered effector functions of long-term memory cells. *Eur. J. Immunol.* **2000**, *30*, 2422–2431. [CrossRef]
39. Bittner, S.; Afzali, A.M.; Wiendl, H.; Meuth, S.G. Myelin oligodendrocyte glycoprotein (MOG35-55) induced experimental autoimmune encephalomyelitis (EAE) in C57BL/6 mice. *J. Vis. Exp.* **2014**. [CrossRef]
40. Miller, S.D.; Karpus, W.J. Experimental autoimmune encephalomyelitis in the mouse. *Curr. Protoc. Immunol.* **2007**. [CrossRef]
41. Stromnes, I.M.; Goverman, J.M. Active induction of experimental allergic encephalomyelitis. *Nat. Protoc.* **2006**, *1*, 1810–1819. [CrossRef]
42. Motl, R.W.; Cohen, J.A.; Benedict, R.; Phillips, G.; LaRocca, N.; Hudson, L.D.; Rudick, R.; Multiple Sclerosis Outcome Assessments, C. Validity of the timed 25-foot walk as an ambulatory performance outcome measure for multiple sclerosis. *Mult. Scler.* **2017**, *23*, 704–710. [CrossRef]
43. Feys, P.; Lamers, I.; Francis, G.; Benedict, R.; Phillips, G.; LaRocca, N.; Hudson, L.D.; Rudick, R.; Multiple Sclerosis Outcome Assessments, C. The Nine-Hole Peg Test as a manual dexterity performance measure for multiple sclerosis. *Mult. Scler.* **2017**, *23*, 711–720. [CrossRef] [PubMed]
44. Heesen, C.; Bohm, J.; Reich, C.; Kasper, J.; Goebel, M.; Gold, S.M. Patient perception of bodily functions in multiple sclerosis: Gait and visual function are the most valuable. *Mult. Scler.* **2008**, *14*, 988–991. [CrossRef] [PubMed]
45. Fiander, M.D.; Stifani, N.; Nichols, M.; Akay, T.; Robertson, G.S. Kinematic gait parameters are highly sensitive measures of motor deficits and spinal cord injury in mice subjected to experimental autoimmune encephalomyelitis. *Behav. Brain Res.* **2017**, *317*, 95–108. [CrossRef] [PubMed]
46. Silva, G.A.; Pradella, F.; Moraes, A.; Farias, A.; dos Santos, L.M.; de Oliveira, A.L. Impact of pregabalin treatment on synaptic plasticity and glial reactivity during the course of experimental autoimmune encephalomyelitis. *Brain Behav.* **2014**, *4*, 925–935. [CrossRef]
47. Herold, S.; Kumar, P.; Jung, K.; Graf, I.; Menkhoff, H.; Schulz, X.; Bahr, M.; Hein, K. CatWalk gait analysis in a rat model of multiple sclerosis. *BMC Neurosci.* **2016**, *17*, 78. [CrossRef]
48. Bernardes, D.; Oliveira, A.L.R. Comprehensive catwalk gait analysis in a chronic model of multiple sclerosis subjected to treadmill exercise training. *BMC Neurol.* **2017**, *17*, 160. [CrossRef]
49. Preisig, D.F.; Kulic, L.; Kruger, M.; Wirth, F.; McAfoose, J.; Spani, C.; Gantenbein, P.; Derungs, R.; Nitsch, R.M.; Welt, T. High-speed video gait analysis reveals early and characteristic locomotor phenotypes in mouse models of neurodegenerative movement disorders. *Behav. Brain Res.* **2016**, *311*, 340–353. [CrossRef]
50. Amende, I.; Kale, A.; McCue, S.; Glazier, S.; Morgan, J.P.; Hampton, T.G. Gait dynamics in mouse models of Parkinson's disease and Huntington's disease. *J. Neuroeng. Rehabil.* **2005**, *2*, 20. [CrossRef]
51. Vincelette, J.; Xu, Y.; Zhang, L.N.; Schaefer, C.J.; Vergona, R.; Sullivan, M.E.; Hampton, T.G.; Wang, Y.X. Gait analysis in a murine model of collagen-induced arthritis. *Arthritis Res. Ther.* **2007**, *9*, R123. [CrossRef]
52. Hampton, T.G.; Kale, A.; Amende, I.; Tang, W.; McCue, S.; Bhagavan, H.N.; VanDongen, C.G. Gait disturbances in dystrophic hamsters. *J. Biomed. Biotechnol.* **2011**, *2011*, 235354. [CrossRef]
53. Powell, E.; Anch, A.M.; Dyche, J.; Bloom, C.; Richtert, R.R. The splay angle: A new measure for assessing neuromuscular dysfunction in rats. *Physiol. Behav.* **1999**, *67*, 819–821. [CrossRef]
54. Leva, G.; Klein, C.; Benyounes, J.; Halle, F.; Bihel, F.; Collongues, N.; De Seze, J.; Mensah-Nyagan, A.G.; Patte-Mensah, C. The translocator protein ligand XBD173 improves clinical symptoms and neuropathological markers in the SJL/J mouse model of multiple sclerosis. *Biochim. Et Biophys. Acta Mol. Basis Dis.* **2017**, *1863*, 3016–3027. [CrossRef] [PubMed]
55. Kappos, E.A.; Sieber, P.K.; Engels, P.E.; Mariolo, A.V.; D'Arpa, S.; Schaefer, D.J.; Kalbermatten, D.F. Validity and reliability of the CatWalk system as a static and dynamic gait analysis tool for the assessment of functional nerve recovery in small animal models. *Brain Behav.* **2017**, *7*, e00723. [CrossRef] [PubMed]
56. Dorner, H.; Otte, P.; Platt, D. Training influence on age-dependent changes in the gait of rats. *Gerontology* **1996**, *42*, 7–13. [CrossRef] [PubMed]
57. Vrinten, D.H.; Hamers, F.F. 'CatWalk' automated quantitative gait analysis as a novel method to assess mechanical allodynia in the rat; a comparison with von Frey testing. *Pain* **2003**, *102*, 203–209. [CrossRef]

58. Duffy, S.S.; Keating, B.A.; Perera, C.J.; Lees, J.G.; Tonkin, R.S.; Makker, P.G.S.; Carrive, P.; Butovsky, O.; Moalem-Taylor, G. Regulatory T Cells and Their Derived Cytokine, Interleukin-35, Reduce Pain in Experimental Autoimmune Encephalomyelitis. *J. Neurosci.* **2019**, *39*, 2326–2346. [CrossRef]
59. Catuneanu, A.; Paylor, J.W.; Winship, I.; Colbourne, F.; Kerr, B.J. Sex differences in central nervous system plasticity and pain in experimental autoimmune encephalomyelitis. *Pain* **2019**, *160*, 1037–1049. [CrossRef]
60. Harada, Y.; Zhang, J.; Imari, K.; Yamasaki, R.; Ni, J.; Wu, Z.; Yamamoto, K.; Kira, J.I.; Nakanishi, H.; Hayashi, Y. Cathepsin E in neutrophils contributes to the generation of neuropathic pain in experimental autoimmune encephalomyelitis. *Pain* **2019**. [CrossRef]
61. Serizawa, K.; Tomizawa-Shinohara, H.; Yasuno, H.; Yogo, K.; Matsumoto, Y. Anti-IL-6 Receptor Antibody Inhibits Spontaneous Pain at the Pre-onset of Experimental Autoimmune Encephalomyelitis in Mice. *Front. Neurol.* **2019**, *10*, 341. [CrossRef]
62. Lee, J.M.; Olitsky, P.K. Simple method for enhancing development of acute disseminated encephalomyelitis in mice. *Proc. Soc. Exp. Biol. Med.* **1955**, *89*, 263–266. [CrossRef]
63. Chen, X.; Winkler-Pickett, R.T.; Carbonetti, N.H.; Ortaldo, J.R.; Oppenheim, J.J.; Howard, O.M. Pertussis toxin as an adjuvant suppresses the number and function of CD4+CD25+ T regulatory cells. *Eur. J. Immunol.* **2006**, *36*, 671–680. [CrossRef] [PubMed]
64. Wakatsuki, A.; Borrow, P.; Rigley, K.; Beverley, P.C. Cell-surface bound pertussis toxin induces polyclonal T cell responses with high levels of interferon-gamma in the absence of interleukin-12. *Eur. J. Immunol.* **2003**, *33*, 1859–1868. [CrossRef] [PubMed]
65. Murugesan, N.; Paul, D.; Lemire, Y.; Shrestha, B.; Ge, S.; Pachter, J.S. Active induction of experimental autoimmune encephalomyelitis by MOG35-55 peptide immunization is associated with differential responses in separate compartments of the choroid plexus. *Fluids Barriers CNS* **2012**, *9*, 15. [CrossRef] [PubMed]
66. Liparoti, M.; Della Corte, M.; Rucco, R.; Sorrentino, P.; Sparaco, M.; Capuano, R.; Minino, R.; Lavorgna, L.; Agosti, V.; Sorrentino, G.; et al. Gait abnormalities in minimally disabled people with Multiple Sclerosis: A 3D-motion analysis study. *Mult. Scler. Relat. Disord.* **2019**, *29*, 100–107. [CrossRef] [PubMed]
67. Novotna, K.; Sobisek, L.; Horakova, D.; Havrdova, E.; Lizrova Preiningerova, J. Quantification of Gait Abnormalities in Healthy-Looking Multiple Sclerosis Patients (with Expanded Disability Status Scale 0-1.5). *Eur. Neurol.* **2016**, *76*, 99–104. [CrossRef] [PubMed]

Zusammenfassung

Im Rahmen meiner Promotion beschäftigte ich mich mit zwei Aspekten der MS: Zum einen, welche Rolle eine Stressreaktion des ERs bei Oligodendrozyten Degeneration und Demyelinisierung spielt. Zum anderen, ob in der Frühphase einer inflammatorischen Demyelinisierung Gangdefizite nachgewiesen werden können.

Für die Beantwortung der ersten Fragestellung wurde das toxische Demyelinisierungsmodell Cuprizone verwendet. Es zeigte sich, dass bereits früh im Verlauf des Tiermodells die Expression verschiedener ER-Stress assoziierter Proteine, unter anderem des Transkriptionsfaktors DDIT3, induziert wird. Dabei ist die DDIT3 Expression in der Frühphase spezifisch für Oligodendrozyten. Auf funktioneller Ebene konnte nachgewiesen werden, dass *Ddit3*-defiziente Tiere teilwiese gegen eine durch Cuprizone induzierte Demyelinisierung geschützt sind.

Für die Beantwortung der zweiten Fragestellung wurde das autoimmun vermittelte MS Tiermodell EAE verwendet. Die Analyse des Gangmusters erfolgte mittels (engl.) „*High Speed Ventral Plane Videography*“. Es konnte gezeigt werden, dass während der Entwicklung neuer, inflammatorischer Herde im ZNS der Versuchstiere verschiedene Gangdefizite auftreten, wie beispielsweise eine verlängerte Schwungphase bei verkürzter Standphase. Interessanterweise waren diese Veränderungen des Gangmusters noch vor dem Auftreten anderer motorischer Defizite, wie etwa einer Lähmung des Schwanzes, feststellbar.

Zusammenfassend beschäftigen sich beide Arbeiten mit der Frühphase zweier gängiger MS Tiermodelle. In der frühen Phase des EAE Modells kommt es zur Entstehung entzündlicher ZNS Läsionen. Gangdefizite stellen zu diesem Zeitpunkt einen sensitiven klinischen Parameter dar. In der frühen Phase des Cuprizone Modells kommt es zu zellulärem Stress. Da DDIT3 dabei die Oligodendrozyten Apoptose reguliert, ist die zugehörige Signalkaskade ein möglicher Therapieansatz. Sollte es möglich sein, die Entstehung von ER-Stress in Oligodendrozyten zu verhindern, könnte dies eine Demyelinisierung verhindern bzw. abschwächen.

Summary

During my doctoral studies I dealt with two aspects of MS: First, the role of ER stress response in oligodendrocyte degeneration and demyelination. Secondly, whether gait deficits can be detected in the early phase of inflammatory demyelination.

The toxic demyelination model Cuprizone was used to answer the first question. It was shown that the expression of various ER stress associated proteins, including the transcription factor DDIT3, are induced early in the animal model. DDIT3 expression in the early phase is specific for oligodendrocytes. On a functional level it could be shown that *Ddit3*-deficient animals are partially protected against Cuprizone induced demyelination.

The autoimmune MS animal model EAE was used to answer the second question. The analysis of the gait pattern was performed by 'High Speed Ventral Plane Videography'. It could be shown that during the development of new inflammatory lesions in the CNS of the experimental animals various gait deficits occur, such as a prolonged swing phase with a shortened stance phase. Interestingly, these changes in gait pattern were observed before other motor deficits, such as tail paralysis, occurred.

In summary, both studies deal with the early phase of two common MS animal models. In the early phase of the EAE model, inflammatory CNS lesions develop. Gait deficits are a sensitive clinical parameter at this stage. Cellular stress occurs in the early phase of the Cuprizone model. Since DDIT3 regulates the oligodendrocytes apoptosis, the associated signaling cascade is a possible therapeutic approach. If it is possible to prevent the development of ER stress in oligodendrocytes, this could prevent or at least weaken demyelination.

Literaturverzeichnis

Acs, P. (2013, September). Distribution of oligodendrocyte loss and mitochondrial toxicity in the cuprizone-induced experimental demyelination model. *Journal of neuroimmunology*, pp. 128-131.

Alvarez, J. (2015, February). Focal disturbances in the blood-brain barrier are associated with formation of neuroinflammatory lesions. *Neurobiology of disease*, pp. 14-24.

Baranzini, S. (2005, June). Modular transcriptional activity characterizes the initiation and progression of autoimmune encephalomyelitis. *Journal of immunology*, pp. 1412-1422.

Bender, A. (2015). *Kurzlehrbuch Neurologie.* München: Elsevier GmbH.

Bergles, D. (2015, August). Oligodendrocyte Development and Plasticity. *Cold Spring Harbor perspectives in biology*, pp. 1-27.

Edagawa, M. (2014, August). Role of activating transcription factor 3 (ATF3) in endoplasmic reticulum (ER) stress-induced sensitization of p53-deficient human colon cancer cells to tumor necrosis factor (TNF)-related apoptosis-inducing ligand (TRAIL)-mediated apoptosis through up-re. *The Journal of biological chemistry*, pp. 21544-21561.

Edgar, J. (2004, Juli). Oligodendroglial modulation of fast axonal transport in a mouse model of hereditary spastic paraplegia. *The Journal of Cell Biology*, pp. 121-131.

Evangelidou, M. (2014, May). Altered expression of oligodendrocyte and neuronal marker genes predicts the clinical onset of autoimmune encephalomyelitis and indicates the effectiveness of multiple sclerosis-directed therapeutics. *Journal of immunology*, pp. 4122-4133.

Feys, P. (2017, April). The Nine-Hole Peg Test as a manual dexterity performance measure for multiple sclerosis. *Multiple Sclerosis*, pp. 711-720.

Fünfschilling, U. (2012, April). Glycolytic oligodendrocytes maintain myelin and long-term axonal integrity. *Nature*, pp. 517-521.

Gold, R. (2012). *Diagnose und Therapie der Multiplen Sklerose: S2-Leitllinie.* Deutsche Gesellschaft für Neurologie.

Hafler, D. (2004, März). Multiple Sclerosis. *The Journal of Clinical Investigation*, pp. 788-794.

Kipp, M. (2009, Dezember). The cuprizone animal model: new insights into an old story. *Acta neuropathologica*, pp. 723-736.

Kipp, M. (2017, März). Multiple sclerosis animal models: a clinical and histopathological perspective. *Brain pathology*, pp. 123-137.

Kozutsumi, Y. (1988, März). The presence of malfolded proteins in the endoplasmic reticulum signals the induction of glucose-regulated proteins. *Nature*, pp. 462-464.

Kuhlmann , T. (2016, Dezember). An updated histological classificaion system for multiple sclerosis lesions. *Acta Neuropathology*, pp. 13-24.

Kurtzke. (1983, November). Rating neurologic impairment in multiple sclerosis: an expanded disability status scale (EDSS). *Neurology*, pp. 1444-1452.

Lin, Y. (2012, Mai). Interferon-γ activates nuclear factor-κ B in oligodendrocytes through a process mediated by the unfolded protein response. *PLoS One*, pp. 1-13.

Lodish, H. (2000). *Molecular Cell Biology. 4th edition.* New York: W. H. Freeman.

Mason, J. (2000, August). Mature oligodendrocyte apoptosis precedes IGF-1 production and oligodendrocyte progenitor accumulation and differentiation during demyelination/remyelination. *Journal of Neuroscience Research*, pp. 251-262.

Mitew, S. (2013, November). Mechanisms regulating the development of oligodendrocytes and central nervous system myelin. *Neuroscience*, pp. 29-47.

Motl, R. (2017, April). Validity of the timed 25-foot walk as an ambulatory performance outcome measure for multiple sclerosis. *Multiple sclerosis*, pp. 704-710.

Nylander, A. (2012, April). Multiple Sclerosis. *The Journal of Clinical Investigation*, pp. 1180-1188.

Philips, T. (2017, September). Oligodendroglia: metabolic support of neurons. *The Journal of clinical investigation*, pp. 3271-3280.

Pihl-Jensen, G. (2017, Juli). Multifocal visual evoked potentials in optic neuritis and multiple sclerosis: A review. *Clinical Neurophysiology*, pp. 1234-1245.

PRISMS Study Group. (2001, June). PRISMS-4: Long-term efficacy of interferon-beta-1a in relapsing MS. *Neurology*, pp. 1628-1636.

Rejdak K. (2010, Juli). Multiple sclerosis: a practical overview for clinicians. *British medical bulletin*, pp. 79-104.

Rutkowski, D. (2006, November). Adaptation to ER stress is mediated by differential stabilities of pro-survival and pro-apoptotic mRNAs and proteins. *PLoS Biology*, pp. 2024-2041.

Sano, R. (2013, Dezember). ER stress-induced cell death mechanisms. *Biochemica et biophysica acta*, pp. 3460-3470.

Stys, P. (2012, Juni). Will the real multiple sclerosis please stand up? *Nature reviews. Neuroscience.*, pp. 507-514.

Teske, N. (2018, Februar). Chemical hypoxia-induced integrated stress response activation in oligodendrocytes is mediated by the transcription factor nuclear factor (erythroid-derived 2)-like 2 (NRF2). *Journal of neurochemistry*, pp. 285-301.

Thompson, A. (2018, Februar). Diagnosis of multiple sclerosis: 2017 revisions of the McDonald criteria. *The Lancet. Neurology*, pp. 162-173.

Xu, C. (2005, Oktober). Endoplasmic reticulum stress: cell life and death decisions. *The journal of clinical investigation*, pp. 2656-2664.

Danksagung

Herrn Prof. Dr. Dr. Markus Kipp danke ich für die Überlassung des Themas sowie die ausgezeichnete Betreuung und Unterstützung bei der Durchführung der Arbeit.

Auch möchte ich allen Mitarbeitern der Anatomischen Anstalt der Ludwig-Maximilians-Universität zu München danken, die dazu beigetragen haben, dass ich dieses Thema mit Freude bearbeiten konnte. Besonders danke ich Sarah Wübbel, Astrid Baltruschat, Beate Aschauer und Sabine Tost für Ihre herausragende technische Assistenz.

Meinen Eltern und meinen Freunden danke ich für die bedingungslose Unterstützung während des Studiums und darüber hinaus.